2D Atomic Layer Crystals for Nanoelectronics and Applications

by

Zhe Liu

A dissertation submitted in partial fulfillment
of the requirements for the degree of
Doctor of Philosophy
(Electrical and Computer Engineering)
in the University of Michigan
2021

Doctoral Committee:

Professor Zhaohui Zhong, Chair
Professor Xudong Fan
Professor L. Jay Guo
Professor Wei Lu

Zhe Liu

zheliu@umich.edu

ORCID iD: 0000-0002-2308-3342

Dedication

To my loved Ke Gao and my family.

Acknowledgements

I would like to first thank my advisor, Professor Zhaohui Zhong who kindly lead me into the wonderful research field of two-dimensional material nanoelectronics. Throughout my entire PhD life, his creative and professional advice, enthusiasm in research and considerate encouragement have always been my inspiration towards self-actualization. Always available for discussions and prepared to share with me his innovative ideas and essential advice on the problems I come up with, he is the example of virtue and professionalism that lead me to where I am today. I express my sincere gratitude and respect to him.

I would also like to present my gratitude to my committee members Professor Xudong (Sherman) Fan, Professor L. Jay Guo and Professor Wei Lu for their encouragement and careful review of my research. Thanks to Professor Fan for his insightful advice and his selfless help and support during our collaboration on graphene sensor related projects. Thanks to Professor Guo and Professor Lu for their valuable suggestions on the improvement of the graphene bipolar junction transistor project.

I am also grateful to many other professors at the University of Michigan besides my committee members, especially Professor Zetian Mi, Professor Pallab Bhattacharya, Professor Stephen Forrest and Professor Mackillo Kira from Electrical and Computer Engineering, Professor Aaron Pierce and Professor Kai Sun from Physics department and Dr. Brenda Imber from the English Language Institute for their excellent lectures, careful instruction and valuable suggestions in my PhD life.

I cherish my experience working in the Zhong group, an enjoyable period of friendship and endeavor. Many thanks to our former and current group members Dr. Wenzhe Zang, Dr. Girish S. Kulkarni, Dr. Chehung Liu, Dr. Minmin Zhou, Dehui Zhang, Audrey Rose Gutierrez and You (Wade) Wu for their generous support, kind encouragement and enlightening discussions about various aspects such as device fabrication details, lab equipment operations and the graphene growth and transfer method.

I would also like to thank my collaborators Maxwell Li from the Professor Fan group and Zhen Xu from the Professor Norris group for their collaborations on the graphene sensor project and the MoS_2 growth and applications, respectively. Without their selfless and professional support, the research can hardly be conducted with such efficiency and productivity. I thank all the staff from the Lurie Nanofabrication Facility for their support in tool training, fabrication processes and the FirstNano furnace maintenance.

I am thankful to all my friends who have brought happiness and pleasure into my life. In addition to those mentioned above, I further thank Kaiwen Guo, Dr. Chengang Ji, Dr. Da Li, Ruikun Luo, Jingyang Sui, Qiwen Wang, Dr. Ping Wang, Dr. Xifeng Wang, Dr. Yongjie Wang, Dr. Yuanpeng Wu, Dongxiao Yan, Zhong Zhang and many others for the good time we shared in Ann Arbor.

Finally, I present my sincere gratitude to my girlfriend Ke Gao and my family, who give their unconditional love and support to me and encouraged me to reach this milestone in my life.

Table of Contents

List of Tables

List of Figures

Abstract

Since the discovery of graphene in 2004, much research enthusiasm has been evoked for this first discovered two-dimensional (2D) material due to its unique physical and electrical properties, such as an extraordinarily high surface-to-volume ratio, a gapless linear band structure with Fermi level tunability, bipolarity and ultra-high carrier mobility. The following discovery of transitional metal dichalcogenides (TMDCs), with direct band gaps and spin-coupled valleys, adds another crucial piece to the 2D material library.

The thesis aims at 2D materials growth and utilizing their unique physical and electrical properties for real-world solid-state device applications. Chemical vapor deposition (CVD) of monolayer MoS_2 is first demonstrated, with both single crystalline flake (~15 μm) and large area (centimeter level) polycrystalline continuous film growth achieved. Various characterization methods are subsequently utilized to examine growth morphology and quality such as optical microscopy, scanning electron microscopy (SEM), Raman spectroscopy, photoluminescence (PL), atomic force microscopy (AFM) and electrical measurements. Monolayer growth is confirmed by AFM and PL for monocrystalline flakes and polycrystalline continuous films, respectively.

For the application portion, an electrically tunable lateral structured graphene-silicon-graphene bipolar junction transistor (BJT) has been fabricated with direct current gain over 20. During device operation, electrons in the graphene emitter overcome the graphene/Si barrier to diffuse into the silicon base and are subsequently collected by the collector under a large base-

collector reverse bias. In contrast with traditional silicon BJTs, the current gain of graphene BJT device can be readily and smoothly tuned. With the doping concentration and Fermi level of the graphene emitter electrically controlled by a top gate electrode, the electron injection barrier height is consequently tuned, leading to tunability in the graphene BJT direct current gain. With decent performance, simplicity and extensibility, this novel graphene BJT device demonstrates a promising way forward for nanoscale BJT applications.

With an ultra-high surface to volume ratio, graphene is an ideal platform for sensor applications. A graphene chemical sensor, based on a pristine graphene field-effect-transistor (FET) bonded with a μ-column gas flow channel cap, has been miniaturized for volatile compounds sensing and discrimination. With a small size of 1 cm by 0.7 cm, the miniature graphene sensor remains as sensitive (nanogram detection limit) and even faster (down to sub-second) than its pioneering large footprint counterpart. More importantly, a true label-free nanoelectronic sensing platform is pioneered by combining the electrical gate tunability of graphene sensor responsivity (or gate spectra) with the principal component analysis (PCA) technique. In contrast to conventional electronic sensors or electronic nose technology, surface functionalization is no longer needed in order to achieve chemical discrimination. 11 measured chemicals (acetone, ethyl acetate, chloroform, dichloromethane, pentane, heptane, nonane, benzene, toluene, o-xylene and p-xylene), as represented by 11 clusters of points in PCA plot, are clearly grouped into separate regions with each representing a corresponding chemical category. The identification accuracy, as verified by multiple algorithms such as k-nearest neighbors (KNN), linear discrimination analysis (LDA), support vector machine (SVM) and multi-layer perceptron (MLP), is rather satisfactory with at least 98.8% accuracy for the 11 specific chemicals and at least 93.9% accuracy for the four corresponding categories, indicating

the robustness of data acquired by the graphene sensor. This work should lay the groundwork toward true label-free electronic sensor with high sensitivity and selectivity, and a novel electronic nose technology with better simplicity and higher accuracy.

Chapter 1 Introduction to Graphene

1.1 Carbon Allotropes – A Brief History

In 1985, a new carbon isotope consisting of 60 carbon atoms, which is now called fullerene, was discovered by Kroto et al. with laser-induced vaporization of graphite[1,2]. This discovery has evoked enthusiasm for the zero-dimensional carbon crystal and subsequently initiated the revolution of carbon-based nanomaterial studies. Six year later, the synthesis of carbon nanotubes (CNT) by Iijima extended the carbon material study from zero dimensions to one dimension, leading to numerous research studies covering each aspect of CNT properties such as growth mechanisms and methods, as well as optical and electrical properties[3-6]. The electrical properties of CNT are intriguing due to its high carrier mobility, ballistic transport and the unique Dirac cone band structure with certain CNT lattice structures[6].

The discovery and characterization of graphene – the two-dimensional carbon crystal – by Andre Geim and Konstantin Novoselov through mechanical exfoliation from bulk graphite in 2004[7], has finally brought this crucial two-dimensional member to the carbon allotropes family. Compared with the growth of CNT, which lacks control over CNT lattice structure and suffers from difficulty in alignment, the two-dimensional nature of graphene allows a relatively simple and controllable way of growth on a substrate surface, laying a good foundation for large-scale device applications. Numerous electronic and optoelectronic devices have been designed and fabricated with this atomically thin two-dimensional crystal such as graphene FETs, graphene transparent photodetectors, graphene-silicon barristors and graphene chemical sensors. The unique semimetal nature of graphene grants these devices another dimension of

controllability through Fermi level tunability. After the reports of successive two-dimensional crystals such as MoS_2, atomically thin heterojunctions can also be readily achieved, leading to novel and fascinating nanoelectronics and applications.

1.2 Graphene Lattice Structure

Graphene is a two-dimensional crystal consisting of carbon atoms with a honeycomb structure. Individual layers of graphene make up graphite bulk crystals, bonded by Van der Waals force with an interlayer spacing around 3.35 Å[8,9]. The sp^2 hybridization of carbon atoms forms in-plane orbitals with three-fold rotational symmetry, which contributes to carbon-carbon σ bonds with a length of 1.42 Å[10]. On the other hand, the half-occupied unaffected $2p_z$ orbital, which is perpendicular to the graphene plane, binds with other $2p_z$ orbitals from neighboring carbon atoms, forming a delocalized π bond as in the case of benzene[10]. This interaction between neighboring out-of-plane $2p_z$ orbitals results in graphene's unique linear gapless band structure, which will be discussed in detail in the following section.

The graphene honeycomb structure can be treated as a hexagonal lattice with two bases (A and B sites) per unit cell, as shown in Figure 1.1. The two translational vectors can be chosen as $\boldsymbol{a_1} = \frac{1}{2}a\left(\boldsymbol{3i} + \sqrt{3}\boldsymbol{j}\right)$ and $\boldsymbol{a_2} = \frac{1}{2}a\left(\boldsymbol{3i} - \sqrt{3}\boldsymbol{j}\right)$ respectively with a representing the carbon-carbon σ bond length and $\boldsymbol{i}$, $\boldsymbol{j}$ symbolizing the horizontal and vertical unit vectors.

The corresponding reciprocal translational vectors are $\boldsymbol{b_1} = \frac{2\pi}{3a}\left(\boldsymbol{i} + \sqrt{3}\boldsymbol{j}\right)$ and $\boldsymbol{b_2} = \frac{2\pi}{3a}\left(\boldsymbol{i} - \sqrt{3}\boldsymbol{j}\right)$. The first Brillouin zone has the same honeycomb structure but with a rotation of 30 degrees compared to its real space counterpart. High symmetry points such as the Γ point in

the center, K and K' points at hexagonal corners and the M point at the midpoint of edges, are also present in the first Brillouin zone.

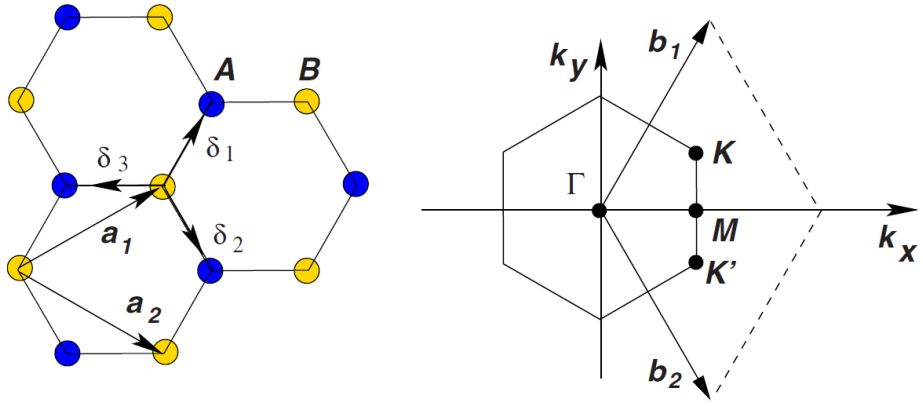

Figure 1.1 The lattice structure (left) and corresponding reciprocal lattice of graphene (right), with high symmetry points marked. [10]

1.3 Graphene Band Structure

Using the tight-binding model with linear superposition of the out-of-plane $2p_z$ orbital wavefunctions, dispersion relation of graphene can be derived as

$$E_{\pm}(k_x, k_y) = \pm t\left\{1 + 4\cos\left(\frac{3k_x a}{2}\right)\cos\left(\frac{\sqrt{3}k_y a}{2}\right) + 4\cos^2\left(\frac{\sqrt{3}k_y a}{2}\right)\right\}^{\frac{1}{2}}$$

where only nearest neighbor hopping energy $t \approx 2.8$ eV has been considered[6,10,11]. The plus and minus sign in $E_{\pm}$ correspond to the vacant antibonding π^* and fully occupied bonding π bands respectively, with the energy zero point set to the $2p_z$ atomic orbital energy.

Specially, at the first Brillouin zone corners $K = \frac{2\pi}{3a}\left(\boldsymbol{i} + \frac{1}{\sqrt{3}}\boldsymbol{j}\right)$ and $K' = \frac{2\pi}{3a}\left(\boldsymbol{i} + \frac{1}{\sqrt{3}}\boldsymbol{j}\right)$, the gap between the antibonding and bonding bands vanishes, resulting in a unique gapless linear dispersion relation or Dirac cone. A small deviation $\boldsymbol{q}$ from K (K') points leads to an approximated energy change as $E_{\pm}(\boldsymbol{q}) = \pm v_F|\boldsymbol{q}| + O\left(\frac{\boldsymbol{q}^2}{\boldsymbol{K}^2}\right)$, where group velocity, or Fermi velocity $v_F = \frac{3ta}{2}$ with a value around 1×10^6 m/s[10,11].

Unlike its two-dimensional counterparts such as a two-dimensional electron gas (2DEG) prepared in quantum wells, which has a parabolic dispersion relation and a constant density of states (DOS), graphene has an ultra-low DOS near the Dirac point with an increasing trend corresponding to linear energy deviation from the Dirac point. This causes a low quantum capacitance near the Dirac point, resulting in efficient tunability in graphene's Fermi level. In device applications, using gate electrodes is the most commonly used way to tune the graphene Fermi level through the carrier density change from the electrical gating effect, with representative devices like graphene FETs and graphene barristors.

Quantitatively, the relation between the Fermi level position and gate voltage can be calculated from the graphene band structure[10]. Using the linear dispersion relation $E(k) = \hbar v_F k$ near the Dirac point, the Fermi level position with reference to the Dirac point is proportional to the square root of the total graphene carrier density n with $\Delta E_F = \pm \hbar v_F \sqrt{\pi n}$, where the positive sign stands for electrons and the negative sign for holes. Since the induced electron/hole density change is simply governed by the linear capacitance model with gate voltage as $\Delta n = C_g V_g$, this electrical tunability is the most effective near the Dirac point, where graphene is intrinsic without gate voltage.

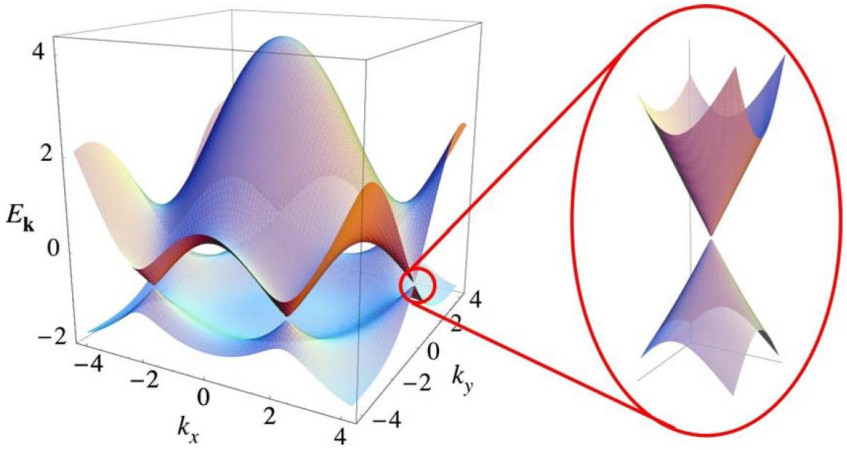

Figure 1.2 Graphene band structure with gapless linear dispersion relation (Dirac cone). Features near K and K' points are zoomed in for a clearer view. [10]

The unique gapless linear band structure determines that electrons and holes can both dominate as majority carriers in graphene, which leads to its characteristic V-shaped transfer curve, with the negative gate voltage side corresponding to the hole conduction region and the positive side to the electron conduction region. This gapless band structure, however, unlike the bandgap of traditional silicon transistors, does not allow a decent off state for graphene FETs due to this bipolarity. As a result, the on-off ratio of graphene FETs is too low for logic switch applications and unfortunately can hardly be improved without band structure engineering.

Graphene is also known for its high mobility as in the case of carbon nanotubes. Mobilities for electrons and holes in lightly doped silicon are around 1400 $cm^2/(V \cdot s)$ and 480 $cm^2/(V \cdot s)$, respectively[12], while the carrier mobility can reach as high as 200000 $cm^2/(V \cdot s)$ for suspended graphene[13,14]. For graphene FET devices, due to the scattering caused by surface charge centers[15-18], interfacial phonons[19], substrate ripples[20-22] and contamination from growth[23] and fabrication[24,25], graphene mobility is reduced while remaining decent, and can still reach as high as 20000 $cm^2/(V \cdot s)$[13].

1.4 Graphene Synthesis

Graphene synthesis can be achieved through either top-down methods from graphite bulk crystal or bottom-up methods through carbon deposition processes governed by chemistry. In a straightforward way, graphene can be mechanically exfoliated from bulk graphite by adhesive tape, which is exactly the method that lead to the discovery of graphene in 2004 by Andre Geim and Konstantin Novoselov[7]. Mechanically exfoliated single crystalline graphene has the highest quality– as indicated by its ultra-high carrier mobility - and is ideal for studies that require high sample purity and low defect density. However, the non-scalability and the relatively low yield of tape exfoliation severely limit its practical use for electronic device

applications. Other exfoliation methods such as manual or automatic transfer-printing mechanical exfoliation[26,27] and electric field assisted mechanical exfoliation[28,29] have been proposed to achieve more controllable mechanical exfoliation, but the size of graphene, the yield of the process and quality control still remain an issue.

Though potentially scalable with low cost, the chemical exfoliation method still yields only small flakes around 1 μm which are only stable in organic solutions or a surfactant/water solution[30]. Epitaxial growth of graphene on SiC, a bottom-up method for large scale synthesis, has also been proposed and demonstrated[31,32]. Unfortunately, the high cost of SiC substrates and the lack of control over the number of layers of growth, together with challenges in the transfer process, cancel out the potential benefits of this growth method.

In the meantime, CVD growth of graphene has been quickly developed on various substrates such as nickel (Ni), copper (Cu), platinum (Pt), ruthenium (Ru), iridium (Ir), iron (Fe) and metal carbides substrates[33-37]. Especially, CVD growth on copper possesses the merits of large growth area, decent growth quality and simple wet transfer process and consequently has been commonly utilized to produce graphene for device applications. It is necessary to mention that, despite the resemblance in growth procedures, graphene growth mechanisms are different for copper based and nickel based growth. In the case where nickel is used as the substrate, carbon atoms originating from methane pyrolysis first get dissolved in nickel, before segregation and precipitation during the cooling process lead to the formation of graphene[37,38]. Graphene growth on copper, on the other hand, is governed by surface adsorption as demonstrated by using ^{12}C and ^{13}C carbon isotope-labelled methane precursor alternatively as carbon sources, and the observation that there is no mix-up of the two carbon isotopes in graphene regional growth[37]. The local carbon isotope type can be readily identified using Raman spectrum – both G and 2D

peaks from graphene consisting of ^{13}C atoms will result in smaller Raman shifts compared with normal ^{12}C graphene due to the difference in atomic mass[37].

1.5 Graphene Optical Properties

For mono- and few-layer graphene, each layer has a significant absorption of 2.3% for incident white light as shown in Figure 1.3[39,40], which makes graphene ideal for optoelectronic devices such as transparent photodetectors for three-dimensional image sensing and reconstruction[41].

This property can also be practically utilized for quick inspections of wrinkles and holes under an optical microscope, especially for large area graphene quality control after a PMMA-assisted transfer process. 285 nm-thick silicon dioxide is a common choice for the gating dielectric of graphene FETs, at which thickness both requirements for good insulation quality and high optical contrast between graphene and SiO_2/Si substrate are well satisfied[42].

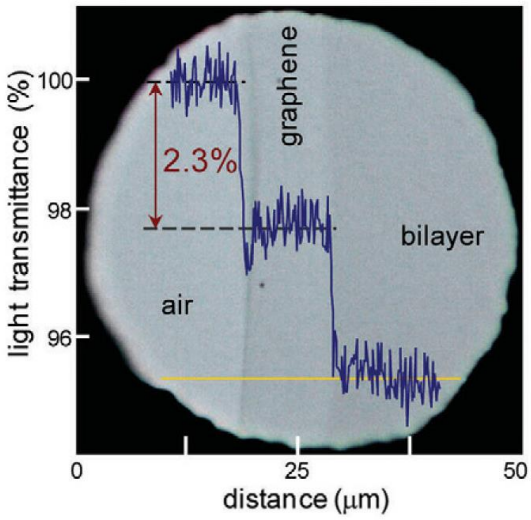

Figure 1.3 White light absorption of mono- and bilayer suspended graphene in comparison with the air. [39,40]

1.6 Graphene Raman Spectrum

The Raman spectrum originates from the interactions between crystal lattice vibration modes and incident monochromatic photons. Raman shifts, typically in the form of a wavenumber change before and after scattering, are unique for each vibration mode in the examined material at the same incident photon wavelength and hence are commonly used as the fingerprint in material discrimination.

Raman spectroscopy, naturally, can also be used to examine the quality of graphene, which includes the differentiation of mono- and few-layers, extraction of defect density and even information about the crystal doping, strain and stress[43]. The two significant Raman peaks of graphene and graphite are the G peak at ~1580 cm^{-1} and the 2D peak (formerly called G' peak) at ~2700 cm^{-1}, with a defect related D peak at ~1350 cm^{-1}[43-47]. The G peak originates from in-plane degenerated transverse optical and longitudinal optical phonon modes with E_{2g} symmetry at the Γ point[43,45]. The D peak and its overtone 2D peak share the same origin from the breathing mode of six-atom rings, with the difference that the D peak requires activation by defects and does not appear in perfect crystals while the 2D peak needs no activation and always exists[43].

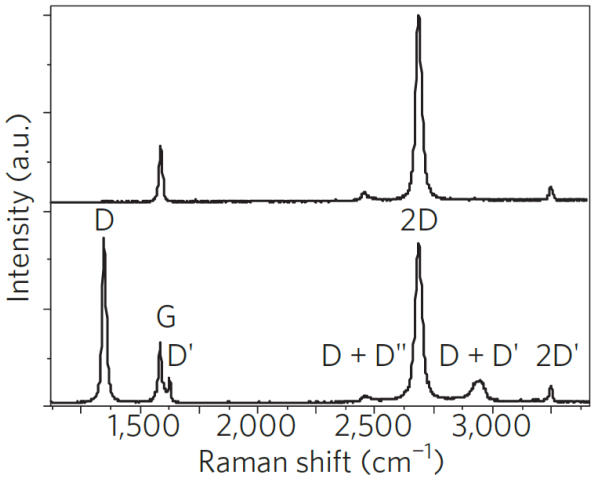

Figure 1.4 Raman spectrum of pristine (top) and defected (bottom) graphene. D peak in graphene requires activation by defects while G and 2D peaks always exist in graphene. [43]

The ratio of the G peak height over the 2D peak height increases significantly with the thickness of a graphene crystal – from a value of 0.24 for a monolayer to 2.1 for a five-layer graphene crystal, which is a crucial criterion to distinguish monolayer graphene from its few-layer counterparts or graphite bulk crystal[48]. In more detail, monolayer graphene has only one single 2D peak, while this characteristic peak consists of four individual peaks for bilayer graphene due to graphene antibonding π^* and bonding π band splitting induced by interlayer interaction[44].

1.7 Graphene-semiconductor Junctions

A Schottky barrier forms at the graphene/silicon interface just as in the usual metal-silicon junction case, with the barrier height for electron injection also defined by the difference between the electron affinity of silicon and graphene's Fermi level in an ideal case. In contrast to metal Schottky diodes, the barrier height of graphene-semiconductor junctions is electrically tunable by changing graphene's Fermi level with a gate electrode, as demonstrated by the three terminal gate-controllable graphene-silicon device or the graphene barristor reported in 2012[49,50].

The current on/off ratio of a graphene barristor device has reached 10^5[50], which is significantly higher than graphene FETs with a value around 30 at a temperature of 300 K[7]. Though this on/off ratio is still several orders of magnitude lower than that of a silicon metal-oxide-semiconductor FET (MOSFET), which targets a value more than 10^7 for low standby power (LSP) logic in the 2007 International Technology Roadmap for Semiconductors (ITRS)[51], it demonstrates the possibility of applying gapless graphene to real logic device applications such as the invertor and half adder built from several graphene barristors as shown in Ref[50].

The Fermi level of pristine graphene, which has been reported to be 4.57eV[52], lies around the midgap of silicon with conduction band edge at 4.05eV and a band gap of 1.12eV[49]. The corresponding graphene-silicon Schottky barrier height for electrons is therefore around 0.55 eV without considering any non-ideal effects. Under positive gate voltage, electrons are induced through the electrical gating effect, thus leading to a higher graphene Fermi level and consequently a smaller electron injection barrier. In the same way, holes are induced under negative gate voltage, leading to a lowered graphene Fermi level and a higher barrier for electrons to overcome. The corresponding band diagrams describing graphene/n-Si heterojunction gate tunability are shown in Figure 1.5.

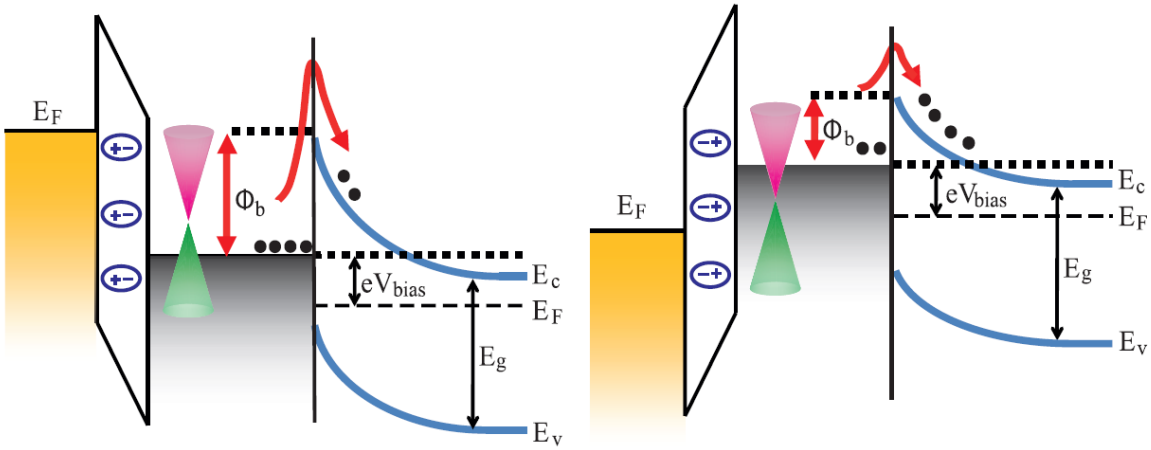

Figure 1.5 Band diagram of graphene-n-doped silicon heterojunction. [50]

The barrier height ϕ_b can be readily extracted from the temperature dependence of graphene/Si junction reverse saturation current (I_{sat}) with $I_{sat} \approx AKT^2 \exp\left(\frac{-q\phi_b}{kT}\right)$, where A is the area of the Schottky junction, K ≈ 100 A/(cm^2/K^2) is the Richardson constant and q, k stand for electron charge and Boltzmann constant respectively[12,50]. As the gate voltage increases from -1 V to 5 V, the corresponding extracted barrier height ϕ_b drops from 0.44 eV to 0.26 eV, which agrees well with the change in graphene Fermi level from 0.09 eV above the Dirac point to 0.23 eV due to the electrical gating effect[50].

Another way to measure the Schottky barrier height is by first extracting the built-in potential ϕ_{bi} under relatively high frequency from the relationship between depletion region capacitance (C) and reverse applied bias V_r as $1/C^2 \propto (\phi_{bi} + V_r)$, followed by the addition of the energy difference between the unbiased semiconductor conduction band edge and Fermi level[12,49]. This method, however, tends to give slightly larger values, which are reported in Ref[49], compared to that using saturation currents at different temperatures reported in Ref[50]. The overestimation of the Shottky barrier is ascribed to graphene Fermi level lowering – possibly from hole doping due to the iron (III) nitrate etchant in the graphene wet transfer process[49,53] together with the effect of gold electrodes[49,52].

Besides silicon, other semiconductors such as GaAs, 4H-SiC and GaN, with electron affinity around 4.1 eV, 3.4 eV and 4.1 eV respectively, can also form the same structure with graphene as studied in Ref[49]. Schottky barrier heights ϕ_b of the four graphene-semiconductor junctions can also be extracted as 0.86 eV (Gr/n-Si), 0.79 eV (Gr/n-GaAs), 0.91 eV (Gr/n-4H-SiC) and 0.73 eV (Gr/n-GaN), with corresponding graphene Fermi levels deduced as 4.91 eV, 4.89 eV, 4.31 eV and 4.83 eV, respectively, from the saturation current temperature dependence[49].

It is, however, necessary to point out that the Schottky barrier heights of graphene-semiconductor junctions may also be severely susceptible to non-ideal factors. Interfacial states mainly contributed by few atomic layers near the surface, can exist with a significant density of states in the band gap. These states can be either donor-like or acceptor-like and result in a potential change within the few atomic layer-thick interface. The existence of this potential change across the interface leads to deviation of the Schottky barrier height from the ideal value, leading to Fermi level pinning. Moreover, the image-force lowering as well as quantum tunneling may also result in reduction of the effective barrier height especially under a high interface electrical field, with the barrier lowering in the former proportional to the square root of the electrical field. [12,54]

1.8 Overview of the Dissertation

This dissertation focuses on the growth of two-dimensional materials and utilizing their unique properties such as ultra-high surface-to-volume ratio and graphene's Fermi level tunability for novel device applications. Chapter 1 and chapter 2 provide the introduction to graphene and MoS_2 respectively, with key aspects such as lattice structure, band structure, unique electrical properties, synthesis and/or characterization methods reviewed for a comprehensive understanding. Monolayer MoS_2 chemical vapor deposition (CVD) growth is presented in Chapter 3 for both single crystalline flakes and large area polycrystalline continuous film growth, followed by various characterization methods to examine growth quality.

Chapter 4 demonstrates a lateral graphene-silicon-graphene BJT with an electrically tunable direct current gain by utilizing the Fermi level tunability of the graphene emitter. A μ-column graphene chemical sensor for fast sensing and vapor separation is first reviewed in Chapter 5, followed by the miniaturization of the device with performance evaluation and

comparison. Chapter 6 presents the accurate discrimination for volatile compounds with a single label-free μ-column graphene chemical sensor, with response trends with gate voltage (or gate spectra) as the fingerprint. Chapter 7 summarizes this dissertation and proposes ideas of vertical structured graphene BJT and potential integration with Tedlar bags for higher sensing and discrimination performance.

Chapter 2 Introduction to MoS_2

2.1 Transitional Metal Dichalcogenides – A New Family of 2D Crystals

Since the discovery of graphene in 2004[7], great enthusiasm has been evoked for exploration of two-dimensional materials. Graphene, despite being a great study object with intriguing physical and electrical properties such as Fermi level tunability and extra-high mobility[10,13,14], still has its intrinsic limitations for certain device applications. The gapless band structure of graphene enables bipolar conduction and gate tunability, but restricts the development of graphene FETs due to its low on/off ratio which reaches only approximately 30 and therefore is less desirable for switching device applications[7]. Various methods have been proposed for graphene gap opening through the silicon carbide substrate effect[55], patterned hydrogen adsorption on graphene following Moiré superlattice periodicity[56] or quantum confinement and edge engineering in graphene nanoribbons[57-60], but reliable and practical engineering control over graphene for desired band gap opening remains challenging. This challenge also exists for AB stacking bilayer graphene band gap opening by the electrical field effect, with the gap opening (less than 200 meV) still being too small for switch device applications[61,62].

In light of the intrinsic limitations originating from graphene's gapless nature, other two-dimensional crystals discovered later than graphene such as black phosphorus and TMDCs have gradually become more and more attractive for nanoelectronics and device applications. Bulk black phosphorus, a layered crystal with individual atomic layers bounded by van der Waals force with ~5Å interlayer spacing, was discovered more than one century ago in 1914, while its

two-dimensional atomic crystal counterpart, phosphorene, has just been reported a few years ago after the rise of graphene[63,64]. The band gap of black phosphorus crystal varies greatly with thickness, resulting in a band gap range from 0.3 eV for bulk or few-layer thin film (thickness > 4 nm or eight layers) to an estimated 2 eV for monolayer black phosphorus crystal[63,65-67]. The carrier mobility extracted from 10 nm-thick black phosphorus FET can reach as high as ~1000 $cm^2/(V \cdot s)$ as reported in Ref[64], which is comparable to that of modern silicon devices. Black phosphorus thin films, however, are unstable in the presence of water vapor and oxygen and can degrade quickly without proper encapsulation due to chemical reactions into aqueous phosphoric acid and phosphorus oxide respectively[63,67,68].

TMDCs MX_2 form another representative library of emerging two-dimensional crystals. Bulk TMDC materials are also stacked layer crystals bonded by van der Waals force, which consist of one transitional metal atom (M = Mo, W etc.) and two chalcogen atoms (X = S, Se etc.) in stoichiometry. Like black phosphorus, TMDC semiconducting crystals also have thickness-dependent bandgaps due to interlayer interactions – as in the 2H-MoS_2 crystal case where the band gap increases together with an indirect to direct band gap transition when the material is thinned down from bulk to monolayer thickness[69-73]. The mobility of exfoliated MoS_2 on SiO_2/Si substrates is extracted to be 0.5 ~ 3 $cm^2/(V \cdot s)$ from MoS_2 FET devices in early studies[74], but the mobility can be further improved to at least 200 $cm^2/(V \cdot s)$ with hafnium oxide acting as a high-k gate dielectric at room temperature as reported by Ref[74]. While the mobility of MoS_2 is not so perfect when compared to ultra-high mobility graphene, or even black phosphorus and silicon, it becomes adequate for practical and novel device explorations. MoS_2 FETs have already been fabricated one decade ago with a demonstration of room temperature on/off ratio achieved as high as 10^8 and low stand-by power consumption owing to its moderate

band gap[75]. Recently transistors based on WS_2, another favored TMDC material, have been integrated into a 300 mm pilot line with an industry back end of line (BEOL) compatibility as reported by researchers from IMEC[76], bringing TMDC thin films one step closer to integration with CMOS-compatible mass production lines.

Besides the promising application for pure electrical devices such as field-effect transistors, TMDCs are also great platforms for valleytronic studies. Due to the broken spin degeneracy induced by spin-orbital interactions and time-reversal symmetry in monolayer TMDCs, the interband optical transitions at K and K' valleys are allowed with opposite helicity of light along the *c*-axis[77-82]. The valley polarization, defined as the ratio of the difference over the sum of the emitted PL intensity with opposite helicity from two valleys, can reach a value of ± 0.32 for monolayer MoS_2 below 90 K, though it degrades remarkably at higher temperatures[83].

2.2 Crystal Structure of MoS_2

Like graphite, MoS_2 bulk crystals are also composed by stacking atomic S-Mo-S layers bonded by interlayer Van der Waals force[84]. Depending on different arrangements of Mo and S atoms, MoS_2 crystal has three common lattice structures, which are trigonal prismatic 2H-MoS_2, octahedral 1T-MoS_2 and distorted octahedral 1T′-MoS_2[85]. 2H-MoS_2 is more thermodynamically stable compared to its two counterparts, while a transition from 2H-MoS_2 to 1T-MoS_2 can be achieved by lithium and potassium intercalation[86-88] and electrochemical incorporation of sulfur vacancies[89]. The transition process, including numerous atomic displacements and plane gliding, requires the nucleation of an intermediate state (state α) and the migration of β- and γ-boundaries as examined by in situ scanning transmission electron microscopy (STEM) as reported in Ref[84]. Due to its semiconducting nature, mono- and few-

layer 2H-MoS_2 has long been the focus as another promising candidate after graphene for nanoelectronics and optoelectronics device research. In this work, MoS_2 used in the contents indicates 2H-MoS_2 by default unless otherwise mentioned.

2H-MoS_2 crystal with trigonal prismatic lattice structure is classified as C7 structure type in Strukturbericht designation with D_{6h}^4 group symmetry[87]. With three primitive translational vectors chosen as $\boldsymbol{t_1} = \frac{1}{2}a(\sqrt{3}\boldsymbol{i} - \boldsymbol{j})$, $\boldsymbol{t_2} = a\boldsymbol{j}$ and $\boldsymbol{t_3} = c\boldsymbol{k}$ ($\boldsymbol{i}, \boldsymbol{j}$ and $\boldsymbol{k}$ are unit vectors along x, y and z directions), the coordinates of Mo atoms in primitive unit cell are $\pm\left(\frac{1}{3}, \frac{2}{3}, \frac{1}{4}\right)$ and the corresponding S atoms are at $\pm\left(\frac{1}{3}, \frac{2}{3}, z - 1\right)$ and $\pm\left(\frac{1}{3}, \frac{2}{3}, \frac{1}{2} - z\right)$ with z = 0.621 as shown in Figure 2.1 according to Ref[75,87].

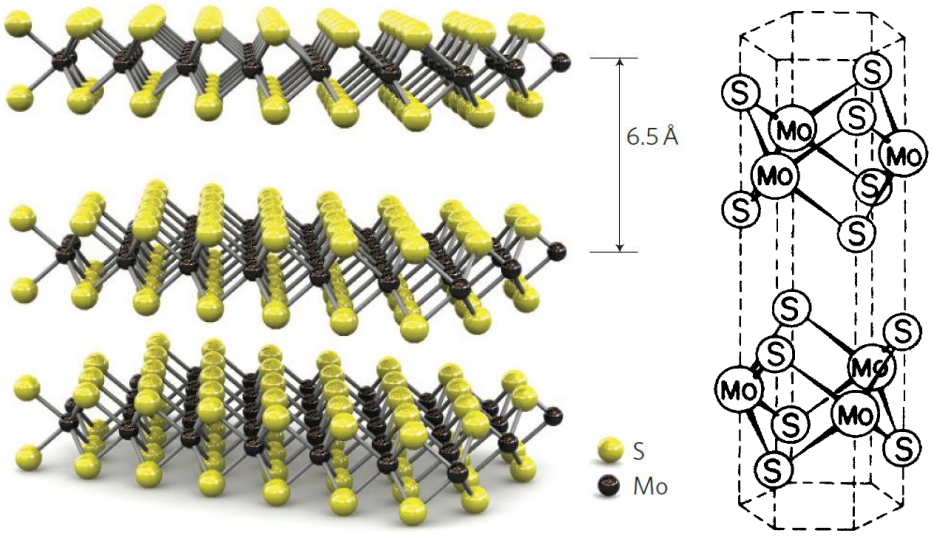

Figure 2.1 Lattice structure of MoS_2 crystal with symmetric unit cell. [75,87]

The first Brillouin zone for 2H-MoS_2 crystal has the same hexagonal symmetry with the three reciprocal lattice vectors to be $\boldsymbol{b_1} = \frac{2}{\sqrt{3}a}\boldsymbol{i}$, $\boldsymbol{b_2} = \frac{1}{\sqrt{3}a}\left(\boldsymbol{i} + \sqrt{3}\boldsymbol{j}\right)$ and $\boldsymbol{b_3} = \frac{1}{c}\boldsymbol{k}$ accordingly. Among these high symmetry points, the central point Γ and hexagonal corner points K (K') are of the most interest in band structure studies, since conduction and valence bands along Γ-K

determine both the direct band gap of monolayer MoS_2 and indirect band gaps of few-layer or bulk MoS_2.

2.3 Band Structure of MoS_2

Governed by the stacked layer crystal lattice structure, the band structure of MoS_2 few-layer or bulk crystals is naturally determined by contributions from both in-plane chemical bonds and out-of-plane interlayer van der Waals interactions. More specifically, the band structure near the Γ point is mostly cause by hybridization of out-of-plane Mo d-orbitals (d_{z^2}) and S p_z orbital, while near the K (K') point it is primarily composed of in-plane Mo d-orbitals (d_{xy}, $d_{x^2-y^2}$) and S p-orbitals[71,72,87,90-92]. As a result, band energy near the Γ point is most sensitive to interactions in the perpendicular direction such as the interlayer Van der Waals force. On the contrary, band structure near the K (K') point is only slightly influenced by interlayer interactions due to its in-plane orbital-hybridization composition.

This difference in orbital composition near the Γ and K (K') points is reflected in the interesting indirect to direct band gap transition, when the MoS_2 crystal is thinned down from bulk or few-layer to monolayer thickness[69-72]. As shown in Figure 2.2, bulk MoS_2 has an indirect band gap of 1.29 eV with the conduction band edge between the Γ and K (K') points and the valence band edge exactly at the Γ point. As the number of layer decreases, this indirect band gap increases substantially from 1.29 eV for bulk crystal to over 1.9 eV for monolayer MoS_2, while the direct band gap at the K point remains nearly unchanged (within only 0.1 eV variation) at around 1.9 eV for monolayer MoS_2, leading to the indirect-direct band gap transition[69,70,93].

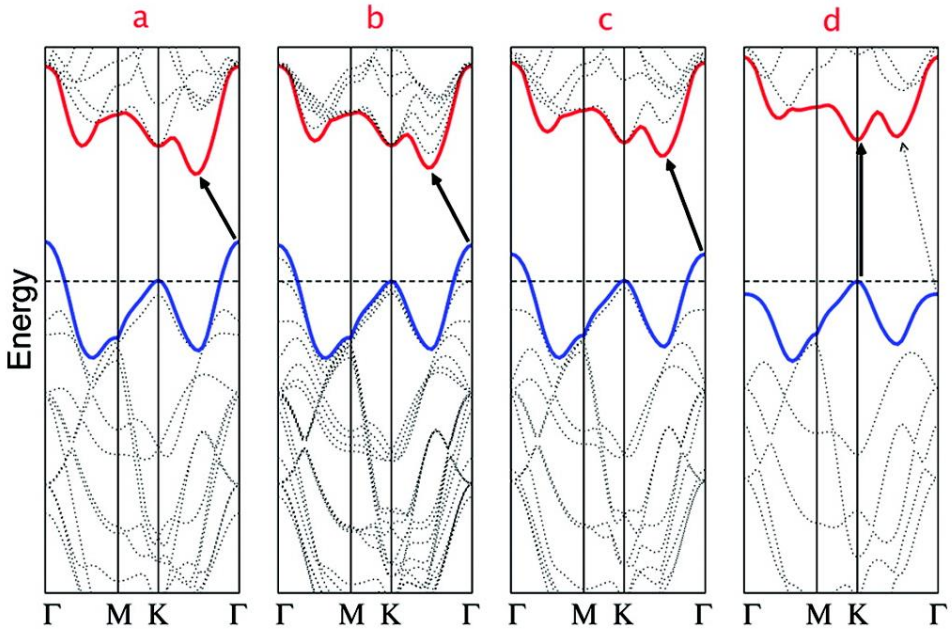

Figure 2.2 Calculated band structure for (a) bulk, (b) quadrilayer, (c) bilayer and (d) monolayer MoS_2 crystal respectively. Solid arrows stand for band gaps in the four cases, with a transition from indirect to direct band gap as the thickness shrunk down from bulk to monolayer. The splitting of valence band at K point due to spin-orbital coupling is not included in monolayer band structure. [93]

Besides the dramatic change in band gap, the valence band splitting at the K (K') point has also been observed, which leads to a double absorption peak around 1.9 eV for both monolayer and bilayer MoS_2[69] and at the same time double peaks in the PL spectrum of monolayer MoS_2[93]. This splitting at the K (K') point is also reported in numerical calculations with various algorithms such as the quasiparticle self-consistent GW method (QSGW)[94] and the screened hybrid functional of Heyd, Scuseria, and Ernzerhof[72]. For few-layer MoS_2 thin films, this splitting is ascribed to a combination of spin-orbital coupling (SOC) and interlayer interactions, while for monolayer MoS_2 the splitting is solely governed by SOC due to the lack of interlayer interactions[72,94].

More interestingly, due to time reversal symmetry for the K and K' points plus inversion symmetry breaking in monolayer MoS_2, valley and spin degree of freedom are coupled, which

leads to interesting and important phenomena in spintronics such as helicity-dependent light absorption[78,95]. For bilayer MoS_2, spin degeneracy of the conduction and valence bands at K and K' is, however, restored by inversion symmetry[78] as shown in Figure 2.3.

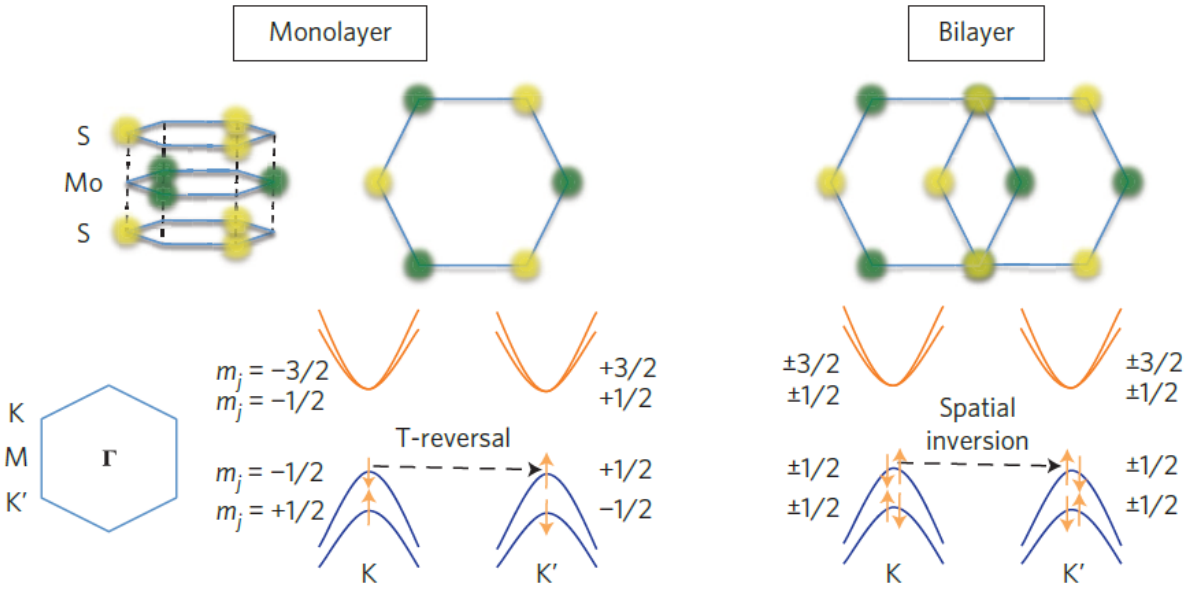

Figure 2.3 Valley spin coupled band structure at time-reversal K and K' valleys due to the lack of inversion symmetry in monolayer MoS_2 crystal (left). The spin degeneracy is restored at two valleys for bilayer MoS_2 crystal where inversion symmetry is maintained (right). [78]

2.4 Photoluminescence

The PL spectrum is an efficient and commonly used method for discriminating monolayer MoS_2 from few-layer or bulk crystals by the dramatic difference in their photon emission efficiency. An incident exciting laser with photon energy higher than the monolayer MoS_2 band gap is first aligned on the sample, which excites electron-hole pairs in the crystal. These excited carriers will subsequently relax and recombine to radiate, with the emitted photon energy typically determined by the difference between the band gap and exciton binding energies.

There are three main routes of electron-hole recombination that lead to few-layer or bulk MoS_2 PL – two through direct band gap transition at the K point considering valence band splitting,

and another through indirect band gap transition, which leads to a total of three peaks[69,93]. As the indirect band gap decreases along with increasing number of layers of MoS_2 thin films, the indirect-gap PL shows a red shift from 1.6 eV to around 1.4 eV, which is in good accordance with the indirect band gap value as shown in Figure 2.4[69].

For monolayer MoS_2, only direct transitions contribute to the PL. As reported by Ref[69], only one PL peak at 1.90 eV is observed for monolayer MoS_2 with an excitation laser wavelength of 532 nm, and it is ascribed to a direct transition at the H point. In Ref[93], however, two PL peaks are observed at 627 nm and 677 nm (with corresponding photon energy of 1.98 eV and 1.83 eV respectively) for monolayer MoS_2 under the same excitation laser wavelength, which is explained as a direct transition at the K point with spin-orbital splitting of the valence band.

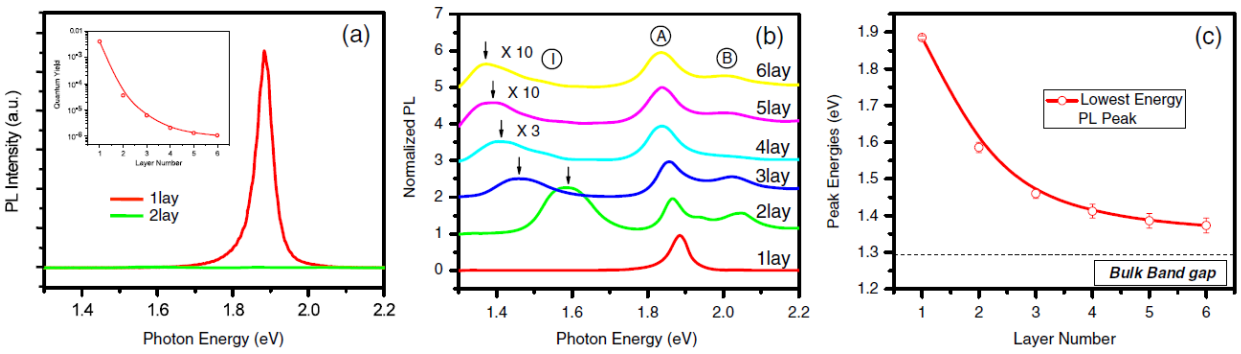

Figure 2.4 (a) PL intensity for monolayer and bilayer MoS_2 crystals. (b) Normalized PL intensity for monolayer to six layer MoS_2 thin films. Peaks due to direct transitions (A and B) and indirect transitions (I) are labelled for few-layer films. (c) The red shift in emitted photon energy agrees well with the band gap dependence on crystal layer number. [69]

Due to its direct band gap, monolayer MoS_2 has a high PL efficiency, which can reach 10^4 times that of its few-layer or bulk counterparts[69]. The high PL efficiency of MoS_2 can be explained with the formula[93]

$$\eta_{PL} = k_{rad}/(k_{rad} + k_{relax} + k_{defect})$$

where k_{rad}, k_{relax} and k_{defect} are carrier radiative recombination rate, intraband relaxation rate and defect trapping rate within the conduction and valence bands. k_{rad}, which is determined by the direct excitonic radiative transition, has little difference for monolayer, few-layer or bulk MoS_2 due to the fact that the band structure at the K point remains nearly unchanged. The intraband relaxation rate k_{relax}, however, has a significant dependence on crystal thickness. For bulk and few-layer MoS_2 crystals with an indirect band gap, k_{relax} is dominant due to the intraband relaxation to conduction band edge. As a result, bulk and few-layer MoS_2 crystals have much lower PL efficiency compared to monolayer MoS_2, whose relaxation rate k_{relax} is negligible, so that its efficiency is only limited by the defect trapping rate k_{defect}.[88,93]

2.5 Raman Spectrum

For bulk MoS_2 crystal, four first-order active Raman modes are E_{2g}^2 (32 cm^{-1}), E_{1g} (286 cm^{-1}), E_{2g}^1 (383 cm^{-1}) and A_{1g} (408 cm^{-1})[96]. Since the E_{2g}^2 mode represents the vibration of one S-Mo-S layer against other layers and the E_{1g} mode is forbidden in back-scattering measurements[96], these two vibration modes are not suitable for monolayer or few-layer MoS_2 Raman characterization. The remaining two vibration modes, E_{2g}^1 and A_{1g}, which originate from the in-plane opposite vibration of two sulfur atoms with respect to the molybdenum atom (E_{2g}^1) and the out-of-plane vibrations of two sulfur atoms opposite to each other (A_{1g}), are typically utilized as the two characteristic peaks in the Raman spectrum for MoS_2 thin films[96,97]. The distance between the E_{2g}^1 and A_{1g} peaks decreases with the thinning of MoS_2 thin films, as shown in Figure 2.5, which is commonly used as a quick estimation for number of layers of MoS_2 thin films. While the E_{2g}^1 peak exhibits a red shift, with an increase of 2.2 cm^{-1} from bulk to monolayer MoS_2, the A_{1g} peak instead shows a blue shift, with a 4.1 cm^{-1} decrement under

532 nm excitation laser[96]. For monolayer MoS_2, the peak distance is usually reported to be less than 20 cm^{-1} with a relatively small deviation in Raman peaks, while for bulk crystals it can reach a value as high as 24.8 cm^{-1}[96,98,99].

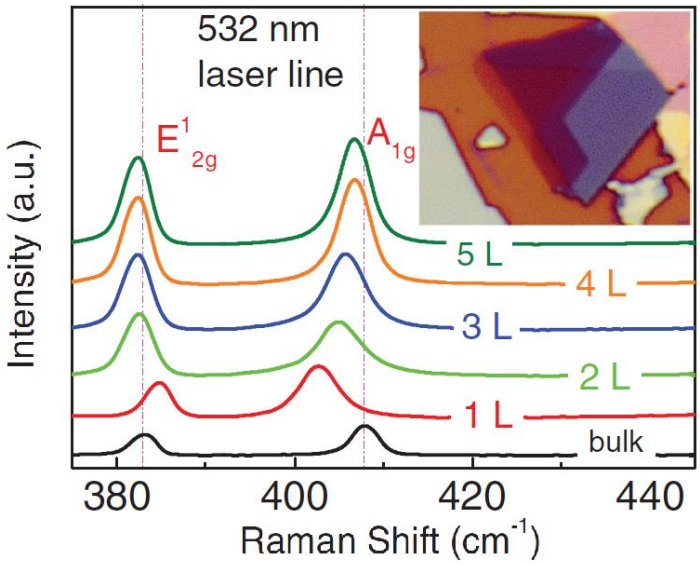

Figure 2.5 Raman spectrum for monolayer, few-layer and bulk MoS_2 crystal. Red shift in E^1_{2g} peak and blue shift in A_{1g} are observed with the thinning down of MoS_2 crystal. [96]

Chapter 3 MoS_2 Chemical Vapor Deposition Growth

3.1 MoS_2 Growth Introduction

As a representative material for TMDCs, monolayer or few-layer MoS_2 crystals have been widely studied and commonly applied for novel solid state devices applications. The synthesis of high-quality MoS_2 at desired thicknesses naturally has become one of the top priority research topics. Various synthesis methods, such as mechanical exfoliation, CVD and metal organic chemical vapor deposition (MOCVD) have been developed, with each synthesis method emphasizing a certain aspect of growth quality, such as high electrical mobility or a large growth area.

Monolayer or few-layer MoS_2 thin films can be mechanically exfoliated from bulk crystal due to the stacking layer nature of bulk MoS_2, the same as the exfoliation of graphene from graphite. Exfoliated monolayer or few-layer MoS_2 thin films generally possess better electrical quality indicated by their relatively higher carrier mobility. Though room temperature mobility of exfoliated monolayer MoS_2 may be in a lower range of 0.1 - 10 $cm^2/(V \cdot s)$ on SiO_2/Si substrates due to the limitation of phonon scattering[74,75], the mobility can be boosted up to 250 $cm^2/(V \cdot s)$ by dielectric screening with a high-k gate dielectric (30 nm atomic layer deposited hafnium oxide)[75,100], which is close to the bulk mobility value with a range of 200 - 500 $cm^2/(V \cdot s)$ at room temperature[101].

Exfoliated MoS_2 thin films, however, suffer from non-scalability due to their small and irregular crystal size. For such exfoliated samples, electron beam lithography is typically used in the fabrication process and batch production with photolithography is almost impossible, which

severely limits the use of exfoliated MoS_2 for device applications requiring scalability and cost-effectiveness in manufacturing.

CVD and MOCVD, on the other hand, synthesize MoS_2 with the bottom-up method from molybdenum and sulfur precursors. MOCVD, which typically uses metal-organic compounds as transitional metal precursors, is capable of growth of large-area monocrystalline MoS_2 flakes with a lateral size of up to 110 μm or even wafer-scale polycrystalline MoS_2 thin films[99,102]. Compared to CVD, MOCVD has better control over the evaporation process of its solid state precursors such as molybdenum hexacarbonyl ($Mo(CO)_6$), thus having advantages on growth reproducibility[99]. Decent room temperature carrier mobility up to 30 $cm^2/(V \cdot s)$ has been demonstrated, as extracted from FETs fabricated from MOCVD grown MoS_2 samples; this mobility value is reported about three times larger compared to that of CVD samples, and half of the value extracted from high-quality exfoliated samples as reported in Ref[102].

The drawbacks of the MOCVD method, however, are evident as well. An MOCVD system is more complicated and expensive compared to a CVD system. Moreover, precursors used in MoS_2 MOCVD growth can be extremely dangerous to human health – both molybdenum hexacarbonyl ($Mo(CO)_6$) and hydrogen sulfide (H_2S) can be fatal and thus place strict requirements for the operation environment.

While maintaining the merits of decent growth quality, simple operational procedures and affordable components, the CVD method also has relatively low toxicity of the precursors, and thus is typically chosen as the practical bottom-up method for MoS_2 synthesis. The lateral size of CVD grown monocrystalline MoS_2 flakes can reach as high as 123 μm[103], with wafer-scale growth of continuous MoS_2 film also reported[98], showing comparable or even slightly larger single crystalline growth area compared to MOCVD grown samples. The mobility of some CVD

grown samples can reach ~10 $cm^2/(V \cdot s)$[102,103]. Though the mobility still needs to be improved compared to the best ones prepared by MOCVD and exfoliation, this value is adequate for nanoelectronics and device applications.

3.2 MoS_2 Growth Key Parameters

CVD growth mechanisms may vary with the change of key growth parameters such as growth temperature, precursor amount, carrier gas, pressure, substrates and promoters, which leads to different nucleation processes and growth morphologies of MoS_2[104,105].

Typical CVD growth of MoS_2 begins with placing a certain amount of a solid-state molybdenum source (usually high purity MoO_3, MoO_2 or $MoCl_5$) and a sulfur source (pure sulfur powder) at desired positions in a quartz growth tube. As the temperature ramps up, the precursors get vaporized first and subsequently transport with the carrier gas, finally reacting with each other in the vapor phase and leading to the nucleation and growth of the crystal. In the case where MoO_3 and sulfur powders are used as precursors, the temperature of the MoO_3 powder and substrates is typically set in the range of 650 to 800°C for MoS_2 crystal growth. The sulfur powder is set at a relatively lower temperature, which is typically slightly higher than the sulfur melting point for desired vaporization. Besides the vaporization rates of precursors, growth temperature also plays an important role in growth morphology by controlling kinetics and thermodynamics during growth, with a higher temperature contributing to thicker growth[104,105].

The ratio of molybdenum and sulfur source concentrations is another key parameter in the nucleation and growth pattern. Based on the reactant concentration ratio, intermediate volatile $MoO_{3-x}S_y$ particles or fully reacted MoS_2 can be formed through vapor phase chemical reactions[104,105]. The former can be further sulfurized and react on the substrate to form

nucleation centers, with few-layer MoS_2 growth preferred[104,106,107]; in the latter case, however, MoS_2 species formed by vapor reaction deposit directly onto the substrate surface, with further crystal edge growth leading to extension of growth into monolayer or bilayer thin films[104,108]. Along with the impact on growth morphology, this ratio also leads to different growth shapes and edge terminations. With a molybdenum-to-sulfur ratio higher than 1:2, Mo zigzag terminations dominate the edge of grown MoS_2 triangular flakes due to the faster growth rate, while S zigzag terminations dominate when the ratio falls below than 1:2. When the ratio is exactly1:2, which is the stoichiometric ratio of MoS_2, it will lead to a hexagonal instead of triangular crystal shape with three sides dominated by each element[109].

Various promoters for MoS_2 CVD growth have also been proposed for easier nucleation and/or faster growth rate. Sodium chloride (NaCl), for example, is an effective and universal promoter for thin films growth within the TMDC library. Added and mixed with transitional metal precursors, the salt melts at high temperatures, reducing the melting point of metal oxides and forming oxychlorides, thus leading to a higher growth rate[110]. Organic seeding promoters such as $F_{16}CuPc$, Perylene-3,4,9,10-tetracarboxylic dianhydride (PTCDA) and its water-soluble derivative perylene-3,4,9,10-tetracarboxylic acid tetrapotassium salt (PTAS) are also reported with overall good or excellent growth results, suggesting a correlation between higher seeding concentration and denser nucleation sites with smaller grains[111].

During CVD growth operations, SiO_2 or sapphire substrates can be either placed in the downstream of the molybdenum source with a clean surface facing upwards[98,111] or placed directly on the molybdenum source combustion boat with a clean surface facing downwards[103,109], with each configuration capable of producing decent monolayer MoS_2 growth, despite the difference in the vapor transfer process. Similarly, low pressure CVD

(LPCVD) and atmospheric pressure CVD (APCVD), though with different impacts on vaporization rate, gas flow rate, etc., are both reported effective for high quality MoS_2 growth as long as appropriate growth conditions have been achieved[98,103,109,111].

3.3 Large Area Polycrystalline MoS_2 CVD Growth

3.3.1 Growth Conditions

A three-zone heating furnace (model: MTI® OTF1200X) with a 4-inch diameter quartz tube is used for MoS_2 CVD growth, together with a four channel gas control system (model: MTI® EQ-GSL-LCD) for inlet gas flow control and a turbo pump station (model: MTI® EQ-PAC-LD) for pressure control as shown in Figure 3.1. A combustion boat containing 18 mg MoO_3 powder is placed at the center of the right heating zone, with 0.5 g sulfur powder placed in close proximity to the right zone. A clean substrate (typically a 285 nm dry grown SiO_2/Si piece) is placed directly on the MoO_3 combustion boat, with the clean surface facing downward. No significant difference in growth morphology has been observed between clean substrates after dry oxide growth and those with an extra acetone/2-propanol sonication and/or Piranha cleaning (H_2SO_4: H_2O_2 = 3:1). The schematic setup for large area polycrystalline monolayer MoS_2 CVD growth is shown in Figure 3.2.

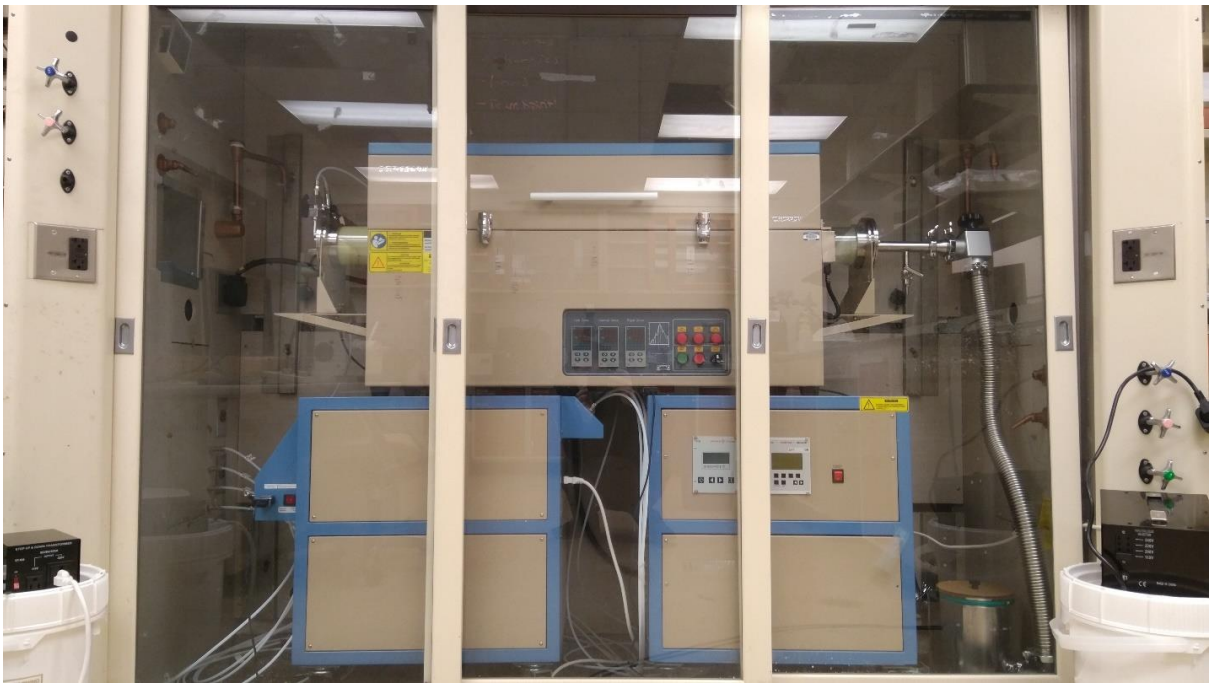

Figure 3.1 CVD equipment for MoS_2 growth, mainly consisting of the three-zone heating furnace (top), the gas control system (bottom left) and the turbo pump station (bottom right).

Before the growth, the whole system is first pumped down to 2 mTorr to remove remnant gases inside the system, and both MoO_3 and sulfur powders are subsequently dehydrated at 115 °C for 20 ~ 30 min at 1.1 Torr with an argon flow rate of 200 sccm. After the dehydration process, the quartz tube is filled with argon to achieve atmospheric pressure for later MoS_2 growth. The right heating zone is subsequently heated from 115 °C to 700 °C with a 15 °C/min ramp rate and held at 700 °C for 10 min before cooling down naturally to room temperature. The target temperatures of the left and central zones are set equally to 180 °C, with a corresponding ramping rate of 1.67 °C/min. The flow rate of argon carrier gas during ramping up, growth and cooling down process is kept constantly at 700 sccm. During the whole growth process, pressure is kept slightly above atmospheric pressure by setting argon inlet gas at a pressure ~2 psi above atmosphere with the turbo pump station kept in an idle state.

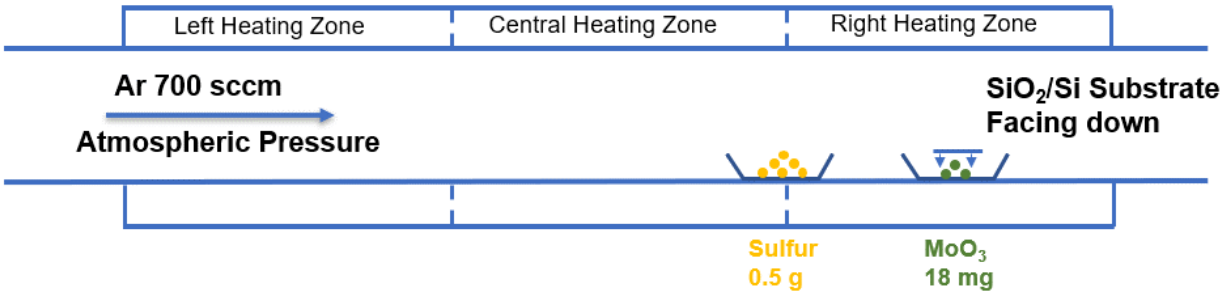

Figure 3.2 CVD setup for large area polycrystalline continuous monolayer growth of MoS_2. APCVD together with substrate facing downward configuration is used for the growth.

3.3.2 Characterizations

Grown samples are first examined by optical microscope, Raman spectroscope and scanning electron microscope (SEM) respectively. In addition, PL of the samples is measured to confirm the monolayer MoS_2 growth, due to its high PL efficiency which is typically used to distinguish monolayer MoS_2 from its few-layer or bulk crystals.

The optical images and corresponding Raman spectra measured at the center spots of each image are presented in Figure 3.3 and Figure 3.4 respectively. There is an evident decreasing trend in grown MoS_2 thickness from the excessive growth region (image 1) to the insufficient growth region (image 6), as indicated by the significant change in color. Under an optical microscope, the excessive growth regions show a blue background, covered with bright and dense yellow dots originating from thicker vertically grown MoS_2 crystals. With the growth pattern gradually shifting to continuous monolayer MoS_2 crystal growth, the yellow dots fade away accordingly, leaving the blue color from thinner MoS_2 crystals standing out. When the growth continues to diminish, only a small portion of area remains recognizable with a light blue color before finally no color contrast against the substrate can be clearly seen.

The decrease in MoS_2 growth from the excessive to the insufficient growth region is also reflected in the corresponding Raman spectra. As discussed in the previous chapter, the Raman

shift distance between E_{2g}^{1} and A_{1g} peak can be used as a characteristic index for the estimation of MoS_2 thickness, since the two peaks will become closer along with the decrease in crystal thickness. Moving the Raman measurement point from the excessive growth region (spot 1) to the insufficient growth region (spot 6), though limited by the resolution (~4.27 cm^{-1}) of the Raman equipment, a clear trend with decreasing Raman peak distance can be observed as presented in Figure 3.4. This trend is in good accordance with bulk, few-layer and monolayer MoS_2 Raman spectrum reported in Ref[96].

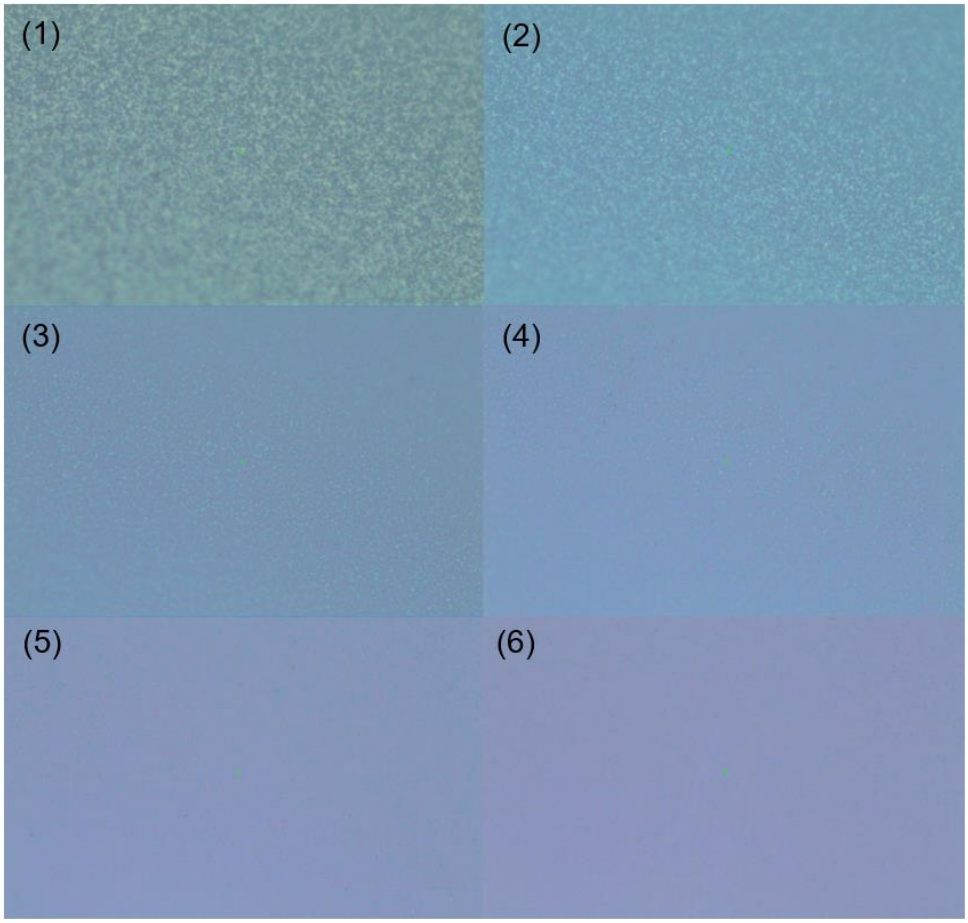

Figure 3.3 Optical images of different MoS_2 growth regions. From image (1) to image (6), the growth of MoS_2 gradually decreases, showing a transition from excessive growth region to insufficient growth region. The green dots in the center of images are examined with Raman spectroscope.

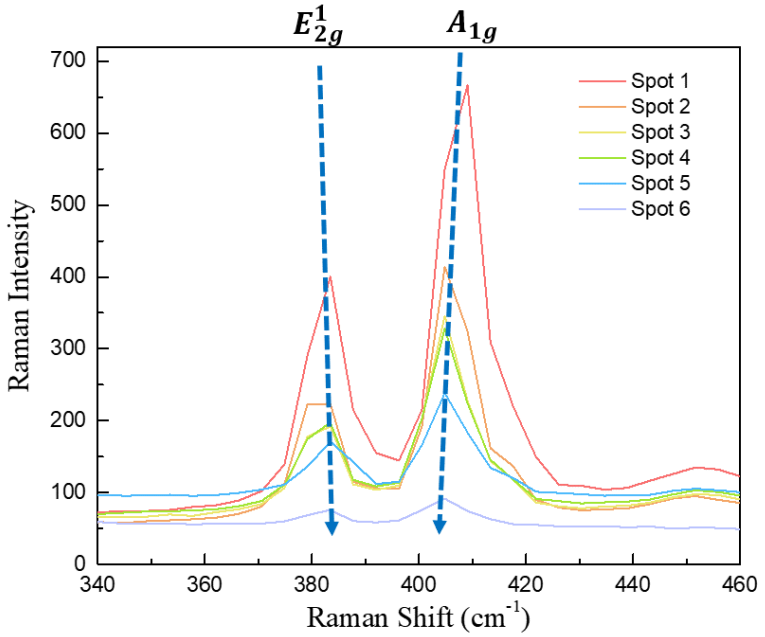

Figure 3.4 Corresponding MoS_2 Raman spectrum measured at the center point of region (1) to region (6) shown in Figure 3.3. Red shift of E^1_{2g} peak and blue shift of A_{1g} peak have been observed from excessive growth region (spot 1) to insufficient growth region (spot 6).

The growth morphology is further examined by SEM. From SEM images, it is seen clearly that overgrown MoS_2 at excessive growth regions is composed by densely packed and stacked tiny crystals. These tiny crystals have a characteristic triangular shape, with edge length around 1 ~ 2 μm. For insufficient growth regions, discrete and single crystalline monolayer MoS_2 crystals are dominant, while sparsely distributed on substrate surface. Though the size remains 1 ~ 2 μm as in the excessive growth region, the thickness of these rounded triangle-shaped crystals is shrunk to monolayer thickness. In particular, these discrete flakes can further merge into a continuous monolayer film, though scattered sparsely with tiny holes and thick spots.

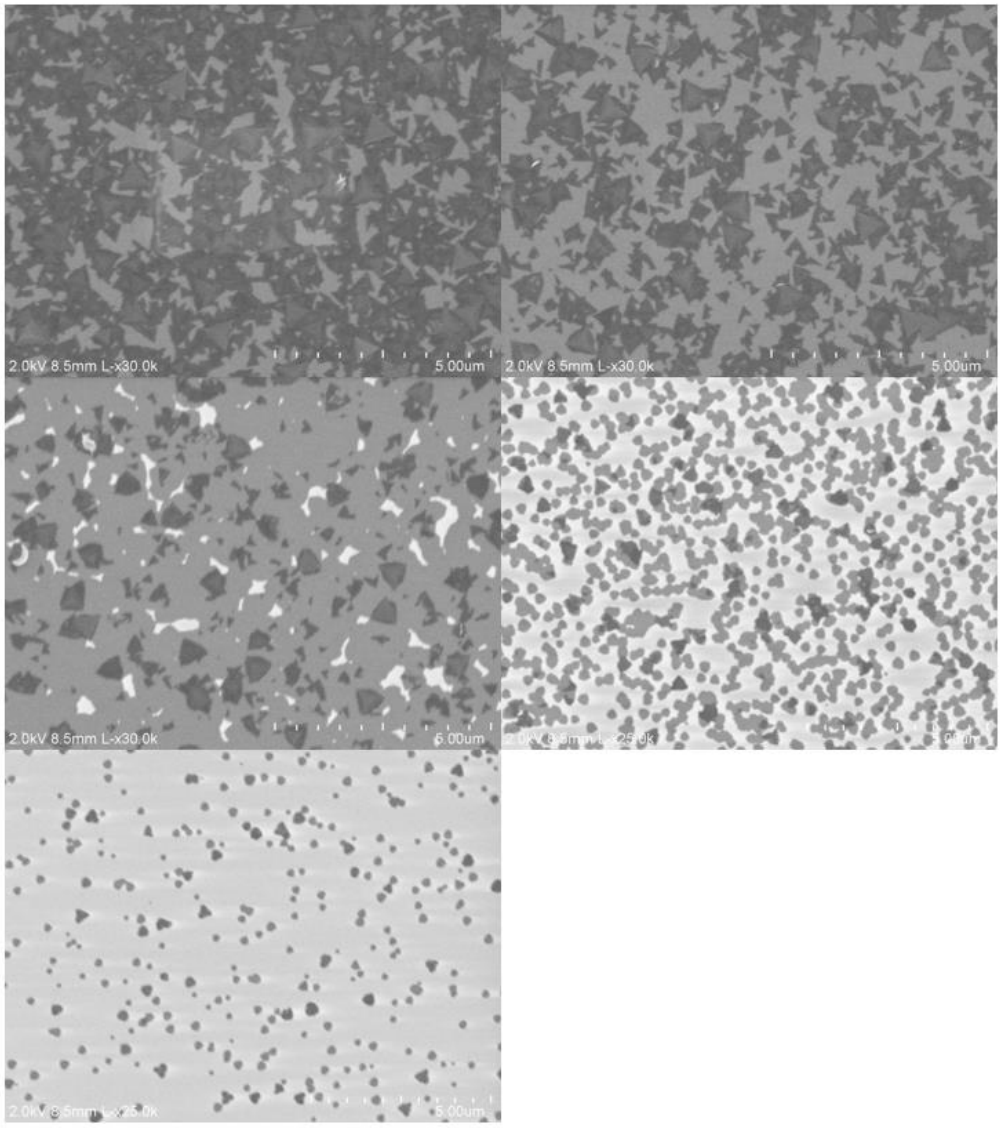

Figure 3.5 SEM images of large area MoS_2 growth, with a transition left to right and top to bottom from excessive growth regions to monolayer growth regions, and finally to insufficient growth regions.

While AFM is a powerful tool in determining the thickness of 2D materials by measuring the step height across the boundary, it is not suitable for characterizing a continuous thin film. PL measurement, instead, is a fast, convenient and convincing method for large area continuous sample characterization and is utilized here to confirm the monolayer MoS_2 growth. Electron-hole pairs in MoS_2 samples are first excited by a He-Ne laser source ($\lambda = 632.8$ nm), with

emitted photons subsequently collected by a spectrometer (model: iHR550). The PL spectrum of MoS_2 samples peaks at 656 nm, which agrees well with the reported optical band gap of monolayer MoS_2 at 1.88 eV[69].

The PL spectra at different growth regions are integrated in Figure 3.6 for the same sample examined by SEM previously, with the labels from left to right representing the trend from excessive to insufficient growth region. From PL spectra, the excessive growth region (labelled as left) only shows a negligible peak intensity due to the low PL efficiency of thick, overgrown MoS_2 crystals. As the overgrown region fades away (central left) and continuous monolayer growth becomes dominant (central), the PL intensity goes up rapidly, with a significant peak at 656 nm for monolayer growth region. As the growth becomes weaker and weaker, the PL intensity drops quickly as the coverage of monolayer MoS_2 decreases (central right), and finally returns to negligible level for regions with nearly no growth (right).

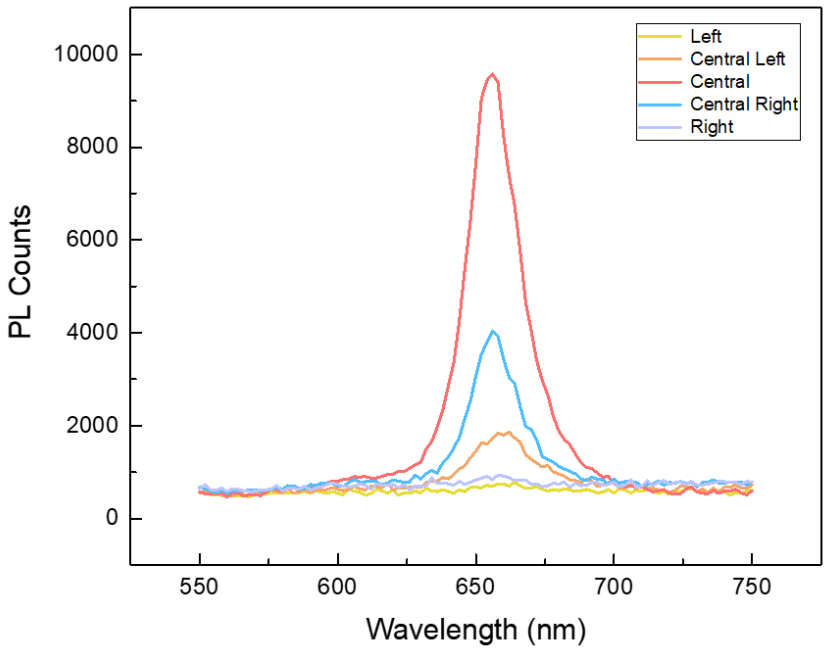

Figure 3.6 PL spectra at different growth regions for large area monolayer MoS_2 sample. Left to right is from overgrown to undergrown. Central is the region of monolayer MoS_2 with most complete coverage.

3.3.3 Electrical Measurements

Due to the benefit of large area growth, an MoS_2 FET with centimeter-scale channel dimension can be readily fabricated. In order to minimize gate leakage, an extra layer of 80 nm ALD Al_2O_3 is deposited on clean 285 nm dry SiO_2/Si substrate before growth. Contacts for MoS_2 (5 nm Mo/50 nm Au) are first put down by electron beam evaporation and a metal lift-off process, followed by the patterning of the MoS_2 thin film into a 0.5 cm by 0.5 cm square by XeF_2 plasma reactive ion etching (RIE). The oxide layer on the backside of the silicon substrate is removed with buffered HF, and 5 nm Cr/50 nm Au is immediately deposited as the back gate electrode. After device fabrication, electrical measurements are carried out in a dark environment to exclude the influences from photocurrent.

The transfer curve of the centimeter-scale MoS_2 FET is presented in Figure 3.7, with source-drain bias, V_{ds}, set at 10 V and the back gate voltage, V_{gs}, scanned from - 80 V to 80 V, showing a typical n-type behavior. The two-terminal mobility of the device is extracted from the n-MOSFET transfer characteristics[12,54]

$$I_{ds} = \mu C_{ox} \frac{W}{L}\left(V_g - V_{th} - \frac{1}{2}V_{ds}\right)V_{ds}$$

where C_{ox} is the gate capacitance per unit area and V_{th} is the threshold voltage. Using data points at 80 V and 60 V gate voltage, the mobility is estimated to be 0.42 $cm^2/(V\cdot s)$ or 0.35 $cm^2/(V\cdot s)$ due to the hysteresis in the transfer curve. Even though this value is orders of magnitude smaller than that of a high-k dielectric encapsulated exfoliated MoS_2 FET[75], it is acceptable compared to the mobility of CVD grown MoS_2 samples typically ranging from 0.1 ~ 10 $cm^2/(V\cdot s)$[75,103], especially when considering the centimeter-scale size of the device.

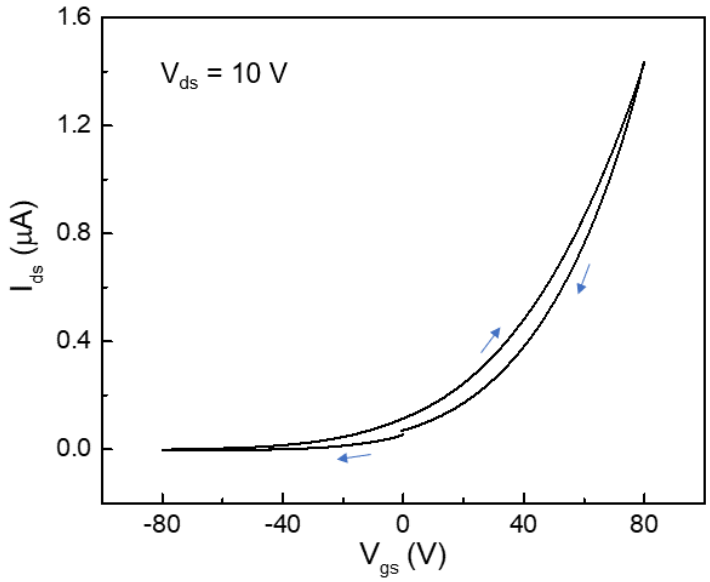

Figure 3.7 Transfer curve of MoS_2 FET with centimeter-scale channel dimension.

3.4 Single Crystalline MoS_2 CVD Growth

3.4.1 Growth Conditions

The CVD growth of single crystalline MoS_2 is also accomplished with the same system, but with a different growth setup. Besides the lowering of growth temperature, relocation of precursor combustion boats with adjusted chemical amounts and the change in substrate position and orientation, there is also a major transition to LPCVD from the APCVD method used previously for large area polycrystalline growth.

Molybdenum (VI) oxide (MoO_3) and sulfur powders are still chosen as precursors, but are placed at different positions: a combustion boat containing 15 mg MoO_3 is placed in the center of the central heating zone lifted by an aluminum oxide holder, while another combustion boat containing 200 mg sulfur is placed in proximity to the upstream entrance of the furnace. Multiple dry grown 285 nm-thick SiO_2/Si substrates are placed in the downstream up to 25 cm from MoO_3 boat as shown in Figure 3.8. The substrates are also placed on the aluminum oxide

holders, with the clean surface facing up after a treatment of acetone/2-propanol sonication and Piranha cleaning (H_2SO_4: H_2O_2 = 3:1).

Before growth, the CVD system is pumped down to 2 mTorr to remove gases from the whole system. Argon carrier gas is subsequently delivered at a constant flow rate of 200 sccm, with a corresponding pressure of 1.05 Torr during the whole growth process. The central and right heating zones are programmed to ramp up from 0 °C to 660 °C in a 34 min heating period, with a corresponding ramp rate of 19.4 °C/min, followed by a 20 min hold time at 660 °C for MoS_2 crystal growth. Meanwhile, the left zone is programmed to heat up from 0 °C to 150 °C in 10 min, heat to 250 °C in another 10 min, hold at 250 °C for 9 min, and finally ramp up to 380 °C in 6 min. After reaching 380 °C, the left zone is also held for 20 min at this temperature for sulfur evaporation. After the simultaneous 20 min-long hold time of all the three heating zones, the system is naturally cooled down to room temperature with the same argon flow rate and pressure.

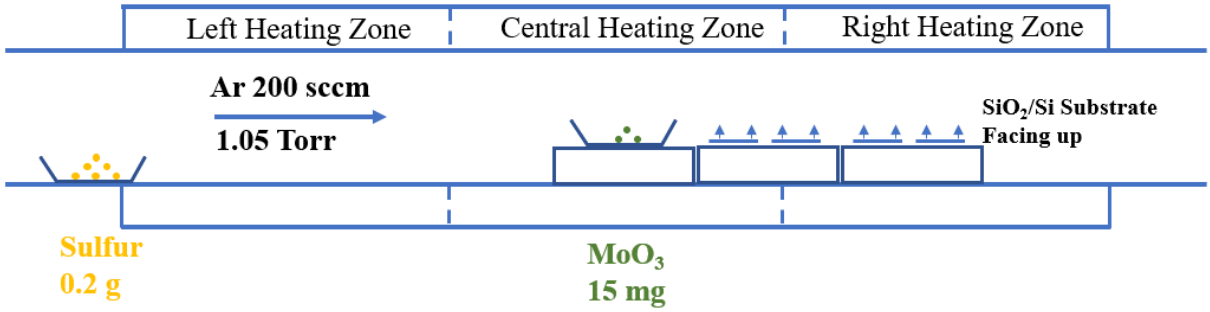

Figure 3.8 Conditions for single crystalline MoS_2 CVD growth.

3.4.2 Characterizations

The LPCVD growth result is first examined under an optical microscope, and monolayer/few-layer MoS_2 can be clearly distinguished due to the difference in their optical contrast against the 285 nm-thick SiO_2/Si substrate.

Triangular MoS_2 flake growth has been observed, with the lateral length up to 10 ~15 μm as shown in Figure 3.9. The grown flakes, however, vary in thickness from monolayer to few-layers, showing a stacking and/or merging growth morphology. Few-layer MoS_2 crystal growth prevails for most areas, with isolated monocrystalline monolayer sparsely distributed. With the help of SEM, the features of the tiny, thick-grown crystals are also observed in detail as shown in Figure 3.9. These vertically grown tiny crystals show irregular shapes with a characteristic crystal core in the center, possibly originated from the incompletely sulfurized $MoO_{3-x}S_y$ nanoparticles which act as nucleation centers[104,106,107].

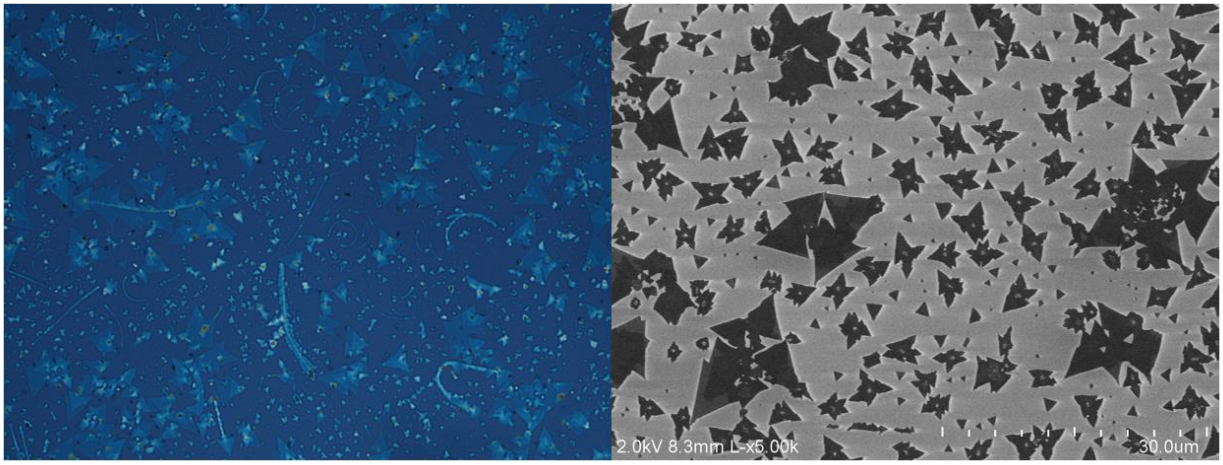

Figure 3.9 Optical (left) and SEM (right) image of grown MoS_2 samples.

The Raman spectrum of the triangular monolayer MoS_2 flake has also been measured, with an excitation laser wavelength at 532 nm as presented in Figure 3.10. For thick few-layer growth, the Raman peak distance between the E^1_{2g} and A_{1g} peaks, which can reach as high as 24.8 cm^{-1}, is evidently larger compared to monolayer MoS_2 crystal with a typical value reported less than 20 cm^{-1}[96,98,99]. The two characteristic Raman peaks are measured respectively to be at 384.8 cm^{-1} and 401.9 cm^{-1}, with a distance of 17.1 cm^{-1}. This distance value is smaller than typically reported values due to errors caused by the resolution limit (~4.27 cm^{-1}) of the Raman

apparatus. With a further triangulation fitting for the A_{1g} peak, the distance is estimated to be 18.0 cm^{-1}, which is a strong evidence for the monolayer MoS_2 growth.

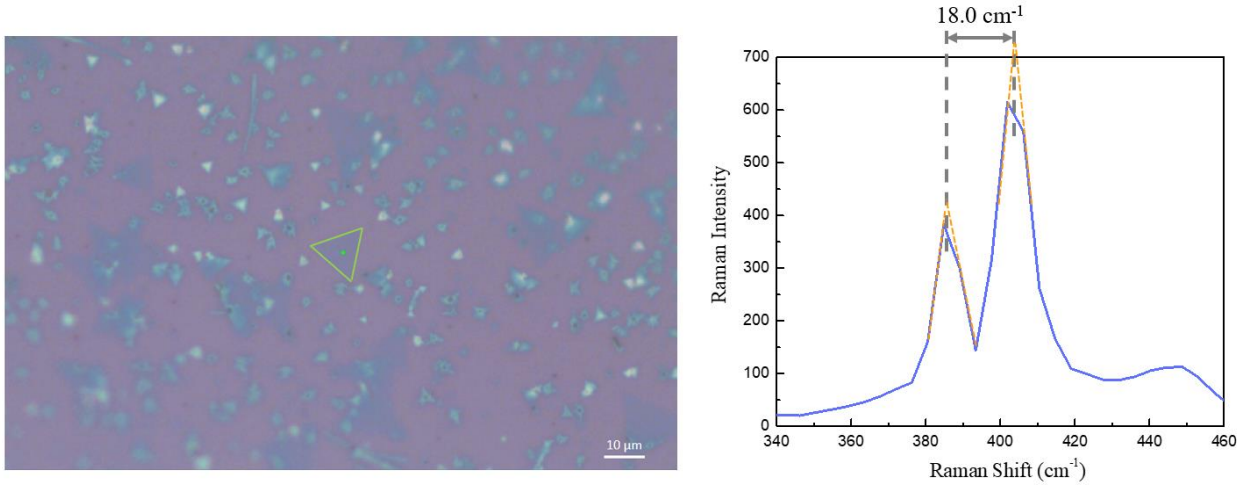

Figure 3.10 Raman spectrum (right) for a triangular monolayer MoS_2 flake, with the measured spot represented by the green dot in corresponding optical image (left).

AFM is a powerful and precise tool to acquire the size, shape and thickness of a two-dimensional crystal, especially suitable for grown MoS_2 flakes with triangular boundaries. Aside from height mapping, phase information from AFM is also recorded for shape recognition. Since the phase of cantilever oscillation reflects measured material properties such as adhesion or stiffness, the phase diagram is another ideal way for differentiating grown MoS_2 crystals from the SiO_2/Si substrate, even for samples which suffer relatively large noise in height mapping.

Triangular MoS_2 flakes can be readily observed under AFM, with the height mapping shown in Figure 3.11. Along with the line across the flake, the step height is extracted as 0.6 ~ 0.7 nm, which agrees well with the monolayer MoS_2 thickness of ~ 0.65 nm as reported in Ref[112], confirming the growth of monolayer MoS_2.

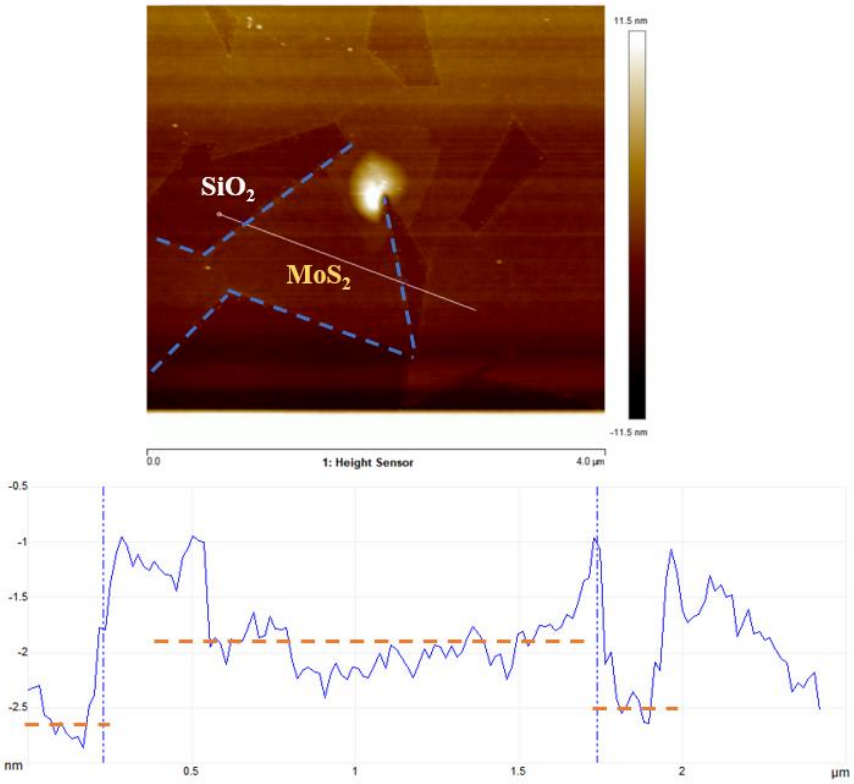

Figure 3.11 AFM height mapping of MoS_2 sample (top), with step height across the boundaries extracted (bottom).

3.5 Conclusion

This chapter presents the CVD method for monolayer MoS_2 growth. Both large-area continuous polycrystalline thin film growth and isolated monocrystalline flake growth have been demonstrated with corresponding growth configurations. Various characterization methods such as optical microscopy, PL, Raman spectrum, SEM and AFM are subsequently utilized to examine the growth quality. For large area grown samples, mobility is further extracted from a corresponding centimeter-scale FET with acceptable values.

Chapter 4 Lateral Structured Graphene-Si-Graphene Bipolar Junction Transistor with Electrically Tunable Gain

4.1 Introduction

Graphene consists of sp^2 hybridized carbon atoms with a honeycomb structure, forming a two-dimensional atomically thin crystal[7,10,113]. It has been proved to be an excellent material for electronic device applications such as thin film transistors and atomically thin junction studies, due to its single-atom thickness and convenient large area CVD growth[36,37,114] as well as simple wet transfer [115,116] or even roll-to-roll transfer process[117,118]. Uniquely, the crystal structure of graphene also leads to a linear dispersion relation with zero band gap at the K and K' points called a Dirac cone[10]. The density of states (DOS) of graphene near the charge neutral point, or Dirac point is $\rho(E) = \frac{2|E|}{\pi v_F^2}$, where E is the energy deviation from the Dirac point and v_F is the Fermi velocity with a value around 1×10^6 m/s[10,11]. This graphene DOS is far smaller compared to the constant DOS of other 2D semiconductors with parabolic dispersion relations, or that of 3D semiconductors with $\rho(E) \propto \sqrt{E}$ dependency[119]. This unique semi-metal DOS of graphene results in a great tunability of the Fermi level for various electrical applications[120-123]. Specifically, by controlling the graphene Fermi level simply by electrodes through the gating effect, the Schottky barrier height formed between graphene and silicon can be tuned, leading to a barristor with an on/off ratio larger than 10^5 as reported in Ref[50]. This tunability is universal for other graphene Schottky junctions such as graphene/GaAs,

generalizing a widely applicable feasibility for graphene heterojunction barrier height tunability[49].

The graphene FET is also a representative device of this advantage, utilizing the gating effect to tune the Fermi level, carrier density and even polarity[7,120,122,123]. The small alternating current gain of most graphene FETs, however, is not sufficiently high. The best current gain can be pushed extremely to 100 after the de-embedding for a epitaxially grown graphene FET with high-k dielectric[124], though a previous work reports the fact that gain of another good exfoliated graphene FET drops from around 30 after the de-embedding to only 7 before de-embedding[125]. Graphene FET, also in another way, can hardly achieve a direct current gain due to insulating gate oxide from its metal-oxide-semiconductor (MOS) structure. Here we report a lateral structured graphene-Si-graphene bipolar junction transistor (BJT) with its direct current gain easily tuned by gate electrodes. The best current gain of our graphene BJT device can be pushed over 20 with large bias voltages as shown in the Gummel plot – though the gain in the common emitter amplification mode is smaller. Uniquely, with a top gate controlling the emitter graphene Fermi level, graphene BJT devices can be electrically tuned smoothly from zero current gain to the current amplification operating mode.

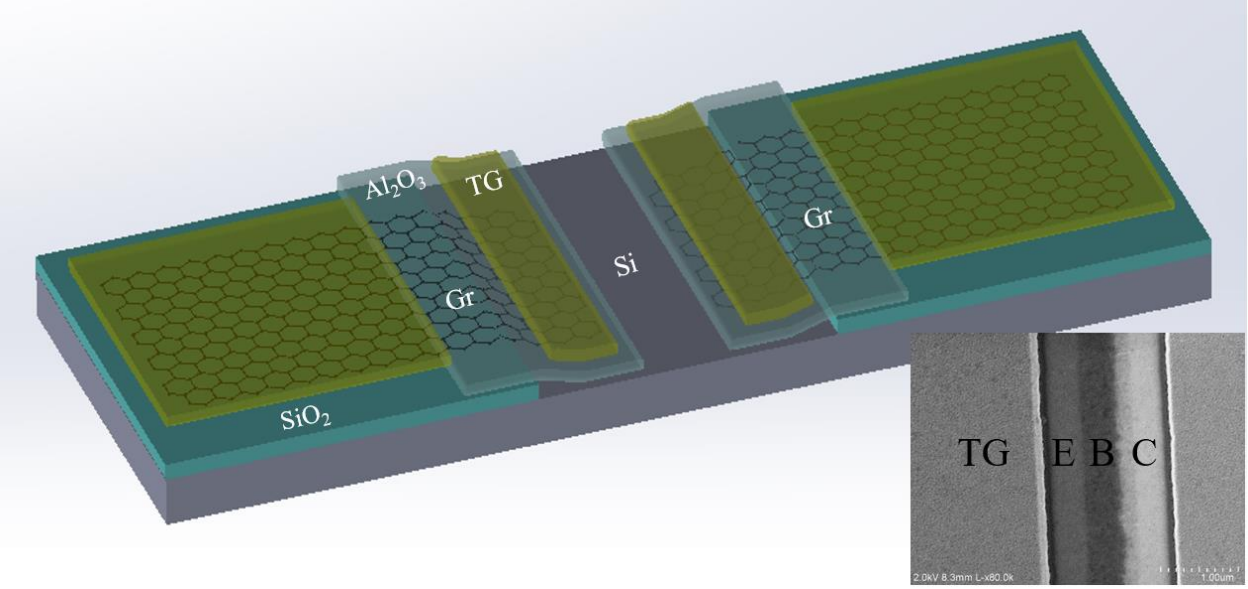

Figure 4.1 Schematic and SEM image (inset) of graphene-Si-graphene BJT device, with emitter top gate (TG), graphene emitter (E) and collector (C) and silicon base (B) labelled. Silicon base contact is not shown for a clear view.

4.2 Device Fabrication

The graphene BJT fabrication process begins with 100 nm-thick SiO_2 dry growth on a lightly p-doped silicon wafer (10^{15} cm^{-3} boron doped, with a resistivity of 10 ~ 20 Ω·cm) and followed by photolithography patterning and buffered hydrofluoric acid (BHF) wet etching. 5 nm/50 nm Cr/Au is then e-beam evaporated and annealed in forming gas to form the silicon base contact. The substrate is dipped in BHF for a few seconds right before the graphene transfer to remove the native oxide for better junction quality. Graphene is subsequently transferred to this patterned SiO_2/Si wafer using a PMMA-assisted wet transfer process, forming a graphene-silicon junction. Another 5 nm/50 nm Cr/Au layer is evaporated as the contacts for the graphene emitter and collector. Oxygen plasma is used to etch a 0.75 μm-wide thin strip of graphene in the center with photolithography, separating the graphene emitter and collector and forming the thin silicon base channel. The part of the graphene emitter/collector in overlap with silicon is 200 μm by 2 μm in size. Finally, 25 nm Al_2O_3 is deposited by atomic layer deposition (ALD) as the top

gate dielectric with 5 nm/50 nm Cr/Au put down as the top gate electrodes. The schematic and SEM images of the graphene BJT device are shown in Figure 4.1 and inset correspondingly.

4.3 Characterization

The graphene emitter-silicon base junction is first characterized under different top gate voltages and analyzed with the corresponding junction band structure. Since the work function of undoped graphene is near the center of silicon's bandgap[49,126], the electron barrier height Φ_{Bn}, determined by the difference of graphene's Fermi level and electron affinity of silicon in an ideal case would be small for an electron to overcome. This barrier could be further smaller considering the n-type doping effect to graphene contributed by the Cr/Au metal contact pinning[126] and/or the possible Fermi level pinning effect due to interface states from silicon dangling bonds and graphene edge defects[12]. The electron current, originating from overcoming the barrier height Φ_{Bn} from the graphene emitter to the silicon base, can thus form a considerable conducting channel. This electron current may be comparable to or even higher than the hole current described by Schottky junction thermal emission theory[12,50], especially when taking the small concentration of dopants (~10^{15} cm^{-3}) in the p-doped silicon base into consideration. The existence of the electron conducting channel is indicated by the rectification curves under various emitter gate voltages (V_{tg}) as shown in the following Figure 4.2 and Figure 4.3.

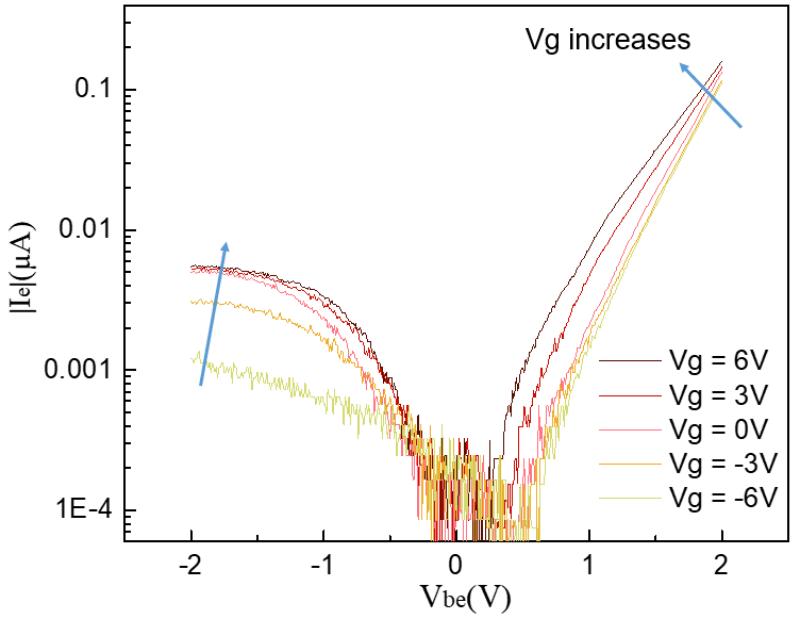

Figure 4.2 Rectification curves of graphene-Si junction under different top gate voltage V_{tg}.

In Figure 4.2, the graphene emitter/p-type silicon base Schottky junction current is characterized under various graphene top gate voltages (V_{tg}). The trend of junction current change with V_{tg} with a base-emitter bias (V_{be}) of 2V is also presented in Figure 4.3 for a clearer comparison. In both figures, the junction current increases with increasing V_{tg}, indicating that electron injection over the barrier Φ_{Bn} should be the main mechanism for this current increment. At a large V_{be} bias, the silicon band bends severely downwards, with an electron injection current governed by Φ_{Bn}.With a positive V_{tg}, the graphene Fermi level is tuned higher due to the electrical gating effect, leading to a reduced Φ_{Bn} and subsequently larger electron current as described by band diagrams in Figure 4.3 inset. In the same way, for a negative V_{tg}, Φ_{Bn} is tuned higher and thus leads to a reduced electron injection current. On the other hand, the hole current is less dependent on gate voltage, especially compared with the distinct change of electron injection current. As a result, the total junction current change has an overall increasing trend with V_{tg}.

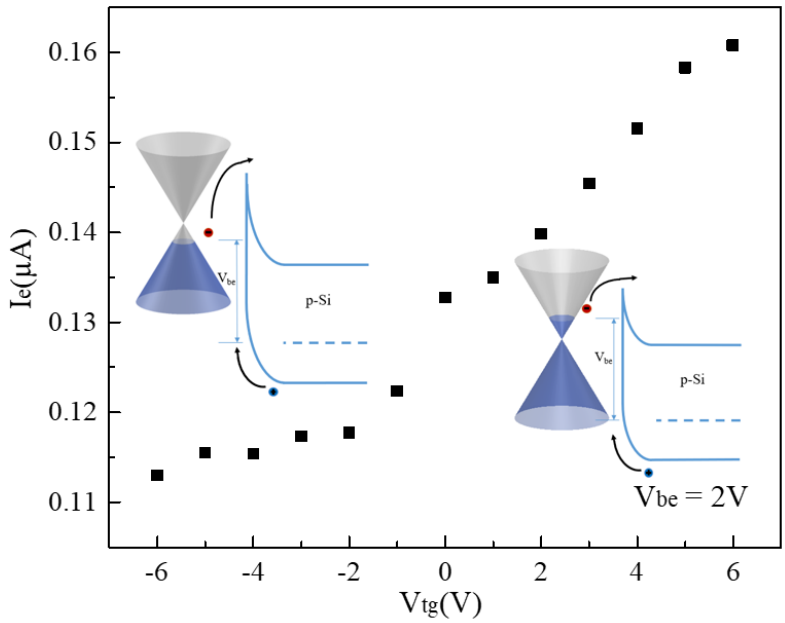

Figure 4.3 Graphene-Si junction current trend with V_{tg} at a constant junction bias V_{be} with corresponding band diagram shown inset.

4.4 Graphene BJT Gain

One of the most important and widely used applications of BJT is current amplification. The common emitter amplification curves of one representative graphene BJT are presented in the left panel of Figure 4.4. For these measurements, the emitter is grounded, the silicon base is connected to a constant current source, and the collector-emitter bias (V_{ce}) is scanned from 0 V to 10 V, with the emitter top gate left floating. Since silicon can absorb visible light, all the measurements are conducted in a dark environment to avoid photocurrents.

The operation mechanism of a graphene BJT highly resembles its traditional counterpart – electrons from the graphene emitter overcome the Schottky barrier Φ_{Bn} into the Si base with a positive base-emitter bias, then diffuse in the base while recombining with holes, before finally being swept to the collector under the strong built-in electric field due to large reverse base-collector bias.

Since graphene BJT is measured with a constant base current, the voltage of the base is 1 ~ 3 V higher than that of the emitter according to base current values. For both zero and small collector-emitter bias cases, with corresponding band diagrams shown in Figure 4.5, injected electrons overcoming the barrier will only recombine with holes in the relatively long base region. Consequently, no current amplification is observed at these voltages due to the lack of electrical field to extract electrons into collector. On the other hand, at zero collector-emitter bias, holes transport from the silicon base into the graphene emitter and collector, mainly divided by their resistance values. While at small bias, the band becomes flat between the silicon base and the graphene collector, so nearly all the holes will come into the emitter, leading to a current plateau in Figure 4.4 with nearly the same values with base current.

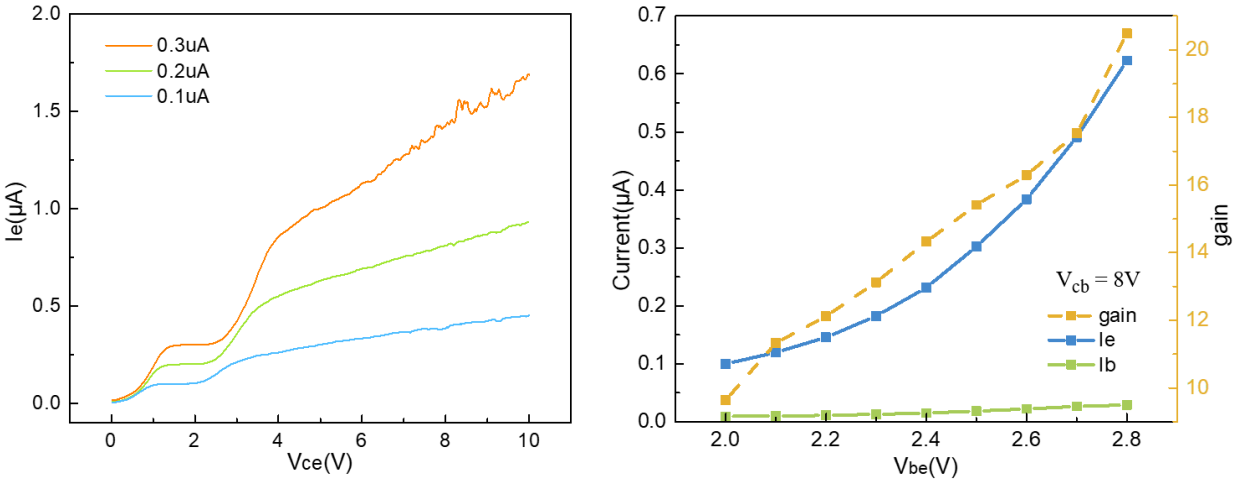

Figure 4.4 Amplification curves of graphene BJT device with constant base current (left) and Gummel plot and extracted gain ($\beta = I_c/I_b$) of graphene BJT device with collector-base bias set to 8V (right).

At a large collector voltage, electrons injected from the emitter begin to be efficiently extracted to the collector, which leads to the current amplification. Due to the existence of the injection barrier Φ_{Bn} and the relatively long base width, the graphene BJT current gain defined as $\beta = I_c/I_b$ reaches only around 5 for the common emitter amplification mode, which is far

smaller compared to traditional silicon BJTs with current gains of a few hundred. The Early effect, which originates from base width modulation, is significant at large bias with Early voltage V_A extracted from 2 V to 5 V. This huge Early effect suggests that a reduction in base width is a promising way to further enhance the current gain substantially.

In order to push the graphene BJT device to its best performance, a Gummel measurement has been carried out on the same device. With a constant collector-base bias (V_{cb}) as well as a relatively large base-emitter bias (V_{be}), the gain can be further pushed over 20 with V_{be} set to 2.8 V and V_{cb} set to 8 V, as shown in the right panel of Figure 4.4. Even though this gain value achieved from the Gummel plot is still less impressive than the traditional silicon BJTs with gain values typically higher than 100, this value is comparable to the current gain achieved with decent graphene FETs. The fact that gain increases with increasing V_{be} implies that a non-ideal space-charge region (SCR) current may also play an important role in graphene BJT operation[12].

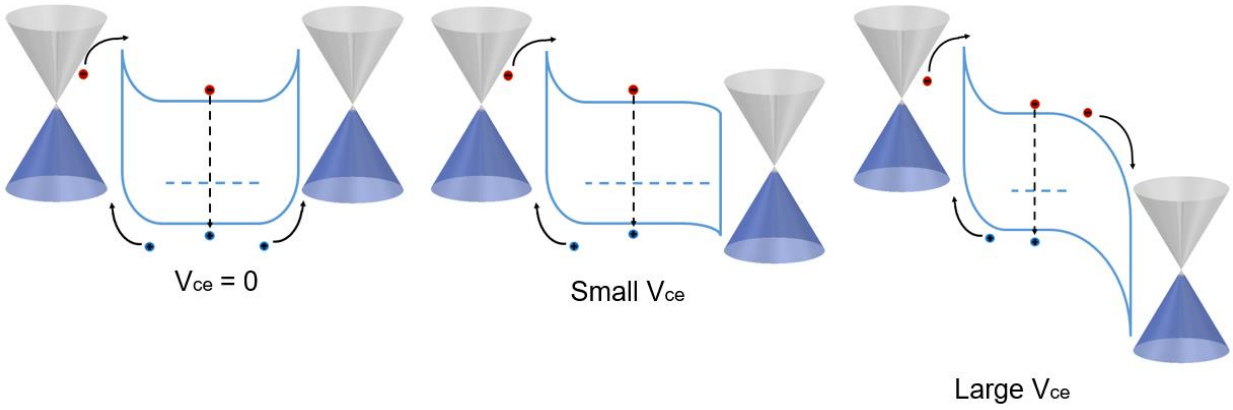

Figure 4.5 Corresponding band diagram for graphene BJT with zero (left), small (central) and large (right) collector-emitter bias V_{ce}.

One reason for the superior gain achieved in the Gummel plot compared with the common emitter configuration is the higher base-emitter bias V_{be} in the former case. For the common emitter configuration with a fixed collector-emitter bias, base-emitter bias V_{be} may be

limited to a smaller value by the ratio of two junction resistances following the voltage division rule. With the increase in base-emitter bias V_{be}, injected electrons from graphene will gain higher carrier velocity under higher electrical field so that they are less likely to recombine within unit length in the space charge region. Furthermore, instead of remaining constant as described in the ideal scenario, the Schottky barrier height at the emitter-base interface may also be subject to reduction under higher voltage, leading to an easier electron injection and increased current. Image-force lowering, for example, can be a key factor causing effective electron injection barrier lowering, which is proportional to the square root of the maximum electrical field[54].

The larger bias in the Gummel plot, with the two junction bias voltages adding up to 10.8 V, can also lead to a stronger modulation in base width. The gain of the graphene BJT device is sensitive to base width as indicated by the significant Early effect, therefore only a small decrease in base width may contribute to a considerate improvement in current gain.

4.5 Gain Tunability

Due to the merit of graphene Fermi level tunability, the electron injection barrier height Φ_{Bn} can be readily reduced by a top gate, leading to a further increase in the current gain of the graphene BJT device. As demonstrated by the amplification curves of another graphene BJT device of the same batch, presented in Figure 4.6 with the corresponding gain in the inset figure, the current gain increases steadily when the top gate voltage V_{tg} is scanned from -9 V to 9 V with the common emitter configuration. At a large negative gate voltage, the current gain vanishes and the graphene BJT is in non-amplification mode, while the gain increases steadily along with the gate voltage. The mechanism for current gain increase under positive V_{tg} is similar to that of a graphene emitter/p-type silicon junction. As the graphene Fermi level is tuned higher by a positive gate voltage, the electron injection barrier Φ_{Bn} is therefore reduced, resulting in an

enhanced injection efficiency and consequently a higher current gain. In a similar way, a negative gate voltage increases the barrier Φ_{Bn} instead and results in a suppressed gain due to a lowered graphene Fermi level, as explained in the band diagrams shown in Figure 4.7.

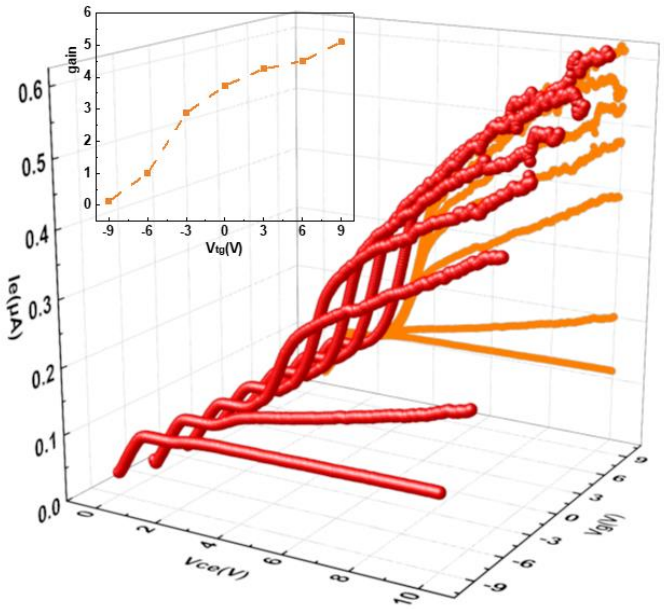

Figure 4.6 Graphene BJT common emitter amplification under different top gate voltages and the corresponding current gain tunability (inset).

As mentioned above, the DOS of graphene is at its minimum at the Dirac point. Combined with the fact that the change in carrier density of graphene is linear with the top gate voltage change ΔV_{tg}, the effectiveness of Fermi level tuning with the top gate voltage $\Delta E_F/\Delta V_{tg}$ is then maximized at the Dirac point. As a result, the change in barrier height Φ_{Bn} and thus gain tunability is most efficient near the Dirac point, if non-idealities such as Fermi level pinning and image-force lowering are not taken into consideration. However, in order to achieve a higher current gain, a smaller Φ_{Bn} and consequently a heavily n-type doped graphene is preferred for the emitter, causing a trade-off between higher gain values and efficiency of the gain tunability for graphene BJT devices.

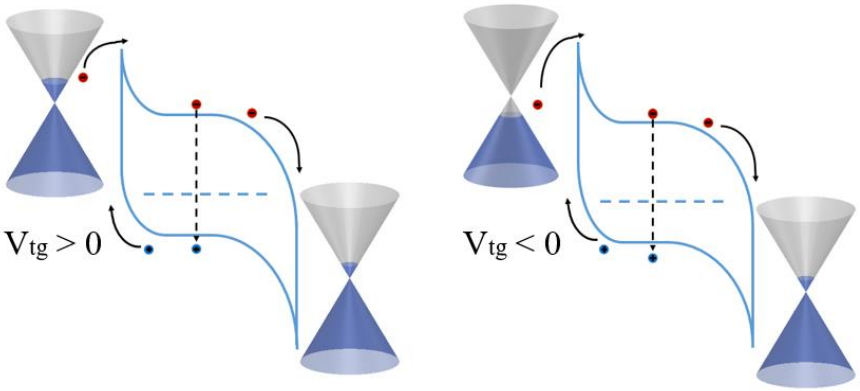

Figure 4.7 Corresponding band diagram of graphene BJT under positive gate bias (left) and negative gate bias (right).

4.6 Conclusion

In conclusion, we demonstrate an electrically tunable lateral structured graphene-Si-graphene BJT with its direct current gain pushed over 20. By utilizing graphene Fermi level tunability, the graphene BJT device can be smoothly and readily tuned from non-amplification mode to current amplification mode with the graphene emitter controlled simply by a top gate electrode. With decent performance, simplicity and extensibility, this novel graphene BJT device demonstrates a promising way forward for nanoscale BJT applications.

4.7 Supplementary Information

4.7.1 Base Width Modulation Simulation

The electric potential in a graphene BJT is inspected with COMSOL simulations, with graphene-silicon junctions approximated by ideal Schottky junctions, of which the work function is set at 4.3 eV in consideration of the graphene Fermi level gate tunability. For simplicity, the base contact is placed at the bottom of the silicon wafer, with a wafer dimension of 15 μm in width and 7 μm in height. the emitter and collector share the same width of 2 μm as determined by graphene-silicon overlap regions, with a 0.75 μm separation in between as the base width.

In the simulation, the base is set to 2 V with the emitter grounded, and the collector voltage is set at 5 V and 8 V in the top and bottom panel Figure 4.8, respectively. Clearly, a more significant base width modulation appears at the higher collector voltage, as indicated by the expansion in collector depletion region, which may explain the severe Early effect observed in the graphene BJT device.

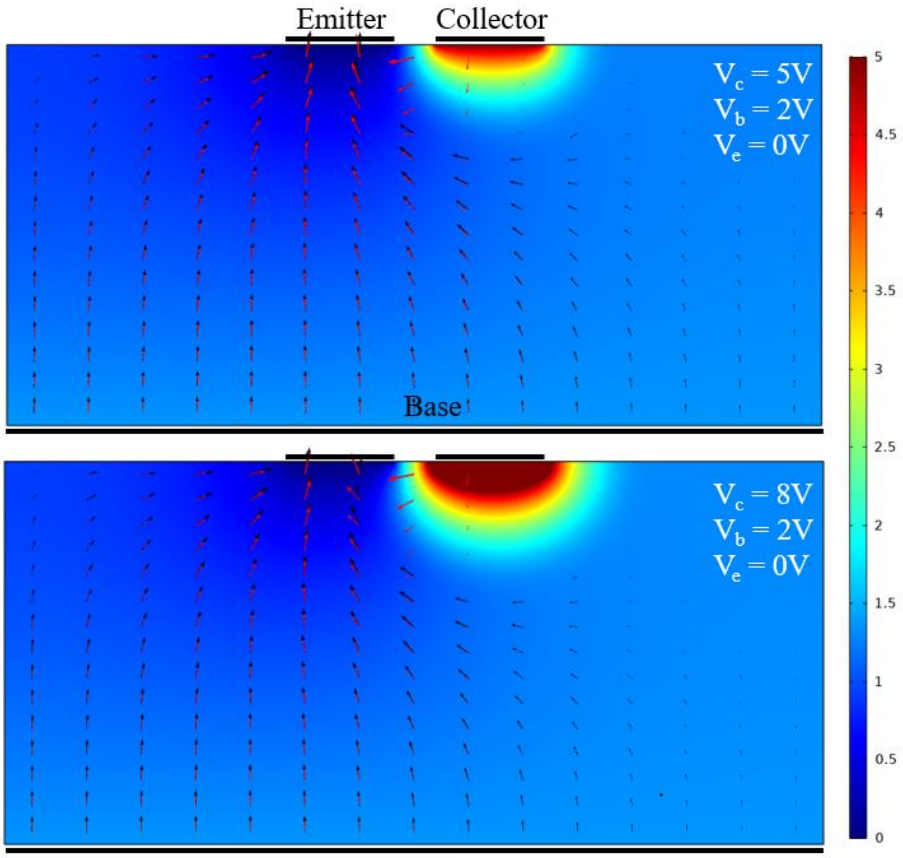

Figure 4.8 Electrical potential simulation results with collector voltage set at 5 V (top) and 8 V (bottom). Base voltage is set at 2 V in both cases with emitter grounded. The same rainbow color scale bar is used for a clear comparison. Red and black arrows stand for electron and hole current density respectively in logarithmic scale.

Electron and hole current density are also represented in the same figure with logarithmic scale, with red color for electron and black for holes. It is necessary to point out, however, that due to the limits in voltage values and sample dimension imposed by simulation convergence

requirements, the electrical field along the vertical direction is exaggerated by orders of magnitude, which leads to the overestimation of hole current density in this simulation.

4.7.2 Further Discussions on Gating Effect

With the parallel plate capacitor model , 9 V emitter top gate bias will induce an electron density $n = 1.55\times10^{13}$ cm^{-2}, where Al_2O_3 dielectric constant $\varepsilon_{Al_2O_3} = 7.8$ is used. In combination with the graphene tunability equation $\Delta E_F = \hbar v_F\sqrt{\pi n}$, this induced electron density corresponds to a 0.46 eV increase in pristine graphene Fermi level in ideal case. In real case, however, graphene can only screen the electric field partially – for example, with a screening efficiency of ~70% reported for the first layer in few-layer graphene system with doping concentration around 10^{13} cm^{-2}[127]. Unscreened electric field will consequently decrease hole concentration and/or induce electrons near the graphene-silicon junction interface, leading to a smaller electron-hole recombination rate and/or a higher electron density in base region – both effects will contribute to a higher current gain though the electron injection barrier in this case is slightly less lowered compared to fully screened case.

Chapter 5 μ-Column Graphene Chemical Sensor Review and Sensor Miniaturization

5.1 Introduction

Graphene, with its extraordinarily high surface-to-volume ratio, is an ideal platform for chemical sensor applications. A graphene heterodyne sensor[128,129], where dipole-induced charge density modulation with a driving voltage excitation is utilized, has been pioneered by Girish Kulkarni et al. in 2014, demonstrating a rapid and sensitive detection (down to 0.1 s and 1 ppb) for a large variety of volatile organic compounds. However as its response is strongly determined by analyte molecular dipole moment, the graphene heterodyne sensor shows little response to nonpolar molecules.

Borrowing the idea of a μ-column structure from the heterodyne sensor, new types of μ-column graphene devices have been developed by Dr. Wenzhe Zang for chemical vapor separation and sensing[130,131]. With a closer inspection on analyte molecular physisorption process, a fast, efficient, and electrically tunable vapor separation is achieved, leading to an ultra-compact gas chromatography system. Remarkably, by using the electrostatic effect with a direct current setup, a broad detection range has been demonstrated for both polar and nonpolar volatile compounds, with comparable sensitivity and rapidity with the heterodyne sensor. These background works lay the foundation for the following studies on the miniaturized direct current graphene sensors, and the proposed mechanisms are briefly reviewed (Section 5.2) for a better understanding.

To integrate with a hand-held gas chromatography system, the direct current graphene sensor is further redesigned and fabricated with a reduced size of 1 cm by 0.7 cm. This

miniaturized graphene sensor demonstrates a performance with comparable sensitivity and even faster response compared to its full-size counterpart, with comparisons on different flow channel designs accomplished as well. In the end, the performance in formaldehyde sensing is also inspected, with a small footprint chemical sensor decorated with metal oxide showing a decent responsivity.

5.2 Review of Proposed Mechanisms

5.2.1 Molecular Physisorption on Graphene

The physisorption dynamics between analyte molecules and a graphene sheet has been examined under different gate voltages[128-130]. The binding energy is a key factor to the desorption rate k_{des} of analyte vapor molecules on graphene's surface, which is governed by the Arrhenius equation

$$k_{des} = \nu_f \exp\left(-\frac{E_a}{kT}\right)$$

where $\nu_f \equiv \frac{kT}{h} e^{\frac{\Delta S}{R}}$ is known as the attempt frequency from the Eyring equation in transition state theory[132] with ΔS as the entropy of activation, and T, k, h and R as absolute temperature, the Boltzmann constant, Planck's constant and the gas constant respectively.

The desorption rate of each analyte can be readily extracted from the decay part of the corresponding current signal. Due to the bipolarity of graphene, an increase in gate voltage can induce either a higher electron density or a lower hole density, with the former leading to a stronger repulsion and the latter to a weaker attraction between graphene and the analyte molecules whose dipole moment is pointing upwards away from graphene sheet. The binding energy for this kind of analyte molecules, such as chloroform on a graphene surface, therefore, becomes smaller at an increased gate voltage, as demonstrated by the higher desorption rate

shown in the left panel of Figure 5.1. Similarly, for analyte molecules with dipole moments pointing downwards towards graphene, the binding energy tends to increase with gate voltage, resulting in suppressed desorption rates.

For non-polar molecules or those with dipole moments parallel to the graphene sheet such as 1,2-dichlorobenzene, their desorption rates k_{des}, however, show negligible dependency on the gate voltage compared to other polar molecules with perpendicular dipole moments.

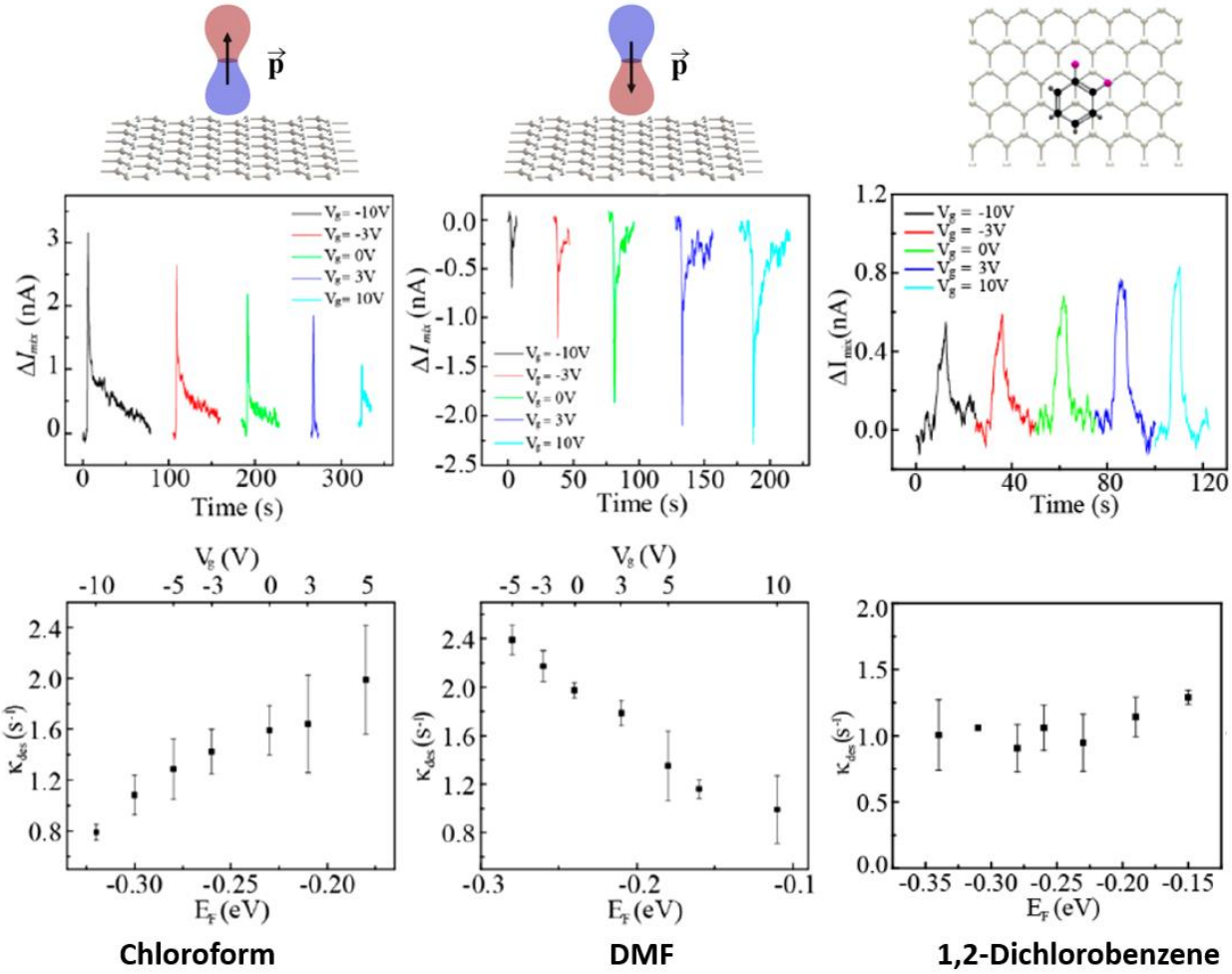

Figure 5.1 Gate tunability of physisorption dynamics for analyte molecules on graphene sheet with different dipole moment orientations as represented by chloroform, DMF and 1,2-dichlorobezene. [129,130]

With graphene FET gate voltage V_g varying from -10 V to 5 V, the graphene Fermi level position with respect to the Dirac point shifts from -320 meV to -180 meV accordingly, as

calculated from the density of states of graphene. The desorption rate of chloroform, as extracted from the response decay at each voltage, is reported to increase from 1.16 s^{-1} to 1.95 s^{-1}, with an attempt frequency $v_f \approx 1.2\times10^4$ Hz and corresponding activation energy E_a decreasing from 235.4 meV to 222.2 meV.

The same set of data is also extracted for DMF, which has the opposite molecular dipole orientation. In contrast to chloroform, a rising trend in the binding energy and a declining trend in desorption time with gate voltage are reported in this case, with a variation range of 9.5 meV and 1.26 s^{-1} respectively, which agrees well with the proposed analyte molecular dipole-graphene interaction model.

5.2.2 Electrostatic Effect Induced Capacitance Modulation

Direct current responses of the graphene sensor follow the basic graphene FET I-V characteristics[12,54], with extra terms originating from interactions between analyte molecules and graphene. Besides the molecular dipole-induced charge density modulation Q_m, capacitance modulation C_m induced by the electrostatic effect is also proposed as an essential contributor to the change in direct current. Supposing the charge neutrality point of graphene is at V_{np}, the direct current can be expressed as:

$$I_{ds} = \mu_{eff}\frac{W}{L}\left(\left(C_g + C_m\right)\left|V_{gs} - \frac{1}{2}V_{ds} - V_{np}\right| + Q_m\right)V_{ds}$$

Due to the semi-metallic and atomically-thin nature of graphene, the electric field penetrating through the gate dielectric cannot be fully screened by the graphene sheet. The unscreened part of the electric field will then interact with the injected analyte molecules in close proximity to graphene, leading to the vapor-induced capacitance modulation. Since the dielectric constants of analytes are typically higher than that of helium carrier gas ($\varepsilon_r \approx 1$ for helium gas[133]), the

change in direct current is always positive due to the increase in capacitance as modulated by analyte vapors.

The reported impedance measurement demonstrates that, as shown in Figure 5.2, the alternating current i_{ac} increases with the injected mass of acetone at a constant AC voltage v_{ac}. The rather linear change in admittance with injected mass is ascribed to the capacitance modulation due to analyte vapor, with the total change proportional to the injected mass.

The consistency in the sign of direct current responses is also reported, regardless of graphene electron or hole branch, for chloroform, acetone, n-nonane and nitrobenzene, which further excludes charge transfer from being the dominant contribution. Since the charge transfer mechanism relies highly on relative electronegativity between graphene and analyte molecules, each analyte will only contribute either electrons, or alternatively holes to graphene, leading to a positive current response for one graphene branch and a negative response for the other. The fact, however, is that the current responses all remain positive for the four analytes with headspace vapor injection, indicating the increase of carriers in both cases.

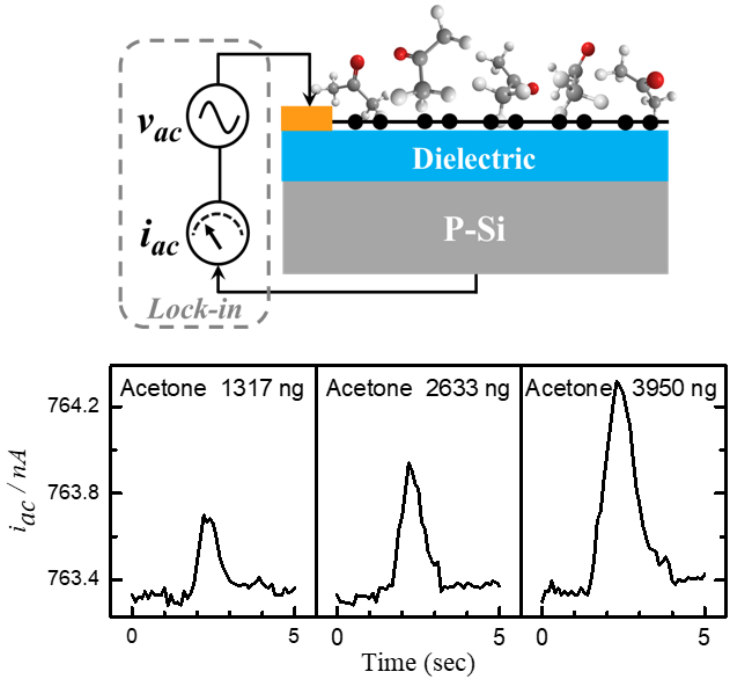

Figure 5.2 Impedance/admittance change due to analyte injection. [131]

5.3 Graphene Chemical Sensor Miniaturization

In the previous subsection, the mechanisms proposed in the outstanding works on graphene chemical sensors for vapor sensing and separation, which were pioneered by our former group members, have been briefly reviewed. As sensors, the graphene devices demonstrate superior performances such as broad detection range, rapid (sub-second level) and sensitive (ppb level) detection as well as great stability over time. The DC graphene sensor device, however, has a relatively large size of 2 ~ 3 cm in both length and width, which limits its use for the integration with a hand-held gas chromatography system as proposed by our collaborators. In view of this, a small footprint graphene chemical sensor with similar device structure has been redesigned and fabricated, with length and width of 1 cm and 0.7 cm respectively. Multiple gas flow channel designs are also proposed at the same time for optimization of the sensor response. The small footprint graphene chemical sensor demonstrates

a comparable sensitivity with its large footprint counterpart, and an even faster response with halved or even quartered peak width.

5.3.1 Device Structure and Fabrication

The whole device is assembled by bonding an etched insulating cap with gas flow µ-column onto a pristine graphene FET (Figure 5.3). 300 nm-thick dry oxide is first grown on bare cleaned silicon wafer, followed by the growth of 80 nm-thick Al_2O_3 with ALD to form a high-quality insulating layer. CVD grown graphene on copper is first spin-coated with polymethyl methacrylate (PMMA) and then followed by an overnight Cu-etching process using ammonium persulfate ($(NH_4)_2S_2O_8$) solution with a concentration of 25 mg/mL. Subsequently, graphene is transferred onto a prepared $Al_2O_3/SiO_2/Si$ substrate by a PMMA-assisted wet transfer process. After removing PMMA by soaking in acetone for several hours, contacts for graphene (Cr/Au 5 nm/50 nm) are deposited using photolithography and e-beam evaporation. Graphene is then patterned into 0.5 cm by 0.5 cm squares by an oxygen plasma etch. After the fabrication of the graphene transistor, the substrate is diced into 1 cm by 0.7 cm pieces waiting for the bonding with the gas flow cap. The cap is fabricated on a silicon wafer with 2 µm-thick SiO_2, with the 400 µm-deep gas flow channel etched into it by deep RIE. This wafer is also diced into 0.6 cm by 0.7 cm cap pieces for bonding. Before bonding, the graphene FET and µ-column gas flow cap are cleaned respectively by acetone/PRS-2000/2-propanol and Piranha cleaning to minimize the organic residues. The µ-column gas flow cap is subsequently bonded to the graphene FET to form the gas flow channel over graphene, with two guard columns also bonded to the device as the interfaces for the gas chromatography (GC) connection. Guard columns made of deactivated fused silica from Restek® with 380 µm/250 µm outside diameter (OD)/internal diameter (ID) are used to minimize the analyte retention inside the column.

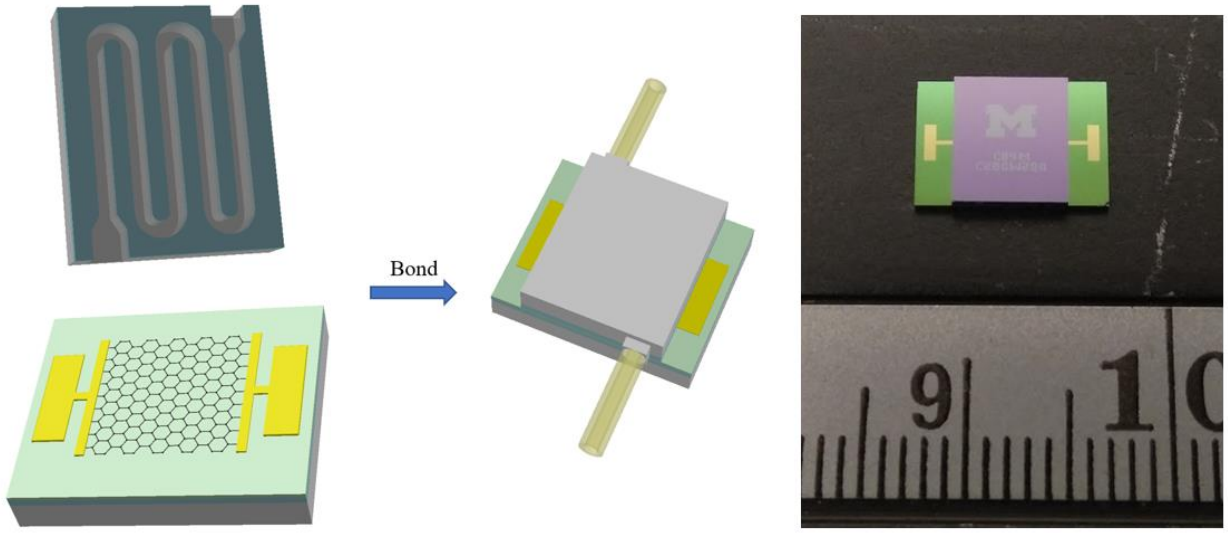

Figure 5.3 Schematic (left) and photo (right) of graphene chemical sensor. Guard column is not shown in the photo.

5.3.2 Device Performance and Gas Flow Channel Design Comparison

To optimize the electrical responses of the graphene chemical sensor, different designs of the gas flow channel are fabricated and bonded with graphene FETs from the same batch for comparison. In the C01M and C03M channel designs, both flow channel widths are set at 400 μm, but with the total flow channel length set at 2.08 cm for C01M and 2.81 cm for C03M, respectively. The coverage of the C01M flow channel over the graphene sheet is calculated as 33.2%, also lower than the 45.0% coverage of C03M design. The top view of both gas flow channel designs is shown in Figure 5.4, with the blue color representing the flow channel, the green square the graphene sheet, and the red area the graphene FET contacts.

Devices 34 and 35 are subsequently fabricated with C01M and C03M designed gas flow caps respectively, with a common flow channel height of 400 μm. Devices 38 and 39, on the other hand, share the same flow channel design with device 34 and 35 respectively, but with a reduced flow channel height of 200 μm.

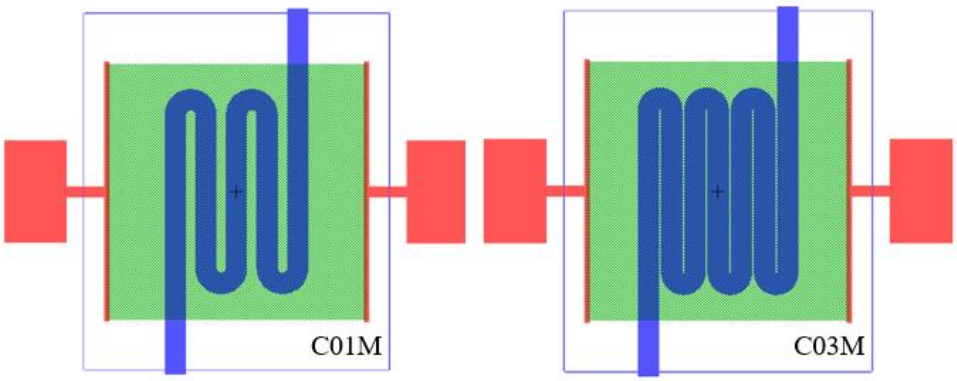

Figure 5.4 Graphene chemical sensor with high coverage of 45.0% (C01M) and low coverage of 33.2% (C03M) flow channel designs.

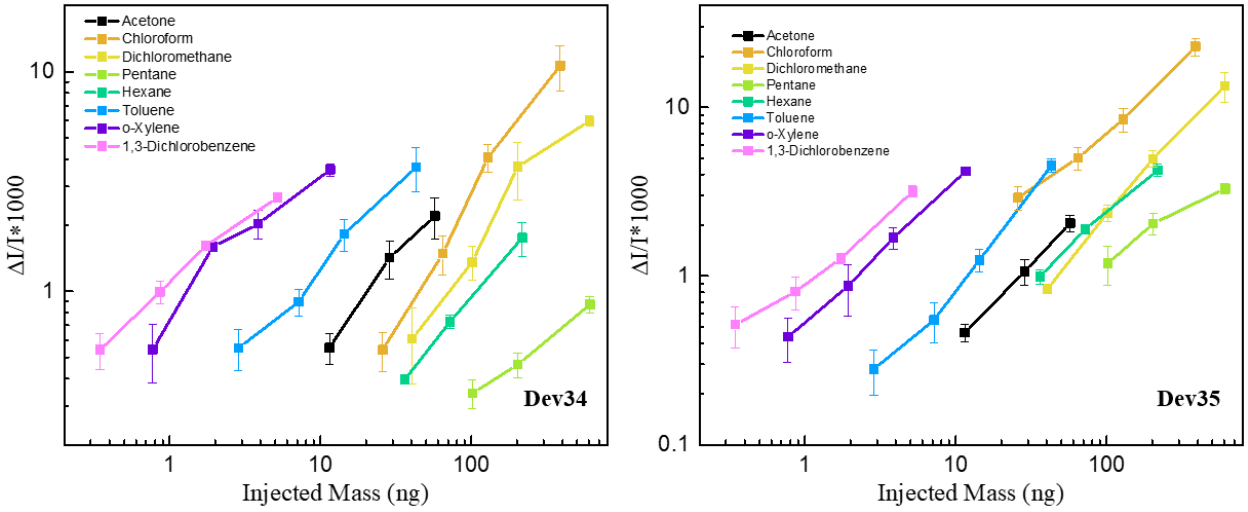

Figure 5.5 Dynamic range of two graphene chemical sensors (Dev34 and Dev35) with corresponding gas flow channel designs shown in Figure 5.4.

The dynamic ranges of devices 34 and 35 are shown in Figure 5.5, with eight chemicals measured for the comparison including ketones, organic chlorides, alkanes and aromatics. While the two devices share a similar response pattern, device 35 which has a larger flow channel coverage over graphene sheet, generally shows a higher sensitivity for most of the analytes, especially for alkanes (pentane and hexane) and non-aromatic organic chlorides (chloroform and dichloromethane).

The sublinearity, though still present for chemicals such as pentane, is suppressed in these miniaturized graphene chemical sensors as indicated by the slope in their dynamic range log-log plots, as well as the approximately linear behavior in the device dosage response plots presented in Figure 5.6. The slope in dynamic range plot is extracted from ~0.52 for pentane to ~1.10 for chloroform with device 34, while for device 35 the variation is ~0.57 for pentane to ~0.76 for chloroform. The slope value around 1.10 for chloroform with device 34 may be subject to data fluctuations caused by manual injection and/or underestimation of signal at small doses due to the influence of noise.

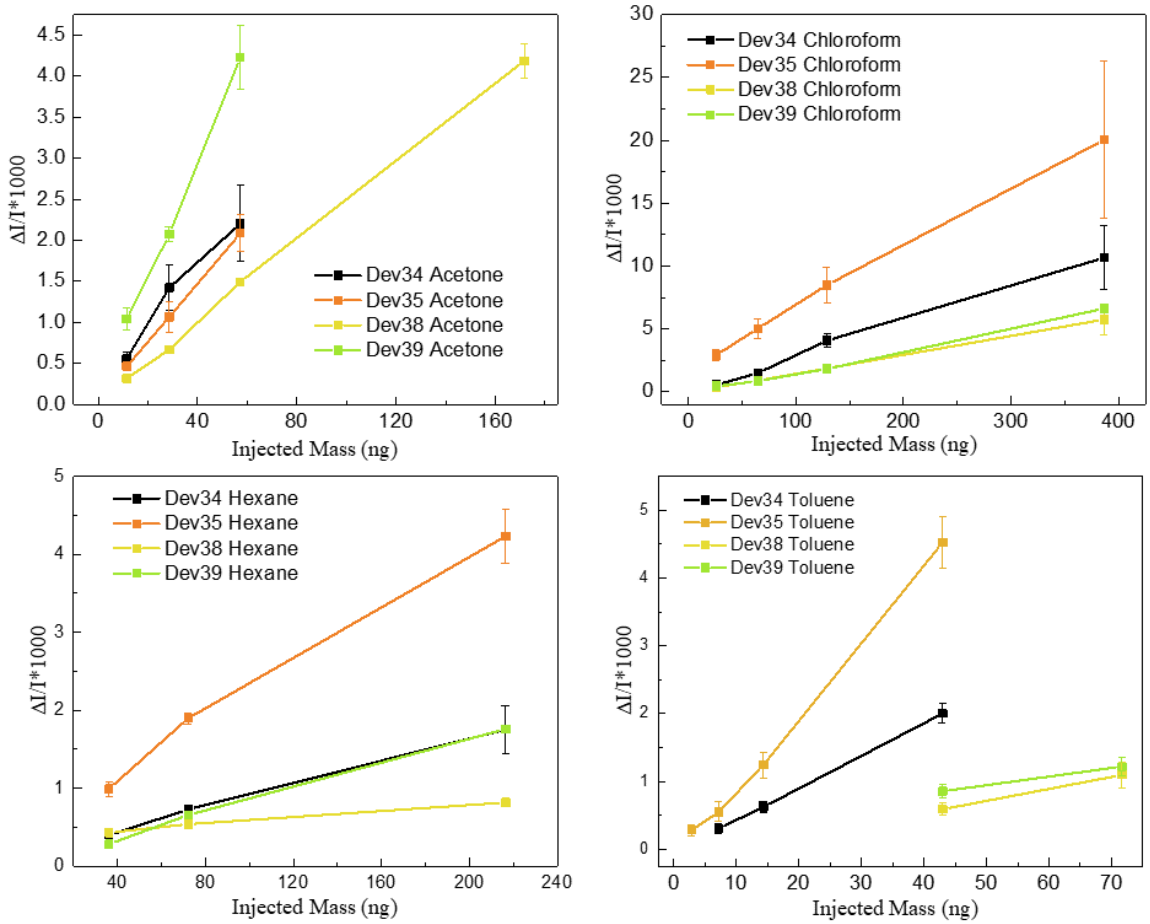

Figure 5.6 Dosage response plots of acetone, chloroform, hexane and toluene. Device 34, 35 and device 38, 39 are paired for flow channel coverage comparison, while device 34, 38 and device 35, 39 for flow channel heights comparison.

Dosage response plots of four analytes (acetone, chloroform, hexane and toluene) are measured with device 34, 35, 38 and 39 and presented in Figure 5.6, with each analyte representing the corresponding ketone, organic chloride, alkane or aromatic group. For the three chemicals other than acetone, it is evident that responses from sensors with a larger area coverage over graphene sheet such as devices 35 and 39, are higher compared to responses from corresponding less-covered sensors such as devices 34 and 38. In addition, a comparison in channel height concludes that, as shown by dosage responses of device 34, 38 and device 35, 39 pairs, a higher channel height typically leads to higher graphene sensor responses.

The response of acetone, however, is the exception from the empirical rules observed from the data of chloroform, hexane and toluene. This abnormal behavior of acetone may be explained by the contributions from both capacitance modulation above graphene and analyte molecular dipole-induced charge density modulation, which may have opposite signs[128-131]. A particular ratio of contributions from the two modulations may be the reason for the complicated and exceptional behavior of acetone, with more future studies needed such as the dynamics of molecules on graphene.

Typical sensing performance of a small footprint graphene sensor is listed in Table 5.1, with comparison with its larger footprint counterpart with 2 cm by 2 cm graphene size. Response speed of the small footprint sensor, as characterized by the full-width-half-maximum (FWHM), is two to four times faster for all the four chemicals measured, which is reasonable due to the reduced gas flow channel length. The small footprint graphene sensor's limit of detection (LOD), as defined by the injected mass that induces a current change of 3σ noise floor, is comparable to its counterpart. With one order of magnitude higher in sensitivity in acetone and toluene detection, the miniatured sensor, however, is less sensitive for dichloromethane and pentane.

Analyte	Limit of Detection (ng)		Full-Width-Half-Maximum (s)	
	Small Footprint	Large Footprint	Small Footprint	Large Footprint
Acetone	4	45.5	0.5	1.46
Dichloromethane	110	79.7	1.4	2.7
Toluene	3.5	39.3	0.5	1.9
Pentane	290	128.5	0.5	1.7

Table 5.1 Performance comparison between small and large footprint μcolumn graphene chemical sensors.

5.3.3 Formaldehyde Sensing

Formaldehyde is a health-detrimental volatile organic compound that is widely present in furniture and construction materials. Exposure to formaldehyde gas is a high-risk factor causing abnormalities in blood-forming systems[134-136], which makes sensing formaldehyde a necessity. Metal oxide nanoparticle sensors made of tin oxide, zinc oxide etc. are a sensitive and less expensive way to sense formaldehyde and thus having been widely studied[137-142]. However, sensing of formaldehyde with metal oxide nanoparticles requires a high operation temperature, typically ranging from 200 ºC to 400 ºC, to oxidize the formaldehyde[137-142], which causes extra power dissipation and limits the application of metal oxide sensors when room temperature operation is required.

Borrowing the idea from metal oxide nanoparticle sensors, a small footprint graphene sensor functionalized by tin oxide is fabricated here for the detection of formaldehyde. 2 nm tin is first evaporated on a graphene sheet and consequently is oxidized in air for several days, before the bonding process of the graphene FET and gas flow channel. The gas flow channel is 200 μm in both width and depth, with a total length of 5.27 cm and a corresponding flow channel coverage of 42.1% over graphene sheet.

Graphene FET transfer curves before tin deposition, right after 2 nm deposition of tin and 42 hours after deposition are shown in Figure 5.7 for comparison. It can be clearly observed that before deposition, graphene is highly p-type doped, possibly due to the doping of water vapor in air[143], with the gate voltage corresponding to its Dirac point beyond 80 V. Right after tin deposition, due to the scattering and surface impurity states, large hysteresis and a significant drop in graphene mobility occur. The gate voltage corresponding to the Dirac point also shifts greatly, possibly due to the doping from tin, whose work function is around 4.42 eV[144]. With a 42-hour-long oxidation in air, which should be sufficient for full oxidation of 2 nm tin, graphene is less p-type doped in comparison with the case before tin deposition, with the gate voltage for the Dirac point shifts between 20 to 50 V. The mobility of graphene, though recovered partially, only reaches about half of that before tin deposition.

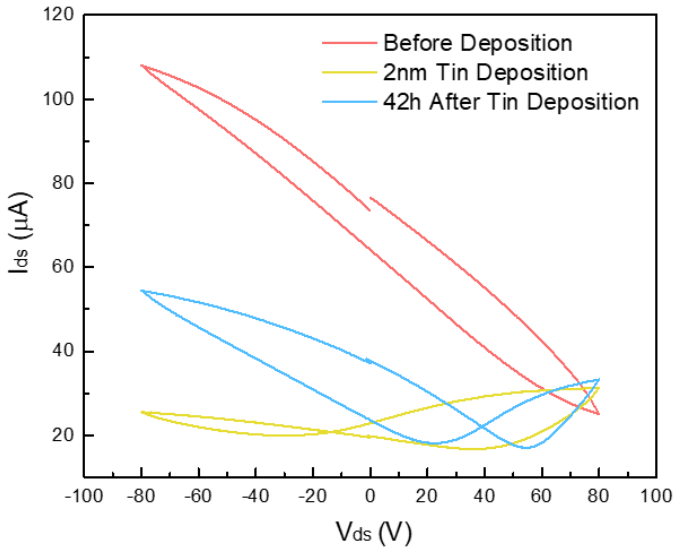

Figure 5.7 Transfer curve of graphene FET before deposition (red), right after 2 nm tin deposition (yellow) and 42 hours after deposition for thorough oxidation (blue).

This tin oxide-decorated graphene chemical sensor exhibits a good performance in formaldehyde gas sensing, with a distinct contrast to a pristine graphene sensor, as shown in Figure 5.8. Due to the difficulty in obtaining pure and stable formaldehyde samples, a

formaldehyde water solution stored in ampoules is used in the measurement. 50 µL and 100 µL of vapor from a headspace vial containing a formaldehyde water solution (Sigma-Aldrich QC1380-20ML lot number LRAC1730, with formaldehyde concentration of 55.3 ± 0.4 mg/L and a standard deviation of 5.53 mg/L) are injected with a GC injector into the tin oxide-decorated graphene sensor. The same amounts of headspace gas from a pure water vial are also injected in the same way as a control group. It is clearly seen that formaldehyde vapor samples result in a 50% larger electrical response compared to the control group for both 50 µL and 100 µL vapor injections, in sharp contrast with the pristine graphene sensor where no obvious difference has been observed between the injection of formaldehyde and water head space gases.

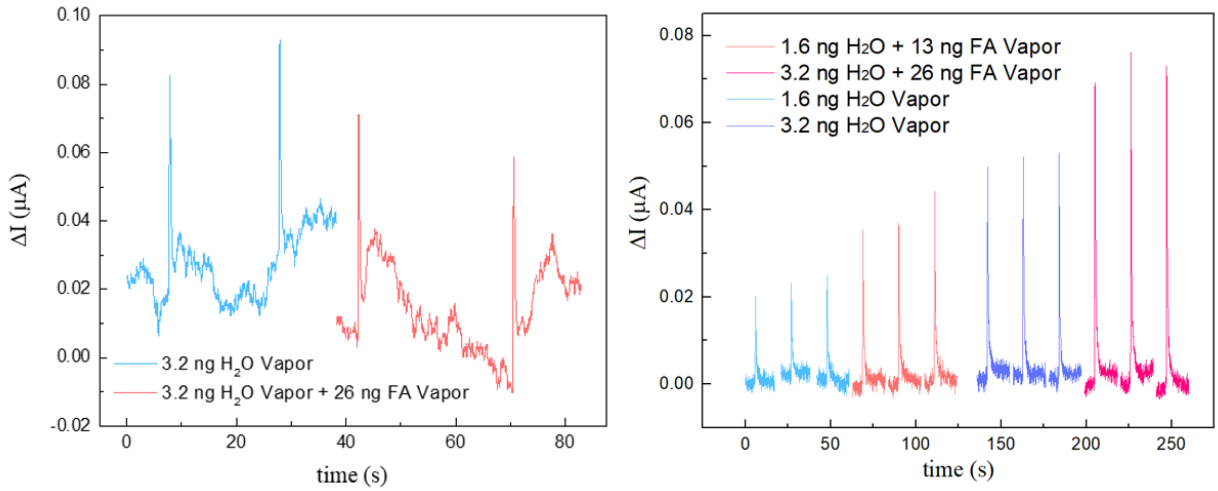

Figure 5.8 Pristine graphene small footprint chemical sensor (left) and 2 nm tin oxide decorated graphene sensor (right) for formaldehyde vapor sensing.

5.4 Conclusion

In conclusion, the proposed mechanisms in pioneering background works have been first briefly summarized, which were the analyte molecular dipole-induced charge density modulation and electrostatic effect-induced capacitance modulation. To integrate with a hand-held gas chromatography system, a direct current graphene sensor is redesigned and fabricated with a miniature size of 1 cm by 0.7 cm. The miniaturized graphene sensor has comparable sensitivity

and even faster responses with only half or a third of peak width compared to its full-size counterpart. Comparisons on different flow channel designs indicate that larger channel coverage on graphene and larger flow channel height typically lead to higher sensor responses. In the end, a tin oxide-decorated graphene chemical sensor is fabricated and tested for formaldehyde vapor sensing. While a pristine graphene sensor shows no difference between the headspace vapor of a formaldehyde water solution and that of pure water, the tin oxide-decorated graphene sensor exhibits 50% higher responses for formaldehyde vapor samples compared to the pure water control group, indicating its capability for formaldehyde sensing.

Chapter 6 Label-free Single Graphene Sensor for Chemical Vapor Discrimination

6.1 Introduction

Volatile compounds, such as low molecular weight organic chlorides, alkanes, aromatics and ketones, exist widely in daily life in the gas phase. Many of these vapors can be severely detrimental to human health , yet they are ubiquitous. Benzene, as an example, has been classified as a human carcinogen (group 1) and exposure to it can cause serious or even fatal blood-forming dysfunction related diseases[145-147]. Exposure to benzene, however, can happen easily even through daily activities like smoking, automobile services or inhalation of vehicle exhaust, as well as in laboratories or factories where benzene is commonly used as an intermediate for chemical preparation[147,148]. As a result, sensing and discrimination of volatile compounds are essential for routine gas concentration monitoring as well as leakage detection.

Nanomaterials, including zero-dimensional nanoparticles such as metal oxide nanoparticles[137,138,140-142,149-152], one-dimensional nanowires such as carbon nanotubes[153,154] and two-dimensional nanosheets such as decorated or pristine graphene[128,129,131,155] as well as 2D metal-organic frameworks[156], are promising candidates for vapor sensing and discrimination applications due to their unique physical and chemical properties at lower dimensions. Since both physisorption and chemisorption of analytes happen only at the surface of the sensing material, a high surface-area-to-volume ratio is therefore crucial for decent responses. Compared to their three-dimensional counterparts, nanomaterials possess significantly higher surface-area-to-volume ratios, which lays the

foundation for their prosperity. In addition, high quality nanomaterials such as carbon allotropes and TMDCs also possess the potential for integration with the modern CMOS process line for mass production in the future, with pioneering studies on BEOL compatible devices reported by leading entities in the semiconductor industry such as TSMC and IMEC[76,157].

Based on these merits, a large variety of nanomaterial-based electronic noses (e-nose) with high reliability and portability have been proposed for vapor discrimination, consisting typically of chemiresistive sensor arrays for data acquisition with matching algorithms for data analysis[158,159]. These chemiresistive arrays, however, generally suffer from slow responses due to the charge transfer process from tens of seconds to minutes, which severely limits their use for time-sensitive applications such as real-time chemical monitoring. Moreover, the complicated fabrication processes such as functioning group decoration or complex structured materials synthesis, as well as the lack in cost-effectiveness originating from device duplication for array assembly, all suggest a faint possibility for future mass production of chemiresistive arrays. Even though a decent single unmodified graphene chemiresistive sensor has also been reported for volatile vapor discrimination[160], which avoids the tricky issues caused by decoration or array assembly, it is intrinsically slow.

In light of the difficulty faced by chemiresistive arrays, here we propose a true label-free single graphene sensor for rapid detection and effective discrimination of volatile compound vapors, with the schematic shown in Figure 6.1. Based on a pristine graphene FET bonded with a μ-column gas flow channel cap, this graphene device generates electrically tunable responses, by utilizing the gate tunable, fast analyte vapor induced modulations in graphene[128-131], with rapid responses down to the sub-second level, which is orders of magnitude superior to typical chemiresistive arrays for e-nose applications.

Accurate vapor discrimination has also been demonstrated by this true label-free fast graphene sensor device with algorithms such as principal component analysis (PCA)[161,162]. In contrast to conventional electronic sensors or sensor arrays, surface functionalization on the sensor is no longer needed in order to achieve chemical discrimination. By utilizing the difference in analyte electrical response trends with gate voltages, or gate spectra, along with the response intensity of analytes, 11 analyte vapors are clearly grouped into separate regions in the PCA plot, with each representing a corresponding chemical category. The identification accuracy, as verified by multiple algorithms, is rather satisfactory with at least 98.8% accuracy into the 11 specific chemicals and at least 93.9% accuracy into the four corresponding categories, demonstrating the excellent performance of our graphene device.

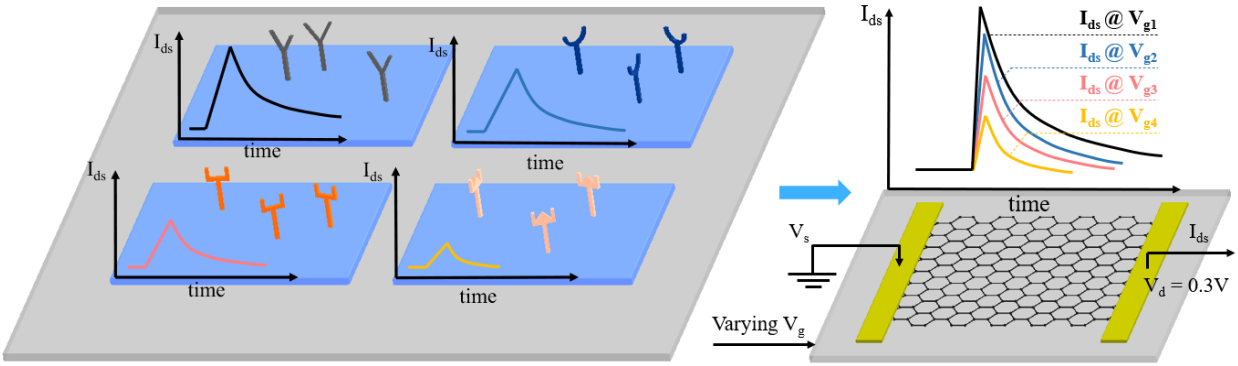

Figure 6.1 The schematic of chemiresistive array (left) and graphene chemical sensor (right) for volatile compounds discrimination.

6.2 Measurement Setup

The small footprint graphene chemical sensor for volatile compounds sensing and discrimination is fabricated using the same method as described in the previous chapter. The gas flow channel dimension of the device is 400 μm in height and 200 μm in width, with a total length of 3.52 cm and a coverage of 28.2% over the graphene sheet. The graphene dimension is

still chosen as 0.5 cm by 0.5 cm, with 5 nm Cr/50 nm Au evaporated as graphene contacts and 80 nm Al_2O_3/285 nm dry-grown SiO_2 as the back gate dielectric.

The inlet guard column of the graphene chemical sensor is connected to a GC injector for manual analyte injection. The temperature of the injector is set to 200 °C to ensure thorough evaporation of analytes, and the pressure is set to 2.0 psi, with a corresponding gas flow rate of 4.5 mL/min. Pure liquid analyte, instead of headspace gas, is chosen for the sensing and discrimination experiment to avoid impurities from the air for more accurate and reliable data. 0.05 μL of the liquid analyte is injected for each measurement manually by a microsyringe into the GC injector, and it is vaporized immediately inside the injector before flowing into the graphene sensor via the guard column. The source/drain bias (V_{ds}) of the graphene sensor is set at a constant value of 0.3 V, with the source grounded. Gate voltages (V_g) are chosen at 7 different values from - 45 V to 45 V, with an interval of 15 V. The schematic of the small footprint graphene device as well as the integration with GC is shown in Figure 6.2.

Considering the key position of functioning groups in analyte molecules, 11 representative chemicals (chloroform, dichloromethane, toluene, o-xylene, p-xylene, benzene, hexane, heptane, nonane, acetone and ethyl acetate) are chosen from four corresponding chemical categories (organic chlorides, alkanes, aromatics and ketones/ethers) to test the performance of the graphene sensor in vapor sensing and discrimination. Each individual analyte is injected 15 times at each of the 7 chosen gate voltages to ensure reliability and sufficiency of data for subsequent analysis.

The background current during the measurement changes relatively slowly with time, with a maximum slope only around 2×10^{-3} μA/s, while the analyte temporal response is very fast and significant, with a typical peak width of 0.1 ~ 1 s and a typical current change of 0.01 ~

0.1 μA. The change in background current, as a result, will induce only modest corrections to the sensor responses and create little difference in the analysis of data.

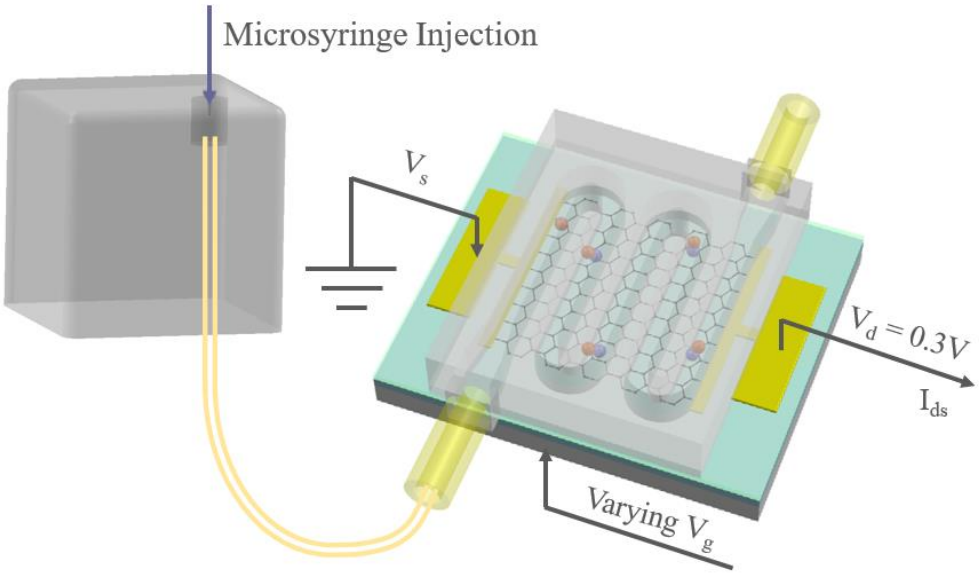

Figure 6.2 Schematic of graphene chemical sensor as well as the integration with GC for chemical sensing and discrimination.

6.3 Experiment Results and Analysis

Sharp temporal responses of chloroform under seven preset gate voltages have been plotted in Figure 6.3, with the background current flattened for a clearer view. The peak width $t_{1/2}$ of chloroform as defined by the FWHM, can reach amazingly as small as 0.11 s, which is an orders of magnitude improvement compared to charge transfer process-limited chemiresistive sensors. This fast sensing performance can be ascribed to the fast nature of analyte molecular dipole-induced charge density modulation and/or capacitance modulation due to the electrostatic effect, as proposed in the pioneering graphene sensor work[128-131]. A maximum current change (ΔI) is used to quantize the response, which is defined as the maximum change in current after each injection of the analyte. Instead of using responses from multiple sensors as in the case of e-nose, only a single graphene chemical sensor is required for chemical discrimination, with

multiple responses at different gate voltages from -45 V, -30V … to 45 V. Due to graphene's Fermi level tunability with gate voltages, the interactions between the analyte molecules and the graphene sheet are consequently modulated, leading to the response dependence on gate voltage which varies from chemical to chemical.

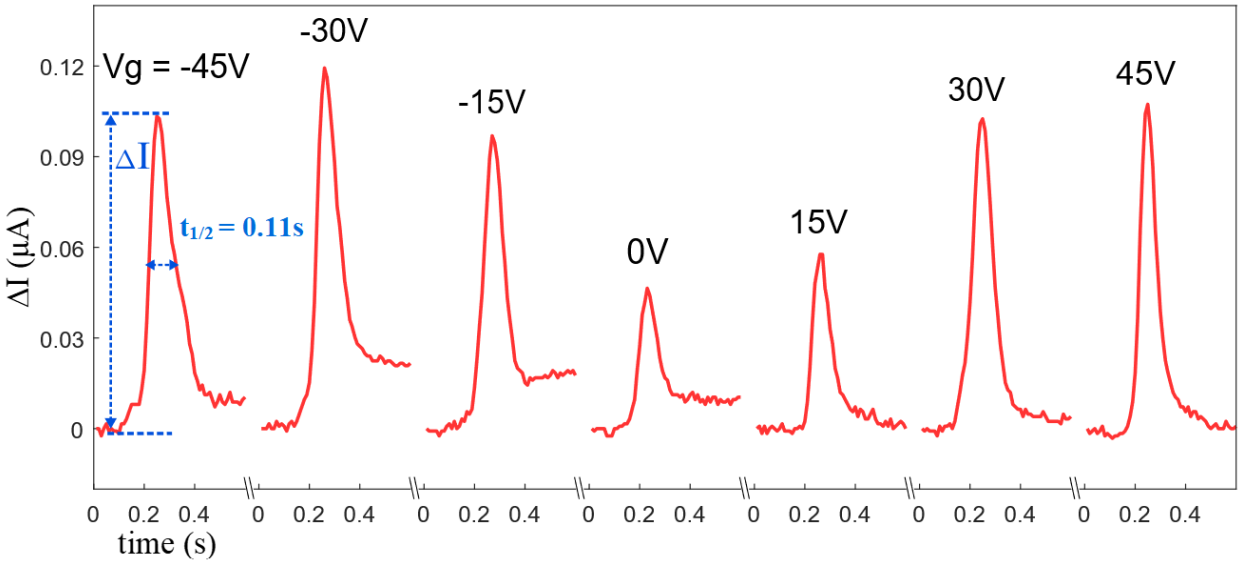

Figure 6.3 Fast responses of chloroform under seven different gate voltages with peak width $t_{1/2}$ down to 0.11 s.

The chemical-specific response trends with gate voltages, or gate spectra, can be utilized as the fingerprint in chemical discrimination as shown in Figure 6.4. It is evident that chemicals belonging to the same category share highly similar gate spectra, while the gate spectra of different chemical categories are distinct from one to another, serving as an ideal identifier for chemical classification. In addition, due to the high sensitivity of our graphene chemical sensor, chemicals within the same class, even with highly similar gate spectra, can also differentiate themselves from the difference in current magnitude. Chloroform, for example, has a much higher response compared to dichloromethane; as a result, an unidentified analyte from the 11 measured chemicals, which has already been categorized into organic chlorides due to the

resemblance in gate spectrum, can be further determined to be chloroform, if the response of this unidentified analyte is higher than a certain threshold value.

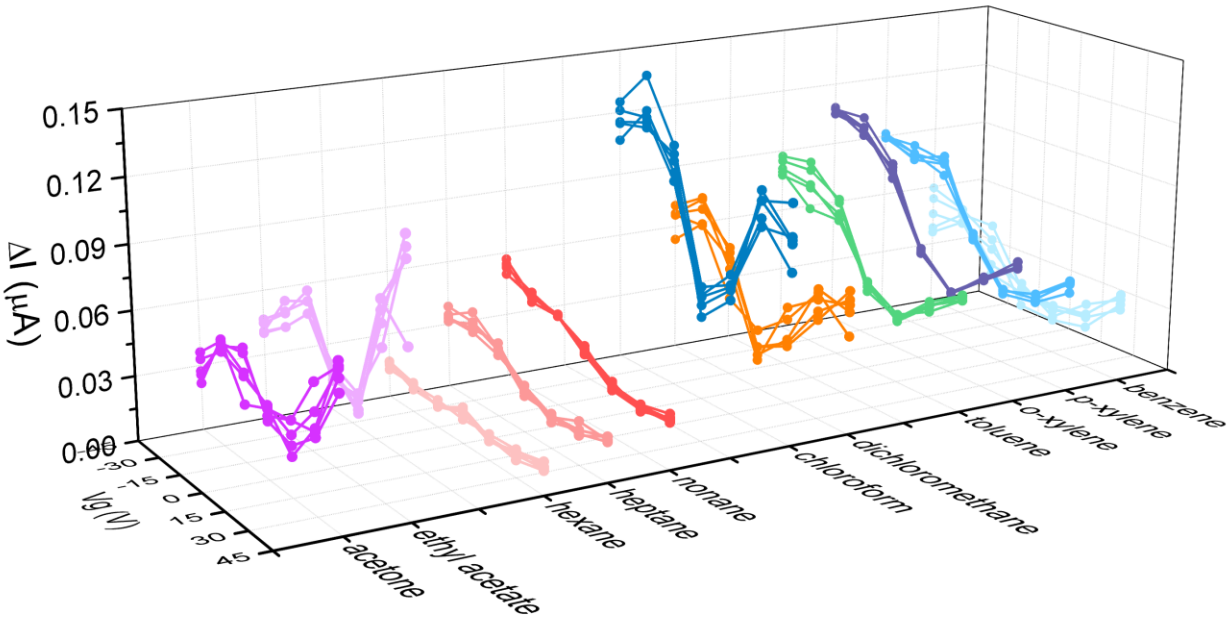

Figure 6.4 Response trends with gate voltages, or gate spectra, of all the 11 chemicals in the measurement.

PCA[161,162], which is an effective unsupervised data analysis tool, is applied to extract the covariance information from the current change, ΔI, data of the 11 measured chemicals. All 165 injections (11 chemicals with 15 injections for each), as shown in Figure 6.5, can be represented by points in a two-dimensional plane spanned by the first and second principal components with one-to-one correspondence. The first two principal components from PCA, PC1 and PC2, have contributions of 79.25% and 15.02%, respectively, which add up to an overall percentage of 92.27% of the data covariance information. It is evident from the PCA plot that 11 measured chemicals can be clearly grouped into 4 clusters – with the alkane cluster at the bottom left corner, aromatics at the bottom, organic chlorides at the center to the right and ketones/esters at the top. The distinct borders of the four clusters also indicate the graphene

chemical sensor's high performance in chemical discrimination, as verified later by the high accuracy obtained with various other classification methods.

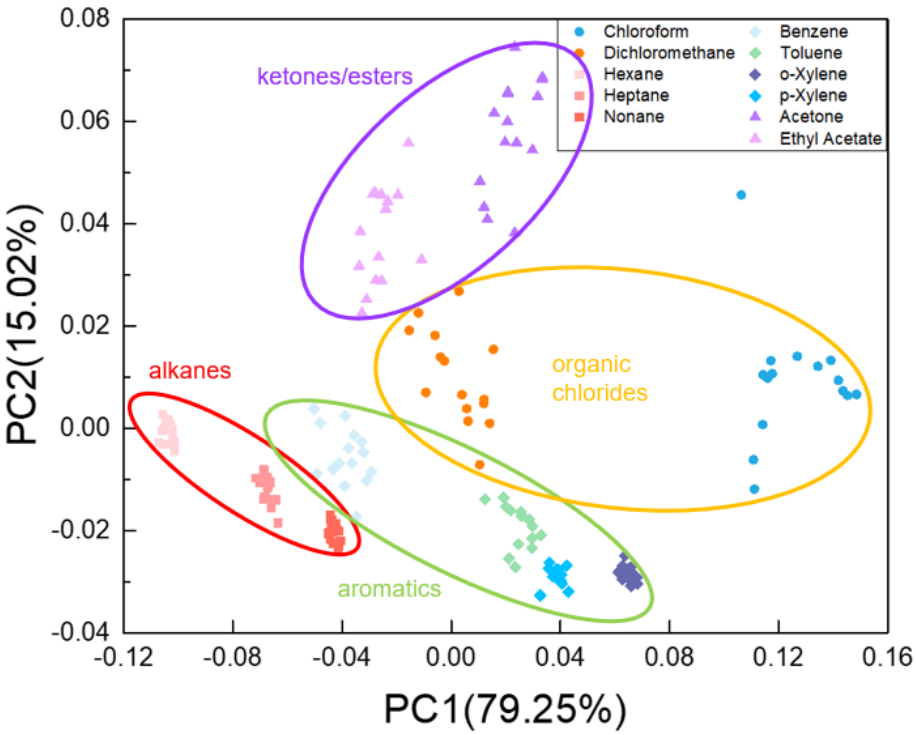

Figure 6.5 Principal component analysis result for all the 11 chemicals, with each dot representing a single analyte injection.

Alkanes show an outstanding result as characterized by both the tight distribution of each single chemical and the clear separation between different chemicals inside the same alkane category. Even though fluctuations may be significant in the responses of certain alkane species such as hexane, their small response magnitude limits the variances in gate spectrum to a relatively low level, which still allows for a tight distribution in the PCA figure. Aromatics including benzene, toluene and two xylenes, also demonstrate a remarkable discrimination result, with xylenes distributed as tightly as alkanes and only limited fluctuations in the other two chemicals. In contrast, organic chlorides as well as ketones/ethers, however, show a relatively severe scattering feature. This large variance, as reflected by the extreme case where one

chloroform dot even falls outside the organic chlorides circle in the PCA plot, is caused by the poor repeatability in current responses, which may be ascribed to the errors introduced by manual microsyringe injection. With their responses being both fast and intensive, these chemicals are typically more susceptible to manual process variations compared to alkanes and aromatics.

To further confirm the performance of the graphene sensor in chemical discrimination for real-world applications, four commonly used classification algorithms, i.e. k-nearest neighbors (KNN), linear discrimination analysis (LDA), support vector machine (SVM) and multi-layer perceptron (MLP) have been applied to the gate spectrum data set. Before implementing the algorithms, a 5-fold cross-validation (80% for training, 20% for testing) is first used to avoid data overfitting. The accuracy of classification into both the 11 specific chemicals and the 4 corresponding chemical categories is studied by using specific chemical and category labels accordingly. As summarized in Table 6.1, the classification result is rather satisfactory with at least 98.8% accuracy into specific chemicals and at least 93.9% accuracy into categories, indicating the robustness of data acquired by our graphene chemical sensor. It is worthy to point out that the accuracy has the potential to be further improved, with more gate voltages applied in the measurement for finer chemical gate spectra.

Classifiers	Classify by Chemicals	Classify by Categories
k-nearest neighbors	99.4%	99.4%
linear discrimination analysis	99.4%	93.9%
support vector machine	98.8%	97.6%
multi-layer perceptron	98.8%	98.2%

Table 6.1 Accuracy of graphene sensor discrimination of 11 analytes into specific chemicals or corresponding chemical categories using KNN, LDA, SVM and MLP methods, respectively.

The dosage response relation of the graphene chemical sensor, however, is not necessarily linear; instead, power law is commonly used to fit the relation empirically, with a power factor typically less than unity[131]. This deviation from linearity, or sublinearity, may create a more complicated scenario for analyte discrimination at different concentrations with the PCA method. Furthermore, at higher injections, saturation in current responses may happen, leading to more challenges for the discrimination of analytes with varying concentrations.

In light of these nonideal factors, to further examine our graphene sensor's capability for chemical discrimination of analytes with unknown concentrations, injections with various volumes (0.02 µL, 0.05 µL and 0.1 µL) are repeated three times for four analytes (nonane, o-xylene, chloroform and ethyl acetate), with each analyte being the representative for alkanes, aromatics, organic chlorides and ketones/ethers category respectively. The gate spectra of the four chemicals with various injection doses are plotted in Figure 6.6, with those of the same chemical showing a high similarity. The sublinearity and saturation are more severe in nonane, ethyl acetate and o-xylene while less significant in chloroform, as indicated by their current change magnitude at different dosages. Gate spectra also generally highly resemble their counterparts in Figure 6.4, showing a good reproducibility between the measurements with a time interval of several months. The minor deformation in the gate spectra of o-xylene at higher gate voltages may be explained by the shift of graphene's neutral point due to moisture in the air and hysteresis in the graphene transfer curve.

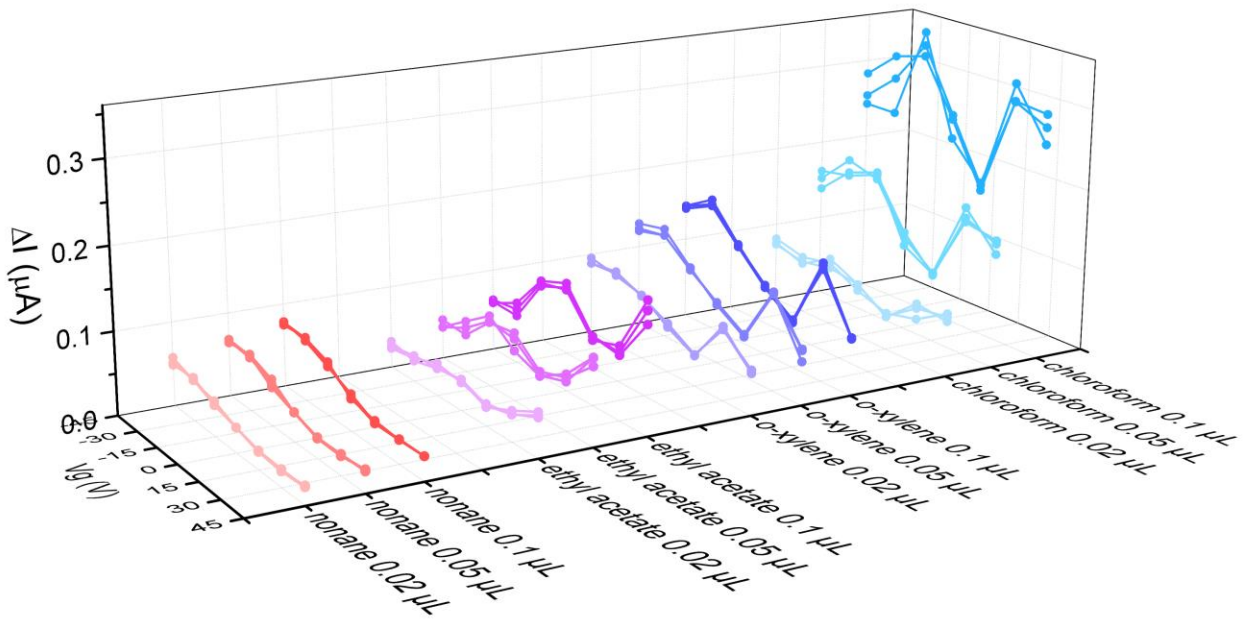

Figure 6.6 Gate spectra of nonane, ethyl acetate, o-xylene and chloroform with three injection doses of 0.02 μL, 0.05 μL and 0.1 μL.

The corresponding PCA plot for different injection doses is presented in Figure 6.7, with a large portion of contribution as high as 93.08% from the first principal component and only 5.68% from the second. Chloroform clearly has a dominant position in the PCA plot, and also shows the most significant scattering, which still comes from its less reliable repeatability explained before. In contrast, nonane, ethyl acetate and o-xylene show rather tight distributions at each injection dose. The sublinear effect or current saturation can indeed influence the results of PCA; this is implied by the closer distance between the 0.05 μL and 0.1 μL injections than the distance between the 0.02 μL and 0.5 μL injections in the nonane and o-xylene cases, however these four chemicals are still successfully separated clearly into four groups with distinct borders. This measurement further suggests our graphene chemical sensor's capability of discriminating analytes with varied doses, as well as its robustness against sublinearity and saturation, at least for these four representative chemicals.

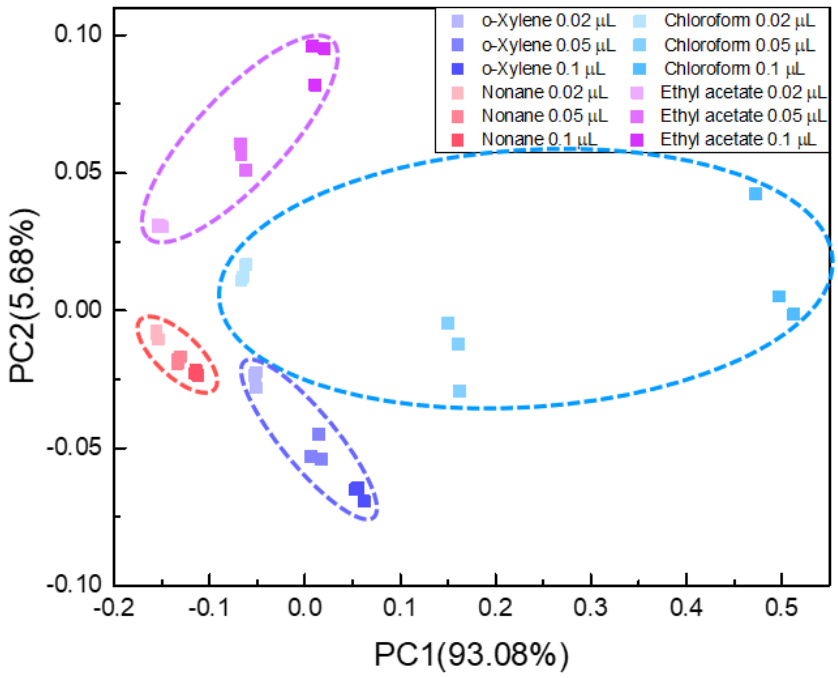

Figure 6.7 PCA plot for nonane, o-xylene, chloroform and ethyl acetate with varying injected volumes of 0.02 µL, 0.05 µL and 0.1 µL respectively.

6.4 Conclusion

In conclusion, a true label-free nanoelectronic sensing platform is pioneered by combining the electrical gate tunability of the graphene sensor responsivity (or gate spectra) with the PCA technique. In contrast to a conventional electronic sensor or electronic nose technology, surface functionalization on the sensor surface is no longer needed in order to achieve chemical discrimination. 11 measured analytes (acetone, ethyl acetate, chloroform, dichloromethane, pentane, heptane, nonane, benzene, toluene, o-xylene and p-xylene), as represented by 11 clusters of points in the PCA plot, are clearly grouped into separate regions with each representing a corresponding chemical category. The identification accuracy, as verified by multiple algorithms such as KNN, SVM, LDA and MLP, is rather satisfactory with at least 98.8% accuracy into the 11 specific chemicals used in the measurement and at least 93.9% accuracy into the four corresponding categories, indicating the robustness of the data acquired by

the graphene sensor. As a proof of concept, the dosage dependent measurements also show the capability of our graphene device for discrimination of analytes with unknown concentrations. This work lays the groundwork toward true label-free electronic sensor with high sensitivity and selectivity, and a novel electronic nose technology with better simplicity and higher accuracy.

6.5 Supplementary Information

6.5.1 Electrical Responses of All 11 Chemicals

Electrical responses of all the 11 measured chemicals are plotted in Figure 6.8, with the background current still flattened for a clearer comparison. Organic chlorides (chloroform and dichloromethane), alkanes (hexane, heptane and nonane) and aromatics (benzene, o-xylene, p-xylene and toluene) show positive current changes with this graphene sensor, while ketones/ethers (acetone and ethyl acetate) show negative responses instead. The bipolarity in current responses may be ascribed to interactions between graphene and the analyte molecules such as dipole-induced charge density modulation and capacitance modulation due to the electrostatic effect, where molecular dipole orientation plays a key role as suggested by Ref[128-131,163].

Uniquely for acetone, the negative peak is typically followed by a positive peak, in a sharp contrast to all the other chemicals. The maximum current change for acetone is therefore calculated as the difference between the two peak values. This double peak behavior of acetone implies a combination of simultaneous contributions from the two interactions. Besides the negative peak, possibly from dipole-induced charge modulation between the analyte molecules and graphene, a positive peak may also be induced by the electrostatic effect above graphene due to the higher dielectric constants of analytes. This double peak behavior, however, remains vague and more studies are needed in the future.

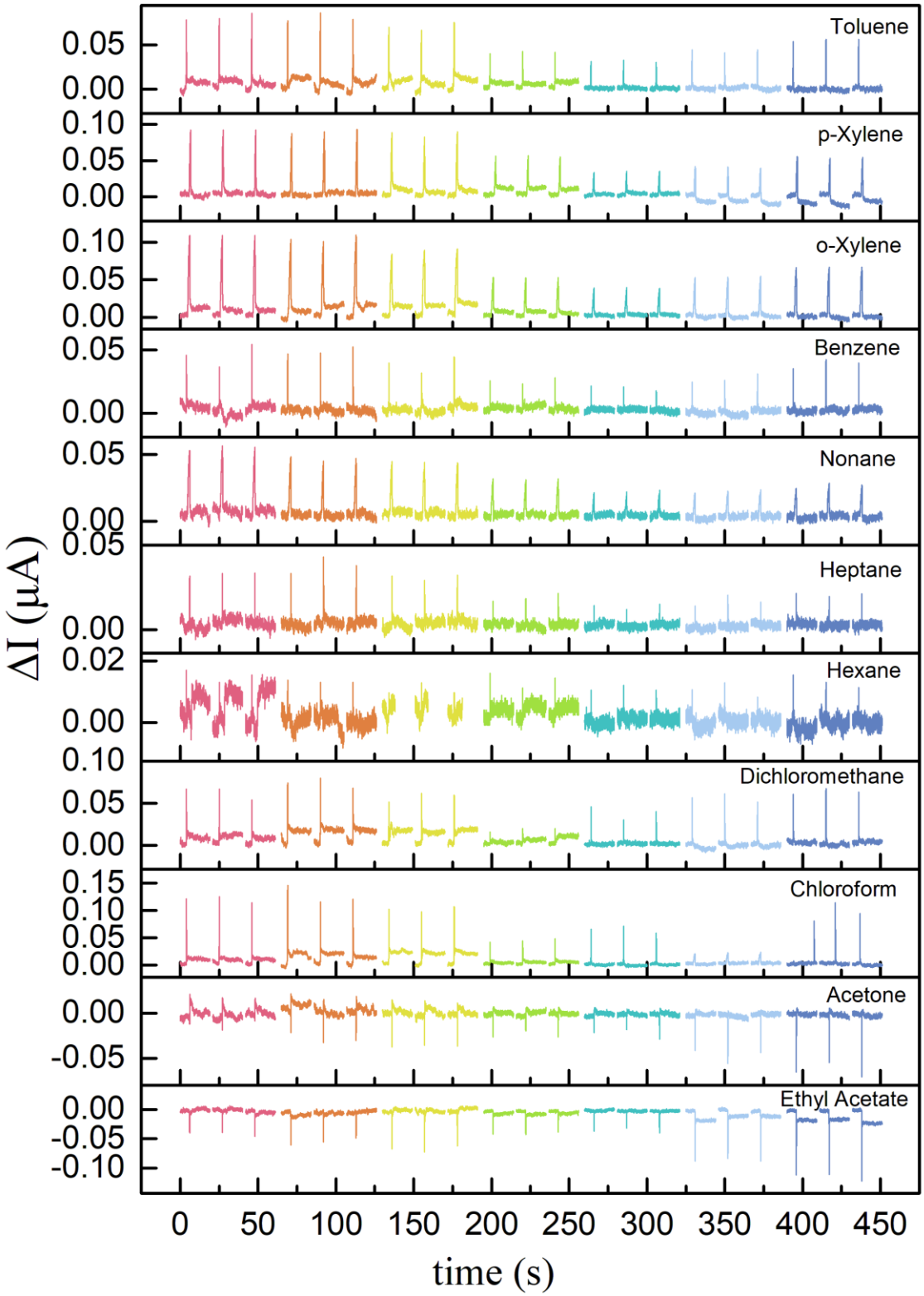

Figure 6.8 Graphene sensor temporal responses of all the 11 chemicals. Seven colors from left to right represent seven different gate voltages from - 45 V to 45 V with an interval of 15 V. Base current value is set as zero point with background flattened for a clearer view.

6.5.2 PCA with Current Change Percentage

Current change percentage ($\Delta I/I$) is readily derived from the current change divided by the base current:

$$\Delta I \equiv |I_{peak} - I_{base}|/I_{base}$$

$$\text{or } \Delta I \equiv \left|I_{peak\_positive} - I_{peak\_negative}\right|/I_{base} \text{ for acetone.}$$

The trends of current change percentage with gate voltages of o-xylene, nonane, chloroform and ethyl acetate, as the representatives for their chemical categories, are calculated and summarized in Figure 6.9. Due to the V-shape of the transfer curve of graphene, which determines the base current, a modification in the trend can be evident such as in the case of nonane.

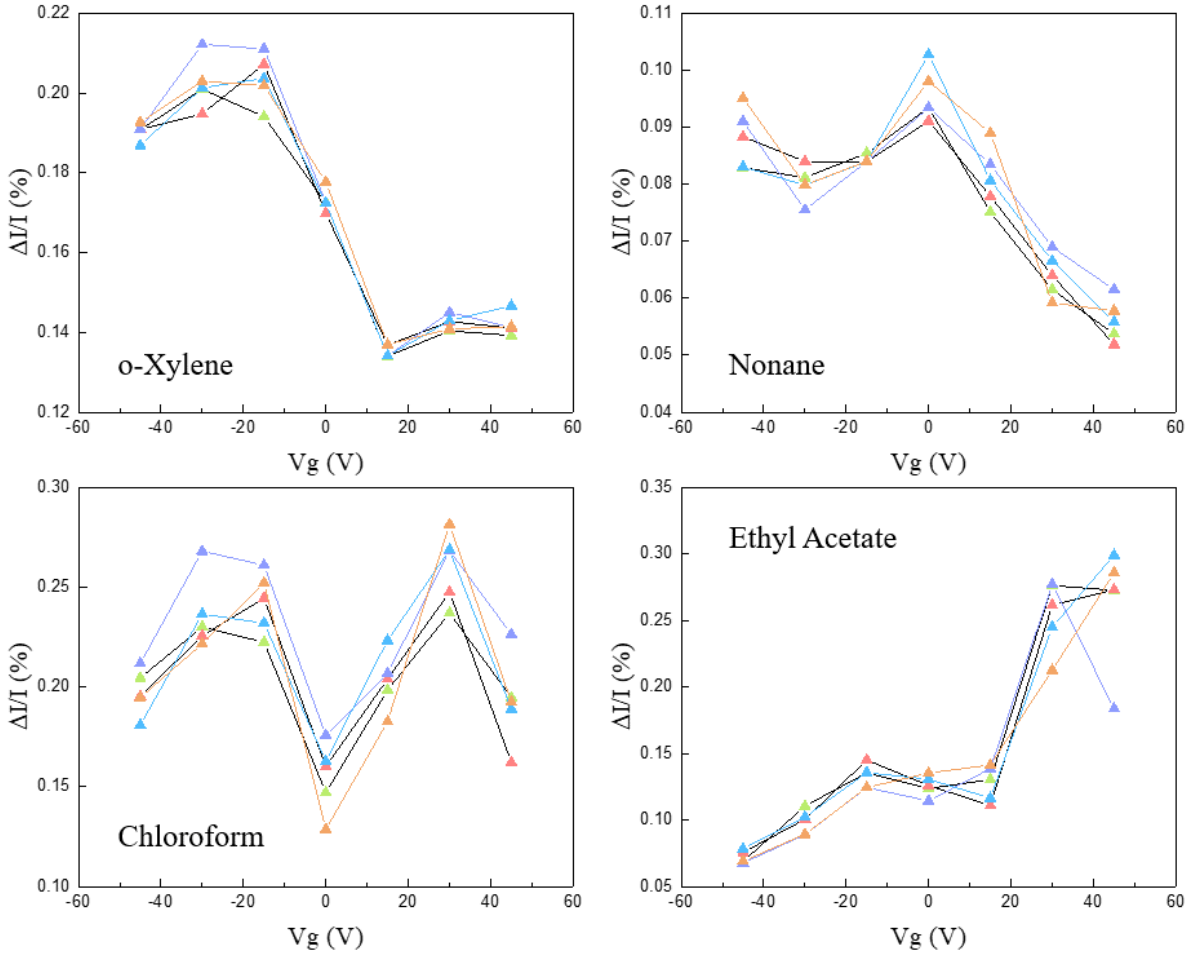

Figure 6.9 The current change percentage trends for four representative chemicals for each group.

The PCA method has also been applied with the current change percentage ($\Delta I/I$) with the plot shown in Figure 6.10. The overall locations for four chemical categories remain almost unchanged, still with alkanes at the bottom left corner, aromatics at the bottom, organic chlorides at the center to the right and ketones at the top with a few additional adjustments. This PCA result, however, is less impressive compared with the previous plot with current change gate spectra. Toluene and p-xylene are almost mixed up and can hardly be distinguished at all. The locations of acetone and ethyl acetate have also been flipped, but the boundary between the two remains clear. This discrepancy in PCA results may be partly ascribed to the shift in current background due to hysteresis, which may accumulate within the long measurement time to create a nonnegligible influence.

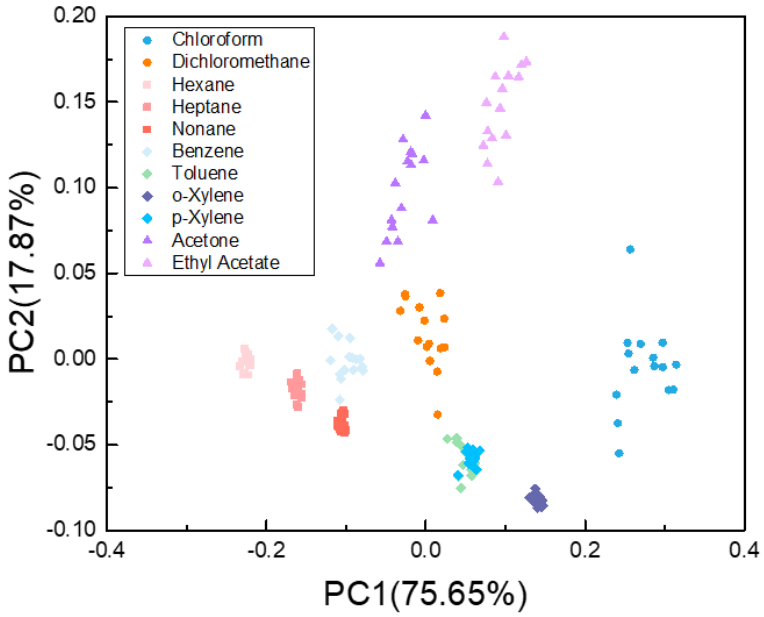

Figure 6.10 PCA plot with current change percentage of all 11 chemicals.

6.5.3 Conversion from Injected Volume to Mass and Concentration

Since the injected volume of each analyte (V_{inj}) is kept constantly at 0.05 µL, the mass injected is readily obtained through liquid density at 20 °C ($\rho_{analyte}$) and the GC split ratio (SR).

The amount of substance ($\gamma_{analyte}$) is consequently derived by dividing the corresponding analyte molecular weight (M_{mol}) as

$$\gamma_{analyte} = \frac{\rho_{analyte} V_{inj}}{SR \times M_{mol}}.$$

On the other hand, the amount of substance of helium carrier gas (γ_{He}) is estimated as[128]

$$\gamma_{He} = \frac{Q t_{1/2}}{V_{mol}}$$

where Q is the volumetric flow rate measured at the outlet of the graphene sensor, $t_{1/2}$ is FWHM peak width and V_{mol} is the molar volume at a temperature of 20 °C and pressure of 2.0 psi. The flow rate, Q, is measured around 4.5 mL/min and V_{mol} is calculated to be 21.16 L/mol for all analytes, while peak width $t_{1/2}$ has a large variance from ~0.07 s to ~1 s for the 11 chemicals used in the measurements. The GC split ratio (SR) is set to 1000 in the experiment.

Concentration is defined as $\gamma_{analyte}/\gamma_{He}$ and is listed in Table 6.2 with other essential parameters for all 11 chemicals. From this table, it is easily seen that injection mass for analytes stays relatively close since the liquid density stays within the same order of magnitude of water. The concentration of analytes, however, varies greatly with a ratio of more than 20. That significant variance originates mainly from the large instability of peak widths up to a factor of 10 and is exacerbated by the change in liquid density and molecular mass. Due to the relatively large variation in response peak width, which may stem from both instrument accuracy limit and manual injection, typical values for $t_{1/2}$ are listed for each analyte.

Analyte	**Liquid Density (g/mL)**	**Injection Mass (ng)**	**Molecular Mass (g/mol)**	**Amount of Substance (nmol)**	**Peak Width $t_{1/2}$ (s)**	**Concentration ($\times 10^3$ ppm)**
Chloroform	1.483	74.15	119.37	0.62	~0.1	~1.8
Dichloromethane	1.322	66.10	84.93	0.78	~0.1	~2.2

Acetone	0.791	39.55	58.08	0.68	~0.15	~1.3
Ethyl Acetate	0.902	45.10	88.11	0.51	~0.07	~2.1
Hexane	0.626	31.30	72.15	0.43	~0.1	~1.2
Heptane	0.684	34.20	100.21	0.34	~0.1	~0.96
Nonane	0.718	35.90	128.25	0.28	~1	~0.079
Benzene	0.879	43.95	78.11	0.56	~0.1	~1.6
Toluene	0.867	43.35	92.14	0.47	~0.2	~0.66
o-Xylene	0.880	44.00	106.16	0.41	~1	~0.12
p-Xylene	0.861	43.05	106.16	0.41	~0.7	~0.16

Table 6.2 The conversion from 0.05 μL injected volume to corresponding injected mass and concentration for all 11 analyte in measurements. Liquid density at 20 °C and molecular mass data are obtained from PubChem[164]. Typical values are used for peak width $t_{1/2}$ values due to the large variation.

6.5.4 PCA with Mass and Concentration Normalized Response

PCA can also be applied for the current change normalized by mass or analyte concentration listed above, for a broader understanding of the device behavior. From the mass-normalized current change PCA plot (Figure 6.11), it can be clearly seen that the four chemical categories (alkanes, aromatics, organic chlorides and ketones) can be separated to bottom left, bottom right, lower central and top central area, respectively. The first principal component contributes 68.25% to the total variance information and the second contributes 24.65%, with a total decent contribution of 92.90%. In addition, the severe scattering feature of chloroform and dichloromethane is also suppressed, leading to a more balanced analyte distribution in the plot. In this scenario, however, benzene and dichloromethane are only partially discriminated. Though better than its counterpart with current change percentage, which fails in separating p-xylene and toluene (Figure 6.10), this result is not as great as that obtained using the current change gate spectrum which can separate all 11 analytes in the measurements (Figure 6.5).

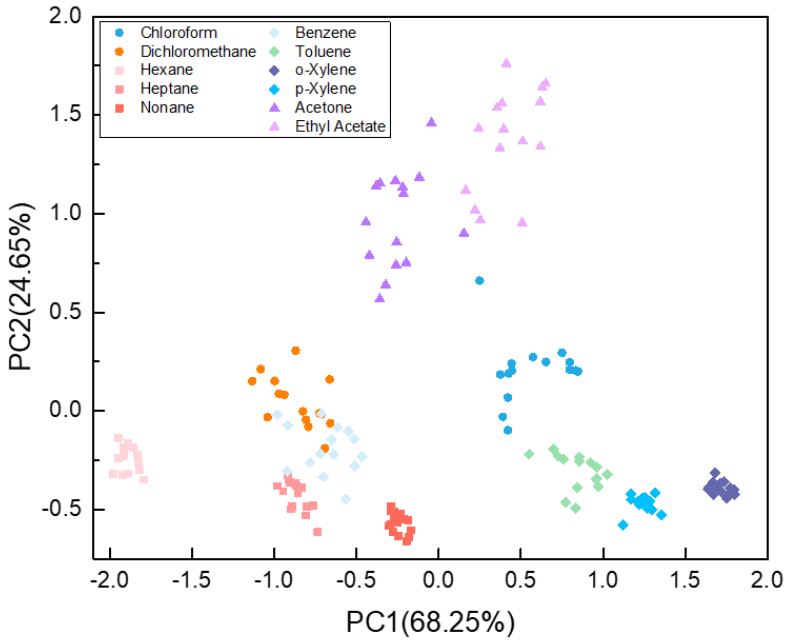

Figure 6.11 PCA plot for injected mass-normalized current change for all the 11 chemicals.

As listed in Table 6.1, the variation in typical peak width values is huge, leading to a great variance in concentration with a factor of more than 20. The PCA method can be applied to the data normalized by concentration as well, which is shown in Figure 6.12. Unsurprisingly, nonane, o-xylene and p-xylene are far separated from other chemicals due to their relatively large peak widths (~1 s), while for those chemicals with faster response ($t_{1/2}$ ~ 0.1 s), the distribution is rather close. Basic features behave similarly as in previous cases such that hexane, heptane and benzene remain in proximity, and so do acetone and acetate. However, organic chlorides (chloroform and dichloromethane) are interspersed with ketones and are nearly impossible to be grouped, as are the three chemicals far from others. The 99.19% and 0.52% contributions from PC1 and PC2 also suggest the reduced effectivity of PCA when the current change is normalized by the concentration. Though concentration-normalized PCA does not render as outstanding of a result as other methods, the distinct difference in analyte response peak width still remains a promising dimension as an auxiliary criterion for better discrimination.

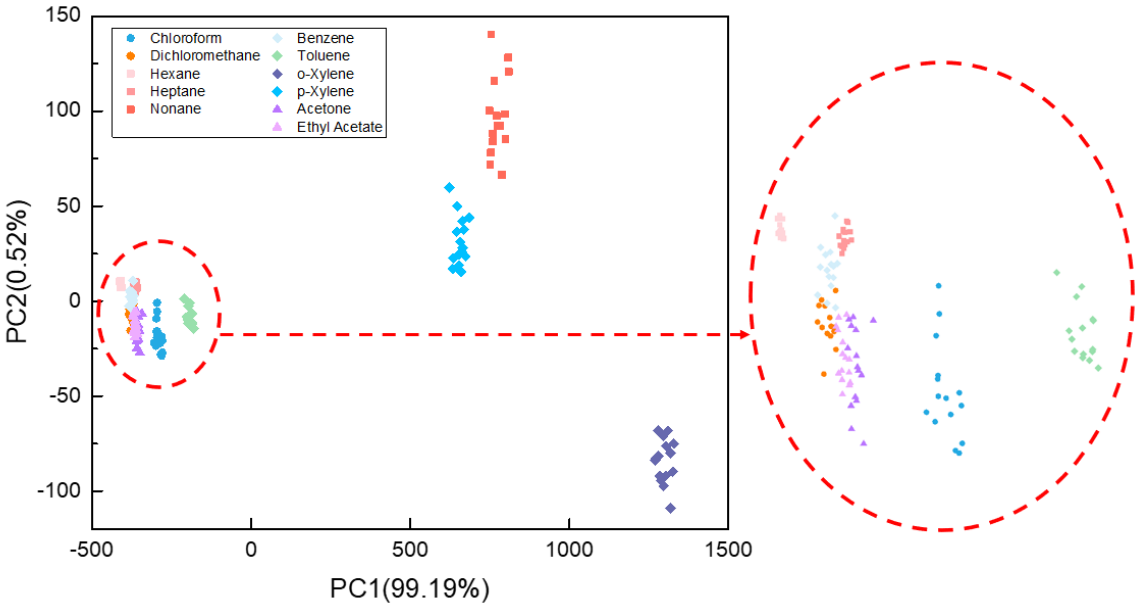

Figure 6.12 PCA result with current change normalized by estimated concentration.

Chapter 7 Conclusions and Future Work

7.1 Conclusions

This work focuses on 2D crystals growth and their nanoelectronic device applications. CVD growth of monolayer MoS_2 is first introduced for both monocrystalline flakes and large area polycrystalline continuous film growth, followed by various characterization methods to examine growth quality. For the application part, a lateral structured graphene-silicon-graphene BJT with electrically tunable gain has been achieved, with a direct current gain over 20. A true label-free nanoelectronic sensing platform is also pioneered by combining the electrical gate tunability of the graphene sensor responsivity (or gate spectra) with the PCA technique, with accurate discrimination of chemical vapors achieved. This lays the groundwork toward a true label-free electronic sensor with high sensitivity and selectivity, and a novel electronic nose technology with better simplicity and higher accuracy.

Chapter 3 presents the CVD results of monolayer MoS_2 growth. Both large area continuous polycrystalline thin film growth and isolated monocrystalline flake growth have been demonstrated under corresponding growth configurations. Various characterization methods such as optical microscopy, PL, Raman spectrum, SEM and AFM are subsequently utilized to examine the growth quality. For large area grown samples, mobility is further extracted from a corresponding centimeter-scale FET with acceptable values.

In Chapter 4, an electrically tunable lateral structured graphene-Si-graphene BJT device has been demonstrated, with a direct current gain over 20. By utilizing graphene's Fermi level tunability, the graphene BJT device can be smoothly and readily tuned from non-amplification

mode to current amplification mode with graphene emitter controlled simply by a top gate electrode. This graphene BJT device, at the same time, also exhibits a potential for significant enhancement with base width downscaling. With decent performance, simplicity and extensibility, this novel graphene BJT device demonstrates a promising way forward for nanoscale BJT applications.

In Chapter 5, the proposed mechanisms in pioneering background works have been first briefly summarized, i.e. analyte molecular dipole-induced charge density modulation and electrostatic effect-induced capacitance modulation. To integrate with a hand-held gas chromatography system, a direct current graphene sensor is redesigned and fabricated with a miniature size of 1 cm by 0.7 cm. The miniaturized graphene sensor has comparable sensitivity and even faster responses with only half or a third of peak width compared to its full-size counterpart. Comparisons on different flow channel designs indicate that larger channel coverage on graphene and larger flow channel height typically lead to higher electrical responses. In the end, a tin oxide-decorated graphene chemical sensor is fabricated and tested for formaldehyde vapor sensing. While a pristine graphene sensor shows no difference between the headspace vapor of a formaldehyde water solution and that of pure water, the tin oxide-decorated graphene sensor exhibits 50% higher responses for formaldehyde vapor samples compared to the pure water control group, indicating its capability for formaldehyde sensing.

In chapter 6, a true label-free nanoelectronic sensing platform is pioneered by combining the electrical gate tunability of graphene sensor responsivity (or gate spectra) with PCA technique. In contrast to a conventional electronic sensor or electronic nose technology, surface functionalization on the sensor surface is no longer needed in order to achieve chemical discrimination. 11 measured analytes from ketones/ethers, organic chlorides, alkanes and

aromatics, as represented by 11 clusters of points in the PCA plot, are clearly grouped into separate regions with each representing a corresponding chemical category. The identification accuracy, as verified by multiple algorithms such as KNN, SVM, LDA and MLP, is rather satisfactory with at least 98.8% accuracy into the 11 specific chemicals used in the measurement and at least 93.9% accuracy into the four corresponding categories, indicating the robustness of the data acquired by the graphene sensor. This work should lay the groundwork toward true label-free electronic sensor with high sensitivity and selectivity, and a novel electronic nose technology with better simplicity and higher accuracy.

7.2 Further Work

7.2.1 Alternative Promising Designs for Graphene Bipolar Junction Transistor

Lateral structured graphene BJT has been previously fabricated in chapter 4, with graphene sheets laying on the silicon surface to form the emitter and collector while with the thin strip in between is etched by oxygen plasma to act as the silicon base. This lateral structured graphene BJT, however, is not necessarily tied to bulk materials. The simplicity in device structure and fabrication gives it broad applicability such as integration with other two-dimensional materials like MoS_2, which can potentially replace silicon to form atomically thin BJT devices.

Even though the direct current gain of the lateral graphene BJT device can be pushed up to 20 with higher biases, this value is still less impressive than a traditional silicon BJT with a current gain typically larger than 100. One major reason for this issue, as implied by the distinct Early effect, may be the long base width, which is limited to 0.75 μm by the resolution of the i-line stepper (λ = 365 nm) used in our photolithography process. In contrast, the base width of modern silicon BJTs is typically downscaled to ~0.1 μm for higher gain.

A graphene BJT with a vertical structure is proposed as a promising way to overcome the limitation imposed by photolithography tools. Instead of using bulk silicon, a thin silicon layer with a desired thickness can be used as the base, with graphene transferred on both sides to form the emitter and collector, respectively. The schematic of vertical graphene BJT is shown in Figure 7.1.

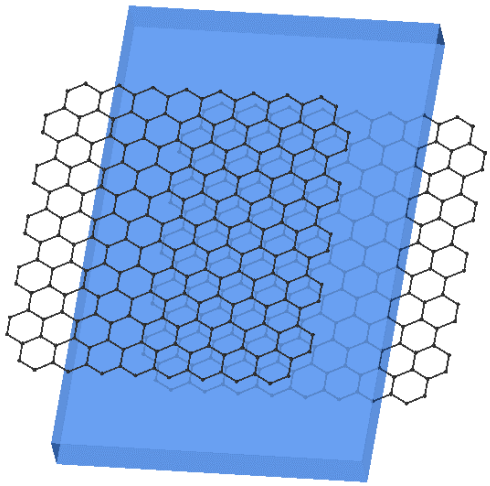

Figure 7.1 Schematic of vertical graphene BJT. Top and bottom graphene sheets act as the emitter and collector with the middle layer (thin silicon or other 2D materials) serving as the base.

This vertical structure maintains the extensibility in integration with other two-dimensional materials serving as the base, such as TMDCs. Unlike the case where a thin silicon slab is used, which is fragile and susceptible to cracks and breakage during the fabrication process, two-dimensional materials are in general easier to transfer while still maintaining a high crystal quality and decent junction quality. Meanwhile, the thickness of the vertical graphene BJT can also be reduced to an atomic level, paving a new way for nanoscale BJT device applications.

7.2.2 Graphene Chemical Sensor with Tedlar Bag Integration

In previous chapters, graphene chemical sensors are connected to GC a injector for manual headspace vapor or pure liquid injection. This manual process, however, may lead to relatively large variations in analyte response and peak decay rate. Integration with Tedlar bags is a feasible choice to get rid of such variations, and at the same time, provides a testing environment closer to the real world scene for the graphene sensors. A calculated amount of single or multiple chemicals can be first injected into Tedlar bags prefilled with an appropriate amount of helium carrier gas, followed by a heating process for chemical evaporation to achieve the desired concentration. Another Tedlar bag filled only with the same amount of helium can be similarly prepared as a control group and connected to the other end of Y-shape connectors as described in Figure 7.2.

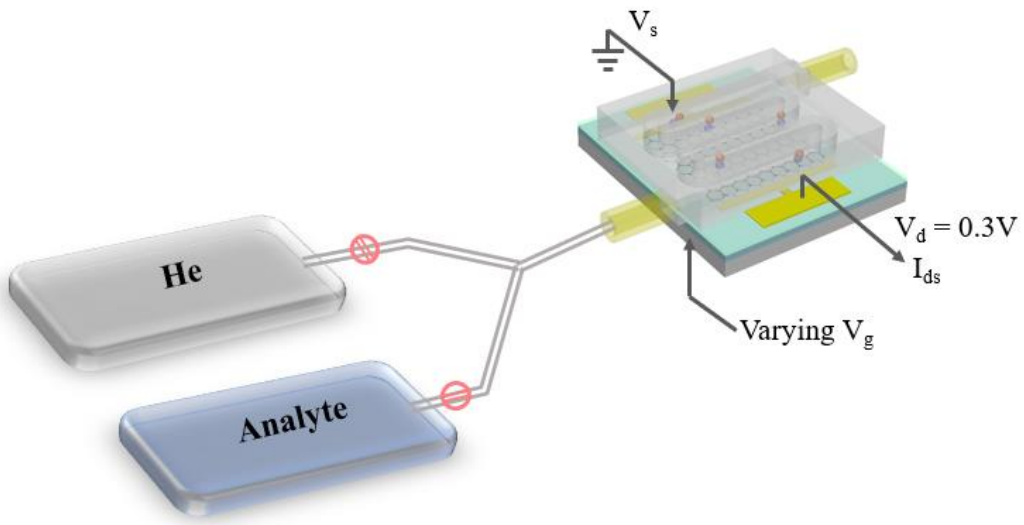

Figure 7.2 Chemical sensing and discrimination measurement setup with Tedlar bag integration.

In our chemical discrimination experiment, the injected analytes are limited to pure chemicals, leaving the capability of small footprint graphene chemical sensor in chemical mixture discrimination underexplored. With the help of Tedlar bags, mixtures of desired

chemicals with almost arbitrary concentrations can be readily prepared, which is superior to headspace gas mixtures and liquid mixtures. In headspace gas mixtures, analyte concentrations are primarily determined by the corresponding saturated vapor pressure and therefore hard to change; in addition, the headspace mixtures are more susceptible to environmental fluctuations such as ambient air moisture variation. The liquid mixtures, while maintaining the highest purity of each analyte, suffer from the issue of solubility. At the same time, variations caused by manual syringe injection and/or the evaporation process in the GC injector can be avoided with Tedlar bags, minimizing the difference in time needed from the GC injector to the graphene sensor for each mixture component.

While only current change information has been utilized for vapor discrimination, the decay rate of each response is also another promising dimension containing physisorption related information. Decay rate, however, is less tolerant to the variations in measurement such as that caused by manual microsyringe injection. With the decay rates of nonane, chloroform, ethyl acetate, toluene, o-xylene and p-xylene extracted with an exponential fit, significant variances appear in the fitted data at individual gate voltages, which blur the trend of decay rate with gate voltage.

The benefit of integration with Tedlar bags is twofold. With this reliable analyte vapor delivery method, variations induced by the manual injection process and the chemical evaporation process in GC are minimized, which leads to higher consistency in chemical responses including the decaying part. In addition, a transition from manual microsyringe liquid injection to Tedlar bag gas delivery may create a steady state between current rising and decaying, leading to better controllability over the decay process. For even higher accuracy in decay rate fitting, automatic microsyringe pumps filled with a gas analyte may be chosen as

alternatives for Tedlar bags, but with high cost and possible issues on injection duration time due to the relatively small syringe volume.

Bibliography

[1] H. W. Kroto, J. R. Heath, S. C. O'Brien, R. F. Curl, and R. E. Smalley, Nature **318**, 162 (1985).
[2] I. de la Calle and V. Romero-Rivas, in *Applications of Nanomaterials*, edited by S. Mohan Bhagyaraj *et al.* (Woodhead Publishing, 2018), pp. 251.
[3] M. Meyyappan, L. Delzeit, A. Cassell, and D. Hash, Plasma Sources Science and Technology **12**, 205 (2003).
[4] S. B. Sinnott, R. Andrews, D. Qian, A. M. Rao, Z. Mao, E. C. Dickey, and F. Derbyshire, Chemical Physics Letters **315**, 25 (1999).
[5] D. Takagi, Y. Homma, H. Hibino, S. Suzuki, and Y. Kobayashi, Nano Letters **6**, 2642 (2006).
[6] R. Saito, G. Dresselhaus, and M. S. Dresselhaus, *Physical Properties of Carbon Nanotubes* 1998), p.^pp. 272.
[7] K. S. Novoselov, A. K. Geim, S. V. Morozov, D. Jiang, Y. Zhang, S. V. Dubonos, I. V. Grigorieva, and A. A. Firsov, Science **306**, 666 (2004).
[8] T. Kyotani, N. Sonobe, and A. Tomita, Nature **331**, 331 (1988).
[9] D. R. Cooper *et al.*, ISRN Condensed Matter Physics **2012**, 501686 (2012).
[10] A. H. Castro Neto, F. Guinea, N. M. R. Peres, K. S. Novoselov, and A. K. Geim, Reviews of Modern Physics **81**, 109 (2009).
[11] P. R. Wallace, Physical Review **71**, 622 (1947).
[12] C. K. Hu, *Modern Semiconductor Devices for Integrated Circuits* (Pearson, 2010), p.^pp. 291-323.
[13] K. I. Bolotin, K. J. Sikes, Z. Jiang, M. Klima, G. Fudenberg, J. Hone, P. Kim, and H. L. Stormer, Solid State Communications **146**, 351 (2008).
[14] X. Du, I. Skachko, A. Barker, and E. Y. Andrei, Nature Nanotechnology **3**, 491 (2008).
[15] J. H. Chen, C. Jang, S. Adam, M. S. Fuhrer, E. D. Williams, and M. Ishigami, Nature Physics **4**, 377 (2008).
[16] E. H. Hwang, S. Adam, and S. D. Sarma, Physical Review Letters **98**, 186806 (2007).
[17] K. Nomura and A. H. MacDonald, Physical Review Letters **96**, 256602 (2006).
[18] J. Sabio, C. Seoánez, S. Fratini, F. Guinea, A. H. C. Neto, and F. Sols, Physical Review B **77**, 195409 (2008).
[19] J.-H. Chen, C. Jang, S. Xiao, M. Ishigami, and M. S. Fuhrer, Nature Nanotechnology **3**, 206 (2008).
[20] M. Ishigami, J. H. Chen, W. G. Cullen, M. S. Fuhrer, and E. D. Williams, Nano Letters **7**, 1643 (2007).
[21] S. V. Morozov, K. S. Novoselov, M. I. Katsnelson, F. Schedin, D. C. Elias, J. A. Jaszczak, and A. K. Geim, Physical Review Letters **100**, 016602 (2008).
[22] J. C. Meyer, A. K. Geim, M. I. Katsnelson, K. S. Novoselov, T. J. Booth, and S. Roth, Nature **446**, 60 (2007).

[23] L. Lin *et al.*, Nature Communications **10**, 1912 (2019).
[24] Y. Ahn, H. Kim, Y.-H. Kim, Y. Yi, and S.-I. Kim, Applied Physics Letters **102**, 091602 (2013).
[25] J. W. Suk, W. H. Lee, J. Lee, H. Chou, R. D. Piner, Y. Hao, D. Akinwande, and R. S. Ruoff, Nano Letters **13**, 1462 (2013).
[26] X. Liang, Z. Fu, and S. Y. Chou, Nano Letters **7**, 3840 (2007).
[27] M. Chen, H. Nam, H. Rokni, S. Wi, J. S. Yoon, P. Chen, K. Kurabayashi, W. Lu, and X. Liang, ACS Nano **9**, 8773 (2015).
[28] A. N. Sidorov, M. M. Yazdanpanah, R. Jalilian, P. J. Ouseph, R. W. Cohn, and G. U. Sumanasekera, Nanotechnology **18**, 135301 (2007).
[29] X. Liang, A. S. P. Chang, Y. Zhang, B. D. Harteneck, H. Choo, D. L. Olynick, and S. Cabrini, Nano Letters **9**, 467 (2009).
[30] Y. Hernandez *et al.*, Nature Nanotechnology **3**, 563 (2008).
[31] J. Hass, W. A. de Heer, and E. H. Conrad, Journal of Physics: Condensed Matter **20**, 323202 (2008).
[32] C. Berger *et al.*, The Journal of Physical Chemistry B **108**, 19912 (2004).
[33] M. Losurdo, M. M. Giangregorio, P. Capezzuto, and G. Bruno, Physical Chemistry Chemical Physics **13**, 20836 (2011).
[34] S. Lee, K. Lee, and Z. Zhong, Nano Letters **10**, 4702 (2010).
[35] A. Reina, X. Jia, J. Ho, D. Nezich, H. Son, V. Bulovic, M. S. Dresselhaus, and J. Kong, Nano Letters **9**, 30 (2009).
[36] X. Li *et al.*, Science **324**, 1312 (2009).
[37] X. Li, W. Cai, L. Colombo, and R. S. Ruoff, Nano Letters **9**, 4268 (2009).
[38] Q. Yu, J. Lian, S. Siriponglert, H. Li, Y. P. Chen, and S.-S. Pei, Applied Physics Letters **93**, 113103 (2008).
[39] R. R. Nair, P. Blake, A. N. Grigorenko, K. S. Novoselov, T. J. Booth, T. Stauber, N. M. R. Peres, and A. K. Geim, Science **320**, 1308 (2008).
[40] J. Kim, F. Kim, and J. Huang, Materials Today **13**, 28 (2010).
[41] D. Zhang *et al.*, in *2019 Conference on Lasers and Electro-Optics (CLEO)*2019), pp. 1.
[42] P. Blake, E. W. Hill, A. H. Castro Neto, K. S. Novoselov, D. Jiang, R. Yang, T. J. Booth, and A. K. Geim, Applied Physics Letters **91**, 063124 (2007).
[43] A. C. Ferrari and D. M. Basko, Nature Nanotechnology **8**, 235 (2013).
[44] A. C. Ferrari *et al.*, Physical Review Letters **97**, 187401 (2006).
[45] Y. Y. Wang, Z. H. Ni, Z. X. Shen, H. M. Wang, and Y. H. Wu, Applied Physics Letters **92**, 043121 (2008).
[46] R. Rao, D. Tishler, J. Katoch, and M. Ishigami, Physical Review B **84**, 113406 (2011).
[47] F. Tuinstra and J. L. Koenig, The Journal of Chemical Physics **53**, 1126 (1970).
[48] I. Calizo, I. Bejenari, M. Rahman, G. Liu, and A. A. Balandin, Journal of Applied Physics **106**, 043509 (2009).
[49] S. Tongay, M. Lemaitre, X. Miao, B. Gila, B. R. Appleton, and A. F. Hebard, Physical Review X **2**, 011002 (2012).
[50] H. Yang *et al.*, Science **336**, 1140 (2012).
[51] The International Technology Roadmap for Semiconductors: 2007 https://www.semiconductors.org/wp-content/uploads/2018/08/2007PIDS.pdf.
[52] Y.-J. Yu, Y. Zhao, S. Ryu, L. E. Brus, K. S. Kim, and P. Kim, Nano Letters **9**, 3430 (2009).

[53] C.-Y. Su, D. Fu, A.-Y. Lu, K.-K. Liu, Y. Xu, Z.-Y. Juang, and L.-J. Li, Nanotechnology **22**, 185309 (2011).
[54] S. M. S. K. K. Ng, *Physics of Semiconductor Devices* 2006).
[55] S. Y. Zhou, G. H. Gweon, A. V. Fedorov, P. N. First, W. A. de Heer, D. H. Lee, F. Guinea, A. H. Castro Neto, and A. Lanzara, Nature Materials **6**, 770 (2007).
[56] R. Balog *et al.*, Nature Materials **9**, 315 (2010).
[57] L. Brey and H. A. Fertig, Physical Review B **73**, 235411 (2006).
[58] M. Y. Han, B. Özyilmaz, Y. Zhang, and P. Kim, Physical Review Letters **98**, 206805 (2007).
[59] M. Y. Han, J. C. Brant, and P. Kim, Physical Review Letters **104**, 056801 (2010).
[60] Y.-W. Son, M. L. Cohen, and S. G. Louie, Physical Review Letters **97**, 216803 (2006).
[61] E. McCann, Physical Review B **74**, 161403 (2006).
[62] E. V. Castro, K. S. Novoselov, S. V. Morozov, N. M. R. Peres, J. M. B. L. dos Santos, J. Nilsson, F. Guinea, A. K. Geim, and A. H. C. Neto, Physical Review Letters **99**, 216802 (2007).
[63] X. Ling, H. Wang, S. Huang, F. Xia, and M. S. Dresselhaus, Proceedings of the National Academy of Sciences **112**, 4523 (2015).
[64] L. Li, Y. Yu, G. J. Ye, Q. Ge, X. Ou, H. Wu, D. Feng, X. H. Chen, and Y. Zhang, Nature Nanotechnology **9**, 372 (2014).
[65] T. Low, A. S. Rodin, A. Carvalho, Y. Jiang, H. Wang, F. Xia, and A. H. Castro Neto, Physical Review B **90**, 075434 (2014).
[66] B. Deng *et al.*, Nature Communications **8**, 14474 (2017).
[67] F. Xia, H. Wang, J. C. M. Hwang, A. H. C. Neto, and L. Yang, Nature Reviews Physics **1**, 306 (2019).
[68] J. D. Wood *et al.*, Nano Letters **14**, 6964 (2014).
[69] K. F. Mak, C. Lee, J. Hone, J. Shan, and T. F. Heinz, Physical Review Letters **105**, 136805 (2010).
[70] *MoS2: Materials, Physics, and Devices* (Springer International Publishing, 2014), p.^pp. 291.
[71] E. S. Kadantsev and P. Hawrylak, Solid State Communications **152**, 909 (2012).
[72] J. K. Ellis, M. J. Lucero, and G. E. Scuseria, Applied Physics Letters **99**, 261908 (2011).
[73] J. Gusakova, X. Wang, L. L. Shiau, A. Krivosheeva, V. Shaposhnikov, V. Borisenko, V. Gusakov, and B. K. Tay, physica status solidi (a) **214**, 1700218 (2017).
[74] K. S. Novoselov, D. Jiang, F. Schedin, T. J. Booth, V. V. Khotkevich, S. V. Morozov, and A. K. Geim, Proceedings of the National Academy of Sciences of the United States of America **102**, 10451 (2005).
[75] B. Radisavljevic, A. Radenovic, J. Brivio, V. Giacometti, and A. Kis, Nature Nanotechnology **6**, 147 (2011).
[76] T. Schram *et al.*, in *2017 47th European Solid-State Device Research Conference (ESSDERC)*2017), pp. 212.
[77] J. R. Schaibley, H. Yu, G. Clark, P. Rivera, J. S. Ross, K. L. Seyler, W. Yao, and X. Xu, Nature Reviews Materials **1**, 16055 (2016).
[78] K. F. Mak, K. He, J. Shan, and T. F. Heinz, Nature Nanotechnology **7**, 494 (2012).
[79] C. Mai, A. Barrette, Y. Yu, Y. G. Semenov, K. W. Kim, L. Cao, and K. Gundogdu, Nano Letters **14**, 202 (2014).
[80] L. Xie and X. Cui, Proceedings of the National Academy of Sciences **113**, 3746 (2016).

[81] D. Xiao, G.-B. Liu, W. Feng, X. Xu, and W. Yao, Physical Review Letters **108**, 196802 (2012).
[82] X. Xu, W. Yao, D. Xiao, and T. F. Heinz, Nature Physics **10**, 343 (2014).
[83] H. Zeng, J. Dai, W. Yao, D. Xiao, and X. Cui, Nature Nanotechnology **7**, 490 (2012).
[84] Y.-C. Lin, D. O. Dumcenco, Y.-S. Huang, and K. Suenaga, Nature Nanotechnology **9**, 391 (2014).
[85] Y. Yu *et al.*, Nature Chemistry **10**, 638 (2018).
[86] M. A. Py and R. R. Haering, Canadian Journal of Physics **61**, 76 (1983).
[87] L. F. Mattheiss, Physical Review B **8**, 3719 (1973).
[88] G. Eda, H. Yamaguchi, D. Voiry, T. Fujita, M. Chen, and M. Chhowalla, Nano Letters **11**, 5111 (2011).
[89] X. Gan, L. Y. S. Lee, K.-y. Wong, T. W. Lo, K. H. Ho, D. Y. Lei, and H. Zhao, ACS Applied Energy Materials **1**, 4754 (2018).
[90] T. Li and G. Galli, The Journal of Physical Chemistry C **111**, 16192 (2007).
[91] S. Lebègue and O. Eriksson, Physical Review B **79**, 115409 (2009).
[92] W. Jin *et al.*, Physical Review Letters **111**, 106801 (2013).
[93] A. Splendiani, L. Sun, Y. Zhang, T. Li, J. Kim, C.-Y. Chim, G. Galli, and F. Wang, Nano Letters **10**, 1271 (2010).
[94] T. Cheiwchanchamnangij and W. R. L. Lambrecht, Physical Review B **85**, 205302 (2012).
[95] K. F. Mak, K. L. McGill, J. Park, and P. L. McEuen, Science **344**, 1489 (2014).
[96] H. Li, Q. Zhang, C. C. R. Yap, B. K. Tay, T. H. T. Edwin, A. Olivier, and D. Baillargeat, Advanced Functional Materials **22**, 1385 (2012).
[97] P. A. Bertrand, Physical Review B **44**, 5745 (1991).
[98] S. H. Baek, Y. Choi, and W. Choi, Nanoscale Research Letters **10**, 388 (2015).
[99] H. Cun, M. Macha, H. Kim, K. Liu, Y. Zhao, T. LaGrange, A. Kis, and A. Radenovic, pp. 2646.
[100] D. Jena and A. Konar, Physical Review Letters **98**, 136805 (2007).
[101] R. Fivaz and E. Mooser, Physical Review **163**, 743 (1967).
[102] K. Kang, S. Xie, L. Huang, Y. Han, P. Y. Huang, K. F. Mak, C.-J. Kim, D. Muller, and J. Park, Nature **520**, 656 (2015).
[103] A. M. van der Zande *et al.*, Nature Materials **12**, 554 (2013).
[104] D. Zhou, H. Shu, C. Hu, L. Jiang, P. Liang, and X. Chen, Crystal Growth & Design **18**, 1012 (2018).
[105] H. Li, Y. Li, A. Aljarb, Y. Shi, and L.-J. Li, Chemical Reviews **118**, 6134 (2018).
[106] D. Zhu, H. Shu, F. Jiang, D. Lv, V. Asokan, O. Omar, J. Yuan, Z. Zhang, and C. Jin, npj 2D Materials and Applications **1**, 8 (2017).
[107] G. H. Han *et al.*, Nature Communications **6**, 6128 (2015).
[108] Q. Ji, Y. Zhang, Y. Zhang, and Z. Liu, Chemical Society Reviews **44**, 2587 (2015).
[109] S. Wang, Y. Rong, Y. Fan, M. Pacios, H. Bhaskaran, K. He, and J. H. Warner, Chemistry of Materials **26**, 6371 (2014).
[110] J. Zhou *et al.*, Nature **556**, 355 (2018).
[111] X. Ling, Y.-H. Lee, Y. Lin, W. Fang, L. Yu, M. S. Dresselhaus, and J. Kong, Nano Letters **14**, 464 (2014).
[112] X. Li and H. Zhu, Journal of Materiomics **1**, 33 (2015).
[113] A. K. Geim and K. S. Novoselov, Nature Materials **6**, 183 (2007).

[114] A. Reina, X. Jia, J. Ho, D. Nezich, H. Son, V. Bulovic, M. S. Dresselhaus, and J. Kong*, Nano Letters **9**, 3087 (2009).
[115] J. W. Suk, A. Kitt, C. W. Magnuson, Y. Hao, S. Ahmed, J. An, A. K. Swan, B. B. Goldberg, and R. S. Ruoff, ACS Nano **5**, 6916 (2011).
[116] K. S. Kim *et al.*, Nature **457**, 706 (2009).
[117] S. Bae *et al.*, Nature Nanotechnology **5**, 574 (2010).
[118] T. Kobayashi *et al.*, Applied Physics Letters **102**, 023112 (2013).
[119] N. W. Ashcroft and N. D. Mermin, *Solid State Physics* (Brooks Cole, 1976), 1st edn.
[120] F. Schwierz, Nature Nanotechnology **5**, 487 (2010).
[121] V. V. Cheianov, Fal, V. ko, and B. L. Altshuler, Science **315**, 1252 (2007).
[122] C.-H. Liu, Q. Chen, C.-H. Liu, and Z. Zhong, Nano Letters **16**, 1064 (2016).
[123] S. Lee, K. Lee, C.-H. Liu, G. S. Kulkarni, and Z. Zhong, Nature Communications **3**, 1018 (2012).
[124] Y. M. Lin, C. Dimitrakopoulos, K. A. Jenkins, D. B. Farmer, H. Y. Chiu, A. Grill, and P. Avouris, Science **327**, 662 (2010).
[125] Y.-M. Lin, K. A. Jenkins, A. Valdes-Garcia, J. P. Small, D. B. Farmer, and P. Avouris, Nano Letters **9**, 422 (2009).
[126] S. M. Song, J. K. Park, O. J. Sul, and B. J. Cho, Nano Letters **12**, 3887 (2012).
[127] H. Rokni and W. Lu, Scientific Reports **7**, 42821 (2017).
[128] G. S. Kulkarni, K. Reddy, Z. Zhong, and X. Fan, Nature Communications **5**, 4376 (2014).
[129] G. S. Kulkarni, W. Zang, and Z. Zhong, Accounts of Chemical Research **49**, 2578 (2016).
[130] W. Zang, H. Zhu, Z. Liu, W. You, X. Fan, and Z. Zhong, (In preparation).
[131] W. Zang, Z. Liu, G. S. Kulkarni, H. Zhu, K. Lee, X. Fan, and Z. Zhong, (In preparation).
[132] G. A. Somorjai, *Introduction to surface chemistry and catalysis* (John Wiley and Sons: New York, 1994).
[133] R. C. West and D. R. Lide, *CRC Handbook of Chemistry and Physics* (CRC Press, 1990).
[134] H. d. A. Heck and M. Casanova, Regulatory Toxicology and Pharmacology **40**, 92 (2004).
[135] L. Zhang, *Formaldehyde: Exposure, Toxicity and Health Effects* (Royal Society of Chemistry, 2018).
[136] J. K. McLaughlin, International Archives of Occupational and Environmental Health **66**, 295 (1994).
[137] H.-J. Kim and J.-H. Lee, Sensors and Actuators B: Chemical **192**, 607 (2014).
[138] D. Meng, D. Liu, G. Wang, Y. Shen, X. San, M. Li, and F. Meng, Sensors and Actuators B: Chemical **273**, 418 (2018).
[139] X. Li, J. Wang, D. Xie, J. Xu, R. Dai, L. Xiang, H. Zhu, and Y. Jiang, Sensors and Actuators B: Chemical **221**, 1290 (2015).
[140] Y. Liu, G. Zhu, B. Ge, H. Zhou, A. Yuan, and X. Shen, CrystEngComm **14**, 6264 (2012).
[141] G. Zhu, C. Xi, H. Xu, D. Zheng, Y. Liu, X. Xu, and X. Shen, RSC Advances **2**, 4236 (2012).
[142] I. Castro-Hurtado, C. Malagù, S. Morandi, N. Pérez, G. G. Mandayo, and E. Castaño, Acta Materialia **61**, 1146 (2013).
[143] V. Panchal, C. E. Giusca, A. Lartsev, N. A. Martin, N. Cassidy, R. L. Myers-Ward, D. K. Gaskill, and O. Kazakova, 2D Materials **3**, 015006 (2016).

[144] M. Akbi and A. Lefort, Journal of Physics D: Applied Physics **31**, 1301 (1998).
[145] IARC monographs on the evaluation of carcinogenic risks to humans. Supplement **7**, 1 (1987).
[146] Facts About Benzene, (Centers for Disease Control and Prevention) https://emergency.cdc.gov/agent/benzene/basics/facts.asp (2021).
[147] C. P. Weisel, Chemico-Biological Interactions **184**, 58 (2010).
[148] L. A. Wallace, Cell biology and toxicology **5**, 297 (1989).
[149] N. Barsan, D. Koziej, and U. Weimar, Sensors and Actuators B: Chemical **121**, 18 (2007).
[150] B. T. Marquis and J. F. Vetelino, Sensors and Actuators B: Chemical **77**, 100 (2001).
[151] A. A. Tomchenko, G. P. Harmer, B. T. Marquis, and J. W. Allen, Sensors and Actuators B: Chemical **93**, 126 (2003).
[152] Z. Wen and L. Tian-mo, Physica B: Condensed Matter **405**, 1345 (2010).
[153] S. F. Liu, L. C. H. Moh, and T. M. Swager, Chemistry of Materials **27**, 3560 (2015).
[154] I. V. Zaporotskova, N. P. Boroznina, Y. N. Parkhomenko, and L. V. Kozhitov, Modern Electronic Materials **2**, 95 (2016).
[155] Y. Lu, B. R. Goldsmith, N. J. Kybert, and A. T. C. Johnson, Applied Physics Letters **97**, 083107 (2010).
[156] M. G. Campbell, S. F. Liu, T. M. Swager, and M. Dincă, Journal of the American Chemical Society **137**, 13780 (2015).
[157] Scaled-Down Carbon Nanotube Transistors Inch Closer to Silicon Abilities, (IEEE) https://spectrum.ieee.org/nanoclast/semiconductors/devices/scaleddown-carbon-nanotube-transistors-inch-closer-to-silicon-abilities.
[158] F. Röck, N. Barsan, and U. Weimar, Chemical Reviews **108**, 705 (2008).
[159] A. D. Wilson and M. Baietto, Sensors **9** (2009).
[160] E. C. Nallon, V. P. Schnee, C. Bright, M. P. Polcha, and Q. Li, ACS Sensors **1**, 26 (2016).
[161] S. Wold, K. Esbensen, and P. Geladi, Chemometrics and Intelligent Laboratory Systems **2**, 37 (1987).
[162] H. Abdi and L. J. Williams, WIREs Computational Statistics **2**, 433 (2010).
[163] G. S. Kulkarni, K. Reddy, W. Zang, K. Lee, X. Fan, and Z. Zhong, Nano Letters **16**, 695 (2016).
[164] PubChem, https://pubchem.ncbi.nlm.nih.gov/ (Accessed October 2020).